First-Principles Modeling of Optically Active Organic Molecules in Solar Cell Devices and Biological Environments

PAR

Jun REN

(EPFL
ÉCOLE POLYTECHNIQUE
FÉDÉRALE DE LAUSANNE

Suisse
2011

First-principles modeling of optically active organic molecules in solar cell devices and biological environments

JUN REN

Institut des Matériaux
École Polytechnique Fédérale de Lausanne (EPFL)

ABSTRACT

With the increasing cognition of the importance of organic molecules, they are widely applied in printing, biological and pharmacological fields, because of their special capabilities of harvesting solar light, scavenging free radicals, and chelating metal ions. During the past decades, the unique photoelectronic and photochemical properties of organic molecules, such as phthalocyanine, cyanidin, and their relevant derivatives, attract tremendous attention, because they provide an excellent opportunity to solve the worldwide energy crisis by converting directly the solar light to electricity. The surface morphology and electronic interaction of these organic molecules with other molecules, surfaces or interfaces play a critical role in determining the performance of the electronic and optical devices based on organic molecules.

In this thesis, we focus on the investigation of several selected organic molecules, and their interaction with molecules, inorganic semiconductors, and organic semiconductors, by using first-principles electronic structure calculations based on density functional theory, and time-dependent density functional theory. Particular attention is paid to the atomic structure, electronic and optical properties of organic molecules and the corresponding interfaces. The focus of this thesis is on the following aspects of the organic molecules: (i) The complexation mechanism of flavonoids with metal ions. The most likely chelation site for Fe is the 3-hydroxyl-4-carbonyl group, followed by 4-carbonyl-5-hydroxyl group and the $3'$-$4'$ hydroxyl (if present) of quercetin. A complex of two quercetin molecules with a single Fe ion is energetically more stable, however, six orbitals of Fe in the three quercetin complex are saturated by three perpendicular molecules to form and octahedral configurations. Furthermore, the optical absorbance spectra serves as signatures to identify various complexes. (ii) The electronic coupling between a dye molecule (Cyanidin) and a TiO_2 nanowire. Upon molecular adsorption on TiO_2 [010]-wire, cyanidin will be deprotonated into the quinonoidal form. This results in its highest occupied molecular orbitals being located in the middle of TiO_2 bandgap and its lowest occupied molecular orbitals being close to the TiO_2 conduction band minimum, in turn enhancing visible light absorption. Moreover, the excited electrons are injected into TiO_2 conduction band within a time scale of 50 fs with negligible electron-hole recombination. (iii) The atomic and electronic structure of copper (fluoro-)phthalocyanine and graphene. When adsorbed on graphene, $F_{16}CuPc$ molecules prefer to form a close-packed hexagonal lattice with two-ordered alternating α and β stripes, whereas CuPc would like to form a square lattice. In addition, phthalocyanine adsorption modifies the electronic structure of graphene introducing intensity smoothing at 2-3 eV below and a small peak at ∼0.4 eV above the Dirac point in the density of states. And

finally, (iv) the electronic interaction between CuPc and fullerene. For CuPc/C_{60} molecular complex, CuPc prefers to lie flat on the C_{60} surface rather than taking the standing-up molecular orientation. The favorable adsorption site for CuPc is the bridge site of C_{60} with one N-Cu-N bond of CuPc being parallel to a C-C bond of C_{60}. Based on the analysis of the molecular complex, we predict that CuPc/C_{60}(001) thin film heterojunction adopting the lying-down molecular orientation should have a higher efficiency of charge transfer in comparison with the relevant CuPc/C_{60}(111) heterojunction with the standing-up arrangement.

ZUSAMMENFASSUNG

Mit zunehmender Erkenntnis der Wichtigkeit organischer Moleküle werden diese auf Grund ihrer speziellen Fähigkeiten Sonnenenergie zu sammeln, freie Radikale zu binden und Chelatkomplexe mit Metallionen zu bilden, in Druck, Biologie und Pharmakologie verbreitet eingesetzt. In den vergangenen Jahrzehnten haben die einzigartigen photoelektrischen und photochemischen Eigenschaften organischer Moleküle wie Phtalocyanin, Cyanidin und deren relevanter Derivate große Aufmerksamkeit auf sich gezogen, weil sie eine exzellente Möglichkeit bieten, durch direkte Umwandlung von Sonnenlicht in elektrische Energie die weltweite Energiekrise zu lösen. Die Oberflächenmorphologie sowie die elektronische Wechselwirkung dieser organischen Moleküle mit anderen Molekülen, Ober- und Grenzflächen haben entscheidenden Einfluss auf die Leistung drauf basierender elektronischer und optischer Bauelemente.

In dieser Arbeit konzentrieren wir uns auf die Untersuchung organischer Moleküle und deren Wechselwirkung mit Molekülen, anorganischen Halbleitern und organischen Halbleitern mittels *ab-initio* Berechnungen der Elektronenstruktur basierend auf Dichtefunktionaltheorie und zeitabhängiger Dichtefunktionaltheorie. Besonderes Augenmerk liegt auf der Betrachtung der atomaren Struktur und elektronischen sowie optischen Eigenschaften organischer Moleküle und der betreffenden Grenzflächen. Der Fokus dieser Arbeit liegt auf den folgenden Aspekten organischer Moleküle: (i) Der Komplexbildungsmechanismus von Flavonoiden mit Metallionen. Der wahrscheinlichste Chelatisierungsplatz für Fe ist die 3-Hydroxyl-4-Carbonyl-Gruppe, gefolgt von der 4-Carbonyl-5-Hydroxyl-Gruppe und dem 3'-4' Hydroxyl (falls vorhanden) von Quercetin. Ein Komplex zweier Quercetin Moleküle mit einem einzelnen Fe ist jedoch energetisch stabiler: sechs Orbitale des Fe im drei-Quercetin Komplex sind durch drei senkrecht zueinander stehende Moleküle abgesättigt. Des weiteren dienen die optischen Absorptionsspektren als Signaturen zur Identifikation verschiedener Komplexe. (ii) Die elektronische Kopplung zwischen einem (Cyanidin) Farbstoffmolekül und einem TiO_2 Nanodraht. Bei der Adsorption auf einem TiO_2 [010]-Draht wird Cyanidin in die quinonartige Form deprotoniert. Daraus resultiert, dass sein höchstes besetzten Molekülorbital in der Mitte der TiO_2 Bandlücke liegt und sein niedrigstes unbesetztes Orbital nahe dem TiO_2 Leitungsbandminimum, wodurch die Absorption von sichtbarem Licht verstärkt wird. Des weiteren werden die angeregten Elektronen innerhalb eines Zeitraums von 50 fs und mit vernachlässigbarer Elektron-Loch-Rekombination in das TiO_2 Leitungsband injiziert. (iii) Die atomare und elektronische Struktur von Kupfer-(fluoro-)Phtalocyanin und Graphen. Adsorbiert auf Graphen bevorzugen F_{16}CuPc Moleküle ein dicht gepacktes hexagonales Gitter mit zwei geordneten α und β Streifen, während CuPc ein quadratisches Gitter bilden möchte. Zusätzlich modifiziert die Adsorption von Phtalocyanin die Elektronenstruktur von Graphen wodurch die Intensität der Zustandsdichte zwischen 2 und 3 eV unterhalb des Dirac Punktes geglättet wird und ein kleiner Peak bei ~0.4 eV oberhalb auftaucht. Und schließlich, (iv) die elektronische Wechselwirkung zwischen CuPc und Fullerenen. Für den CuPc/C_{60}

Molekülkomplex bevorzugt CuPc flach auf der C_{60} Oberfläche aufzuliegen mit einer N-Cu-N Bindung des CuPc parallel zu einer C-C Bindung des C_{60}. Basierend auf der Analyse des Molekülkomplexes wird vorhergesagt, dass ein CuPC/C_{60} Dünnschicht-Heteroübergang mit liegender Ausrichtung des Moleküls eine höhere Ladungstransfereffizienz im Vergleich zur relevanten CuPc/C_{60}(111) Heterostruktur mit stehender Anordnung haben sollte.

LIST OF PUBLICATIONS

This thesis consists of an introductory text and the following papers:

I   Theoretical investigations on the fullerene and metal phthalocyanine hetero-junciton
Jun Ren, S. Meng, E. Kaxiras
To be submitted. (2011).

II   Properties of copper phthalocyanine layers deposited on epitaxial graphene
Jun Ren, S. Meng, Y. L. Wang, X. C. Ma, Q. K. Xue, E. Kaxiras
J. Chem. Phys. in press (2011).

III   Selective adsorption and electronic interactions of F_{16}CuPc on epitaxial graphene.
Y. L. Wang, _Jun Ren_, C. L. Song, Y. P. Jiang, L. L. Wang, K. He, X. Chen, J. F. Jia, S. Meng, E. Kaxiras, X. C. Ma, Q. K. Xue
Phys. Rev. B. **82**, 245420 (2010).

IV   Optical properties of clusters and molecules from real-time time-dependent density functional theory using a self-consistent field.
Jun Ren, E. Kaxiras, S. Meng
Molecular Physics **108**, 1829 (2010).

V   Direct correlation of crystal structure and optical properties in wurtzite/zinc-blende GaAs nanowire heterostructures.
M. Heib, S. Conesa-Boj, _Jun Ren_, H. H. Tseng, A. Gali, A. Rudolph, Em Uccelli, F. Peiro, J. R. Morante, D. Schuh, E. Reiger, E. Kaxiras, J. Arbiol, A. F. i Morral
Phys. Rev. B **83**, 045303 (2011).

VI   Structural, electronic and optical properties of representative Cu-flavonoid complexes.
C. Lekka, _Jun Ren_, S. Meng, E. Kaxiras,
J. Phys. Chem. B **113**, 6478 (2009).

VII   Complexation of flavonoids with iron: structure and optical signatures.
Jun Ren, S. Meng, C. Lekka, E. Kaxiras
J. Phys. Chem. B **112**, 1845 (2008).

VIII   Natural dyes adsorbed on TiO_2 nanowire for photovoltaic applications: enhanced light absorption and ultrafast electron injection.
S. Meng, _Jun Ren_, E. Kaxiras
Nano Letters **8**, 3266 (2008).

Scientific publications not included in this thesis:

I Cooperativity in surface bonding and hydrogen bonding of water and hydroxyl at metal surfaces.
T. Schiros, H. Ogasawara, L.-A. Naslund, K. J. Andersson, *Jun Ren*, S. Meng, G. S. Karlberg, M. Odelius, A. Nilsson, L. G. M. Pettersson
J. Phys. Chem. C **114**, 10240 (2010).

II Is the nature of magnetic order in copper-oxides and in iron-pnictides different?
E. Manousakis, *Jun Ren*, S. Meng, E. Kaxiras
Solid State Communications **150**, 62 (2010).

III Effective Hamiltonian for FeAs-based superconductors.
E. Manousakis, *Jun Ren*, S. Meng, E. Kaxiras
Phys. Rev. B **78**, 205112 (2008).

IV First-principles study of water on copper and noble metal (110) surfaces.
Jun Ren, S. Meng
Phys. Rev. B **77**, 054110 (2008).

V Atomic structure and bonding of water overlayer on Cu(110): the orderline for intact and dissociative adsorption.
Jun Ren, S. Meng
J. Am. Chem. Soc. **128**, 9282 (2006).

VI Spin accumulation and decay in magnetic Schottky barriers.
G. E. W. Bauer, Y. Tserkovnyak, A. Brataas, *Jun Ren*, K. Xia, M. Zwierzycki, P. J. Kelly. Phys. Rev. B **72**, 155304 (2005).

Contents

Introduction

1.1 Organic molecules and applications

1.1.1 Flavonoids as antioxidants

Flavonoids are the most abundant polyphenolic natural compounds with a C_6-C_3-C_6 carbon skeleton, as shown in Fig. 1.1. They are ubiquitous in higher vascular plants, particularly in the leaves, fruits, nuts, skins, flowers, and plant extracts such as red wine and tea.[1] Depending on different substituents in the two benzene rings (A and B in Fig. 1.1), distinct chelation sites, and variations in the heterocyclic rings, over 4000 different flavonoids occurred in nature have been described and studied, and the quantity is still increasing.[2,3]

There have been numerous investigations of flavonoids in recent years because of their potent capacity of scavenging free radicals.[4] In addition, the beneficial biological and pharmacological properties of flavonoids have been reported, such as antitumor, antibacterial, and antimutagenic activity, anticarcinogenic, immune-stimulating, antiallergic, and cardiovascular protection.[5–8] Furthermore, the power-
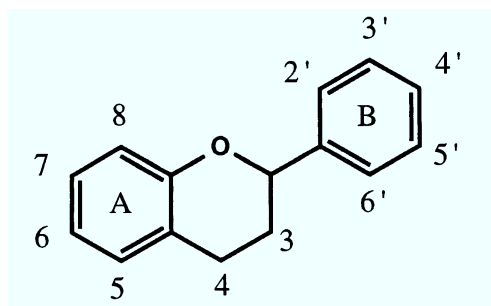

Figure 1.1: Basic structure of flavonoids.

ful antioxidant activity of flavonoids plays an essential role in prevention and treatment of oxidation damage.[4, 9, 10] Quercetin, the 3, 5, 7, 3′, 4′-pentahydroxylflavonol, is the most abundant and one of the most powerful antioxidants in the flavonoid family. These useful properties are attributed to their promising abilities that flavonoids can chelate transition metal ions, such as Fe^{2+}, Cu^{2+}, and Mg^{2+}, bind to biologic polymers such as enzyme, hormone carriers and DNA, and scavenge harmful free radicals as well.[10]

There are two possible mechanisms for the antioxidant activity of flavonoids. One is ascribed as free radical scavenging activity, because of the lower reduction potentials of flavonoids radicals than those superoxide radicals. Flavonoids may inactivate these species by binding them diectly, preventing the damage of their reactions with biological polymers. Another is the metal ions chelation,[3] since transition metal ions involve in the initiation of free radical processes. It is well known that flavonoids can scavenge metal ions to provide protection from oxidative damage.[11, 12] Take iron as an example, because it is the most abundant metal ions in a human body. Excessive concentration of iron ions may lead to production of free hydroxyl radicals through the Fenton reaction.[13, 14] Flavonoids can efficiently bind Fe ions to form complexes through charge transfer from its deprotonated hydroxyl group to form stable phenoxyl radicals, which prevent the deleterious consequence of the Fenton reaction. It is worth pointing out that flavonoids alone provide minimal benefits due to slow absorption by the body. Chelating metal ions can enhance the antioxidant activity and accelerate the whole process.

Several investigations have emphasized that the antioxidant activity of flavonoids complexes dependents strongly on the number of hydroxyl (OH) groups, the relevant positions on the different rings, and metal ions chelation sites.[8, 9, 15–17] Despite tremendous efforts, the atomic structures of metal-flavonoid complexes and the corresponding binding mechanism remain unclear, mainly because of experimental difficulties in detecting these complexes with the molecular resolution in solution.[18–20]

In general, the complexes of flavonoid and metal ions have been investigated by using various methods, such as ultraviolet-visible (UV-vis) or fluorescence spectroscopies, ^{1}H and ^{13}C nuclear magnetic resonance (NMR) spectroscopies. Experimental results observed in UV/vis region confirm that there are two major absorption bands for most flavonoids: ranging from 320 nm to 380 nm corresponds to the absorption of the ring B, and the 210-285 nm region represents the contribution of the ring A.[8, 21] However, it is very hard to identify the atomic structure of complexes, the ratio of metal/flavonoids, and the chelation site for metal ions from these experimental results. To address this puzzle, it needs the theoretical work to figure out the possible configurations and understand the mechanism of the complexation from the atomic level.

1.1.2   Cyanidins as light sensitizers

Cyanidin is another natural organic compound, which belongs to the family of anthocyanines with the similar structure of quercetin, as shown in Fig. 1.2. The difference
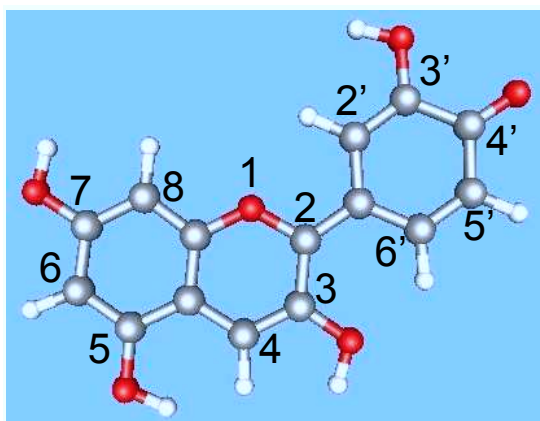
Figure 1.2: The geometry of cyanidin molecule. C, O, and H are represented by gray, red and white spheres, respectively.

between cyanidin and quercetin molecule (as discussed in the previous section) is that cyanidin molecule lacks the carbonyl (C=O) group at the site 4 and replaces the OH group by the C=O group at the site 4′, in comparison with quercetin molecule.

Cyanidin is a water soluble pigment found in most red colored berries including cranberry, blueberry, blackberry, bilberry and cherry, and other fruits such as apples, pears, peaches and plums as well. It can also be found in red cabbage and red onion. The highest concentration of cyanidin are distributed in the skin of these fruits.[22, 23] Depending on the the pH value of the solution, the color of cyanidin changes from red in acidic solution to blue in basic solution.

Cyanidin has attracted extensive attentions because of its pharmacological properties, such as anti-toxic effect, anti-inflammatory, anti-cancer, skin protection, and aids in preventing obesity, diabetes, and cardiovascular diseases.[22–24] Due to the similarity of geometry as the flavonoids (discussed in previous section), cyanidin is also a powerful antioxidant and radical-scavenger.[25–27] Furthermore, cyanidin is widely used as a light absorber in natural dye-sensitized solid state photovoltaic cells, because it can absorb intensely the visible light around 550 nm and UV radiation around 330 nm.

Recently, more and more investigations are focusing on the dye-sensitized solar cell (DSSC),[28–38] often named the "Grätzel cell",[39] since it is a promising alternative to the traditional route toward harvesting solar energy in the effort to address the daunting global energy crisis and environmental challenges. In TiO_2-based DSSCs, the power conversion efficiency of over 11%[29] can be achieved under standard global air mass 1.5 sunlight by using ruthenium-based compounds as dye sensitizers. But the expensive and complicated synthesis process, and undesirable environmental impact of this kind of prototype call for cheaper, simpler and safer natural dyes including chlorophyll, cyanin, arotene and porphyrin, as alternatives.[35, 38] Experimentally, natural dye sensitized TiO_2 solar cells have reached the efficiency of 7.1%[38] with the high stability, and 10%[40] for synthetic metal-free organic dyes. The advantage of using natural dye molecules as light sensitizers in the DSSC is the low cost, easy
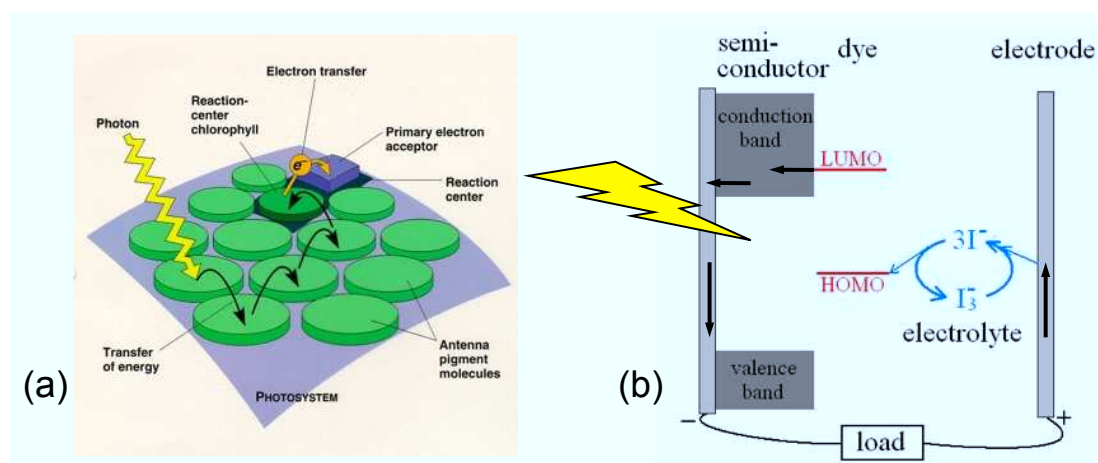
Figure 1.3: The schematic diagrams of natural light harvesting procedures in photosynthesis (a), and the operating principle of dye-sensitized solar cell (b).

fabrication and the high efficiency, which qualifies it as a competing candidate to more established technologies based on monocrystalline Si and nanocrystalline thin film solar cells.[41]

The central idea of the DSSC is to separate the light adsorption process from the charge collection process, mimicking the natural light harvesting procedures in photosynthesis, by combining dye sensitizers with semiconductors (see Fig. 1.3a). This enables the use of wide-bandgap and cheap semiconductors such as TiO_2 and ZnO in DSSCs. To be effective, it requires the highest occupied molecular orbital (HOMO) of the dye to reside in the band gap of the semiconductor and its lowest unoccupied molecular orbital (LUMO) to locate within the conduction band of the semiconductor,[34] as depicted in Fig. 1.3b.

On the other hand, nanostructured materials offer new opportunities to reduce both cost and size and design more efficient solar cells, especially for one-dimensional (1D) nanostructure.[42,43] The use of these 1D nanostructures, including nanowires, nanorods, nanoparticles and nanotubes, can improve efficiency of photon absorption, electron transport and collection in DSSCs,[30–33,42] due to its additional benefits in two aspects: 1) enhanced visible light scattering and absorption, because of the high length-to-diameter ratio and a total length reaching hundreds of micrometers; 2) the 1D geometry facilitates the rapid, diffusion-free electron transport to the electrodes.[31,33] As a result, special attentions have been paid in precisely controlling the growth of one-dimensional (1D) nanowire[30,31] and nanotube.[32,33] However, there are still enormous challenges we have to meet. DSSCs based on 1D nanostructure show a relatively low power conversion due to reduced surface areas and poor stability than thin-film based DSSCs.[41,43]

1.1.3 Phthalocyanines as charge conductors

Discovery. In 1907, Braun and Tcherniac[44] observed dark insoluble precipitates

4
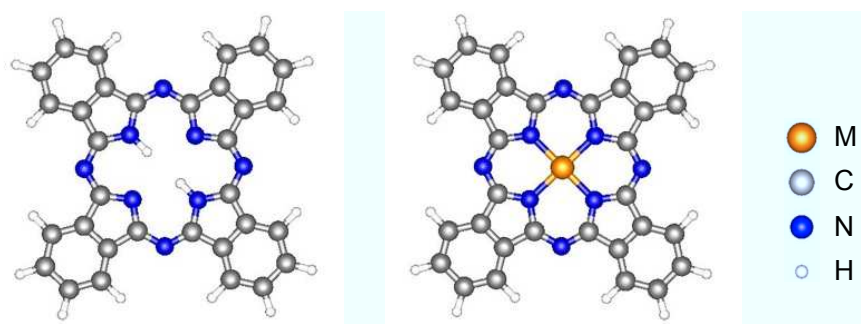
Figure 1.4: The geometry of isolated H_2Pc and MPc molecules with M= Cu, Mg, Zn, and other metal ions.

during the preparation of ortho-cyanobenzamide. Similarly, de Diesbach and von der Weid[45] obtained exceptionally stable and blue materials (metal-free and copper phthalocyanine) in 1927 by accident. Later, the full elucidation of the structure of phthalocyanine and its derivatives[46–48] by the X-ray diffraction techniques and the corresponding synthesis, have been reported during the 1930s.

Structure of metal phthalocyanine. Phthalocyanine (Pc) is a symmetrical aromatic macrocycle, composed of four isoindole units connected by four nitrogen atoms, which is close to the natural porphyrin, as shown in Fig. 1.4. The sufficient size is beneficial to the accommodation of various elemental ions in the central cavity of Pc molecule. Depending on the different central metal cation, the appearance of metal phthalocyanine (MPc) changes from dark blue to metallic bronze to green in its solid state.

In general, the macrocycle exists as a dianion (Pc^{2-}). Therefore, MPc can be divided into five categories in terms of the central ions: i) the metal free Pc, namely H_2Pc, ii) monovalent MPc, such as Li_2FPc; iii) divalent MPc, such as MgPc, CuPc, ZnPc, CoPc, etc⋯ iv) trivalent MPc, including AlClPc and AlOHPc. (in general, M can be a metal halide or a hydroxide in this case); and v) tetravalent MPc: TiOPc, $SiCl_2Pc$, and $Si(OH)_2Pc$, which belongs to a metal oxide, dihalide or dihydroxide. Many metal ions, such as Cu^{2+}, Zn^{2+}, Fe^{2+}, and Mg^{2+} can hold tightly with Pc to form planar structure[49–52] without the distortion of macrocycle. However monovalent, trivalent, and tetravalent metal cations, and large divalent metal ions (such as Pb^{2+}), will protrude from the plane of Pc rings to form non-planar structure.[53]

The potential application in optical and electronic devices requires highly ordered crystalline Pc materials. In contrast to the inorganic electronic materials dominating by covalence bonds, the relatively weak forces, such as van der Waals and $\pi - \pi$ interactions within organic crystals decide the coexistence of Pc polymorphisms, especially for systems deposited by the vacuum sublimation. Different polymorphic crystalline structures had distinct stacking angles, unit cells, and symmetries, which show different absorption spectra. Most MPcs have at least two polymorphic crystalline phases (α- and β-phase).[54] It is often stated that the β-phase, transferred from the α-phase through heating, is thermodynamically more stable than the α-phase, except for small particles, due to important size effect in

this system.[55, 56]

Characteristics and applications. Most MPc molecules show intense absorption in the red/near infrared (IR) regions of the solar spectrum at 600-800 nm (Q-band) and in the near-ultra violet region around 300-400 nm (B-band).[55, 57–61] The non-peripheral substitutions will largely influence the optical spectra of MPcs.[55] In addition, MPcs show a nonlinear response to light. Furthermore, MPcs are characterized by electronic conductors, high thermal and chemical stability, which make them suitable for widespread technological applications, such as dyes, inks, chemical sensors, photosensitizers, semiconductors, information storage systems, optical filters, and energy conversion materials in photovoltaic and solar cells.[54, 55, 62–65]

1.2 Brief history of research on MPcs in organic solar cells

1.2.1 Organic photovoltaic device architectures

MPc and its derivatives have received tremendous attention as a major component in various types of organic solar cells (OSCs) (Fig. 1.5c) over past decades, because of their potential advantages: be relatively cheap to fabricate, can be used on flexible and large-area substrates, and can be shaped or tinted to suit domestic devices, architectural or decorative applications, with a rapid increase in energy conversion efficiency.

The current OSCs with high performance can be grouped primarily into two types of junctions, the bilayer heterojunction with two planar thin films,[44, 66, 67] and the bulk heterojunction.[68–71] The typical bilayer heterojunction thin film device, as displayed in Fig. 1.5a, is composed of two dissimilar organic semiconductor materials as the electron donor and accepter, forming a sandwich structure in contact with the top and bottom electrodes. The principal fabrication[44, 63, 72] process is: indium tin oxide (ITO) is used as the transparent and conductive substrate electrode (bottom contact), then covers successively an electron donor and acceptor layer by vacuum deposition or by spin doping, and finally uses a low work function material as the top contact (e.g. Al, Ag/Mg, Ca, etc). The essential difference for two kinds of OSCs is the active interaction area between the donor and acceptor layers. For the bulk heterojunction, there is no obvious interface between the electron donor and acceptor layers.

1.2.2 Basic operating principles

In general, copper phthalocyanine (CuPc) is most widely chosen as an electron-donor (p-type) materials in contacting with electron-acceptor (n-type) fullerene (C_{60}), and copper hexadecafluorophthalocyanine ($F_{16}CuPc$) molecules as well.[73, 74] The whole process of converting solar light into electric power in the organic solar cell contains three consecutive steps (taking MPc/C_{60} as an example in Fig. 1.5b): 1)
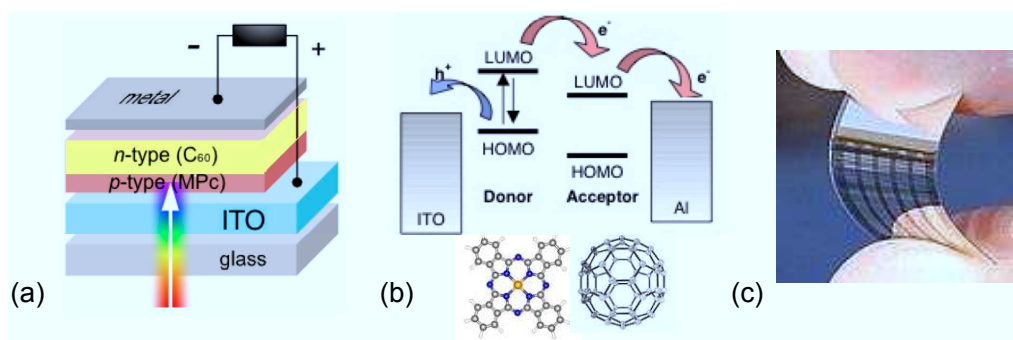
Figure 1.5: The ideal schematic diagrams (a) and schematic views of energy levels from Ref. [76] (b) in MPc/C_{60} heterojunctions. (c) The photo of the organic solar cells.

MPc absorbs photons whose energy matches the band gap of MPc, to generate the electron-hole pairs (excitons). 2) Excitons diffuse to the space charge layer of MPc/C_{60} interface, where excitons are separated by the electric field present in this layer. 3) The electrons are injected into the C_{60} layer and finally collected by a cathode, and the positive holes are driven to an anode through MPc to finish the external circuit.[62, 75]

Although DSSCs have something in common with OSCs, such as low cost, easy fabrication and flexibility, they differ in several aspects: 1) DSSCs are composed of dye molecules and inorganic semiconductors, whereas OSCs replace inorganic semiconductors by organic semiconductors; 2) the incident photon absorbed by the dye molecule will excite an electron directly rather than an exciton (electron-hole pair), since the excited electron in organic semiconductors has strong Coulomb interaction with a hole left in the valence band; 3) dye molecules in DSSCs need the liquid electrolyte, normally iodide/triiodide solution (see Fig. 1.3b) to compensate electrons after exciting electrons; 4) most of DSSCs function in the liquid solution, whereas OSCs work in solid states.

1.2.3 Characterization of a solar cell device

The current-voltage characteristics of a solar cell in the dark and under illumination are described in Fig. 1.6,[63] which is of importance to judge the performance of a device. In the dark, there is almost no current flowing until the forward bias applied on the contact is higher than open circuit voltage (V_{oc}). Under the illumination, the maximum generated photocurrent (I_{sc}) is under the short circuit condition. The maximum power output P_{MAX} is denoted by the largest product of voltage and current, at the maximum power point (MPP) as shown in Fig. 1.6.

The photovoltaic power conversion efficiency (η_e) of a solar solar cell, as defined as

$$\eta_e = \frac{V_{oc} \times I_{sc} \times FF}{P_{in}}, \quad FF = \frac{V_{mpp} \times I_{mpp}}{V_{oc} \times I_{sc}} \tag{1.1}$$

where FF is the fill factor, and P_{in} is the incident light power density. The V_{oc} and I_{sc} is marked in Fig. 1.6.
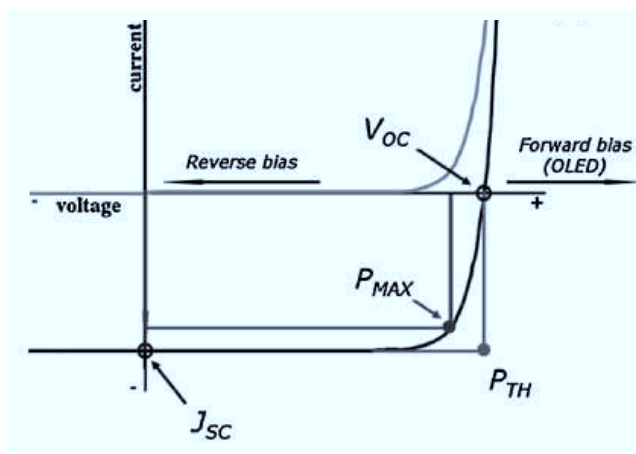
Figure 1.6: Current-voltage (I-V) curves of an organic solar cell (dark, gray curve; illuminated, black curve) from Ref. [63].

1.2.4   Highlights of researches on MPc/C$_{60}$ organic solar cells

Recently, numerous studies are dedicated to the enhancement of the photovoltaic power conversion efficiency of organic solar cells based on C$_{60}$ and MPc heterojunction. The common approaches include: 1) doping other materials, such as pentacene or rubrene into MPc layer to improve its carrier mobility or broadening light absorption and improving exciton diffusion efficiency;[77,78] 2) modifying the morphology of heterojunction by controlling substrate or source temperature;[68,79–81] 3) inserting an intrinsic layer to increase Voc, reduce the serial resistance, or optimizing optical interference;[82–85] 4) modifying the geometry of the electrodes;[86–88] 5) introducing highly purified organic semiconductor;[89] 6) adopting the tandem cell.[90,91] The power conversion efficiency (PCE) of organic photovoltaic (OPV) cells have recently achieved 5-6% through these approaches. It is worth pointing out that precisely controlling the morphology of interface, tuning the relevant electronic structure, and understanding the mechanism of the interaction at the interface of the heterojunction attracts increasing attentions, because it plays a crucial role in improving performance of solar cells.

It is obvious that enhancement of the charge generation, diffusion and injection ultimately rests upon the interface geometry and interaction of the heterojunction, which can largely enhance the conversion efficiency of organic solar cells. Unfortunately, the interface structure and the environmental effect is not well understood, especially at the atomic level. In addition, the electronic interaction between the electron donor and acceptor is not clear either. Therefore, elucidating the possible configurations of heterojunction, demonstrating the corresponding mechanism of the electronic interaction, and understanding the relevant optical properties of the interface are the principal objectives of this study.

1.3 This thesis

This thesis presents a theoretical and computational study of organic molecules, including flavonoids, cyanidin, and phthalocyanines, and the corresponding surfaces and interfaces with other materials, based on first-principles density functional theory calculations. Our study focuses on the structure, the bonding characters, the mechanism of electronic interaction, and optical properties of molecular adsorption on surface.

This thesis consists of eight chapters. Each chapter gives a brief introduction to background together with discussion on some of the results.

In Chapter 1, we introduce the background of organic molecules we mainly investigated in this thesis, and overview researches involved in these fields, in particularly for the study of organic solar cells.

In Chapter 2, the theoretical and computational methods are employed in the whole thesis.

In Chapter 3, we develop self-consistent time-dependent density functional theory (TDDFT) for calculating optical properties of molecules and nanostructures.

In Chapter 4, we focus on the study of complexation mechanism of flavonoids with iron.

In Chapter 5, we compare GaAs and TiO_2 semiconductor nanowire, and focus on the research of natural dye sensitized TiO_2 solar cell by exploring the deprotonation process and charge injection.

In Chapter 6, we compare the molecular structure, electronic and optical properties for two typical phthalocyanine molecules (CuPc and $F_{16}CuPc$) adsorption on epitaxial graphene, and elucidate the corresponding electronic interaction mechanism.

In Chapter 7, we make a thorough discussion about the atomic configurations, charge transfer and optical signature of the $CuPc/C_{60}$ molecular complex, and propose the $CuPc/C_{60}(001)$ thin film heterojunction with higher efficiency of the charge transfer in comparison with the $CuPc/C_{60}(111)$ system.

In Chapter 8, we present general conclusion and express potential research directions.

Theoretical methodology

In this chapter, we briefly introduce the theoretical methods, the density functional theory (DFT), time dependent density functional theory (TDDFT), with van der Waals density functionals (vdW-DF) and hybrid density functionals which have been extensively used for the study of organic molecules in solar cell and biological environment. DFT is a quantum mechanical theory of correlated many-body systems, which has tremendous impact on calculation of electronic structure of atoms, molecules and solids in the ground states. Combining the electronic structure with TDDFT, this approach can provide the exact features of the excited states, such as optical absorbance spectrum. For organic molecules systems, we apply the vdW-DF to treat this kind of system in which the van der Waals force dominates. In this thesis, we give a brief description of the theoretical methods involved in the atomic and electronic structure calculation and the optical electronic excitation simulations.

2.1 Density functional theory

A quantum mechanical theory for a system of nuclei and interacting electrons is based on solving the many-body Schrödinger equation with the form:

$$H\Psi(\{\mathbf{r}_i, \mathbf{R}_I\}) = E\Psi(\{\mathbf{r}_i, \mathbf{R}_I\}), \tag{2.1}$$

where H is the hamiltonian for the system of electrons and nuclei,

$$
\begin{aligned}
H &= H_{ee} + H_{eN} + H_{NN} \\
&= -\sum_i \frac{\hbar^2}{2m_e}\nabla_i^2 + \frac{1}{2}\sum_{i,j,(i\neq j)} \frac{e^2}{|\mathbf{r}_i - \mathbf{r}_j|} - \sum_{i,I} \frac{Z_I e^2}{|\mathbf{r}_i - \mathbf{R}_I|} \\
&\quad - \sum_I \frac{\hbar^2}{2M_I}\nabla_I^2 + \frac{1}{2}\sum_{I,J,(J\neq I)} \frac{Z_I Z_J e^2}{|\mathbf{R}_I - \mathbf{R}_J|}.
\end{aligned}
\tag{2.2}
$$

11

The above equation contains the kinetic energy and the potential energy due to the interactions between the ions and the electrons. Here $\hbar$ is Plank's constant divided by 2π; m_e and M_I are the mass of the electrons and nuclei respectively; $\{r_i\}$ and $\{R_I\}$ describe the relevant positions of the electrons and nuclei.

Based on the Born-Oppenheimer approximation,[92] the nuclei are treated as classical particles. Thus we can ignore the nuclear kinetic energy, and take it into account as a classical contribution. In addition, we also neglect the final term in equation (2.2) , since it is simply a constant, as far as the electronic degrees of freedom are concerned. The hamiltonian of the system can be written as

$$H = -\sum_i \frac{\hbar^2}{2m_e}\nabla_i^2 + \frac{1}{2}\sum_{i,j,(i\neq j)}\frac{e^2}{|\mathbf{r}_i - \mathbf{r}_j|} + V_{ext}, \qquad (2.3)$$

where, $V_{ext} = -\sum_{i,I}\frac{Z_I e^2}{|\mathbf{r}_i - \mathbf{R}_I|}$, which is the potential applied on the electrons due to the nuclei. Directly solving the equation (2.1) for the coupled electron-nucleus system is extremely difficult, even with this simplification. It is possible to obtain solution by using the quantum Monte Carlo method,[93] however, such calculations become extremely expensive as the number of electrons in the system increase.

In order to simplify the many-body wavefunctions to an equivalent one-electron picture, we introduce two approximations. The simplest approach is to represent the many-body wavefunction by a product of the wavefunctions of the individual electrons,

$$\Psi^H(\{\mathbf{r}_i\}) = \varphi_1(\mathbf{r}_1)\varphi_2(\mathbf{r}_2)\cdots\varphi_N(\mathbf{r}_N). \qquad (2.4)$$

This is known as the Hatree approximation, which would be appropriate if the electrons were non-interacting particles.

With this approximation, the equation (2.1) can be put into the single-particle Hartree equation:[94]

$$[-\frac{\hbar^2}{2m_e}\nabla^2 + V_{ext}(\mathbf{r}) + \sum_{i,j,(j\neq i)}\int d\mathbf{r}'\frac{|\varphi_j(\mathbf{r}')|^2}{|\mathbf{r}-\mathbf{r}'|}]\varphi_i(\mathbf{r}) = E_i\varphi_i(\mathbf{r}). \qquad (2.5)$$

Taking the ferminoic exchange nature of electrons into account, we can choose a properly antisymmetrized wavefunction, which changes sign when we exchange the coordinates of two electrons. To this end, by using the Slater determinant[95] of the single-partical wavefunction:

$$\Psi^{HF}(\{\mathbf{r}_i\}) = \frac{1}{\sqrt{N!}}\begin{vmatrix} \varphi_1(\mathbf{r}_1) & \varphi_1(\mathbf{r}_2) & \cdots & \varphi_1(\mathbf{r}_N) \\ \varphi_2(\mathbf{r}_1) & \varphi_2(\mathbf{r}_2) & \cdots & \varphi_2(\mathbf{r}_N) \\ \vdots & \vdots & & \vdots \\ \varphi_N(\mathbf{r}_1) & \varphi_N(\mathbf{r}_2) & \cdots & \varphi_N(\mathbf{r}_N) \end{vmatrix}, \qquad (2.6)$$

the Hartree equation evolves into the single-particle Hartree-Fock equations,[96]

$$[-\frac{\hbar^2}{2m_e}\nabla^2 + V_{ext}(\mathbf{r}) + \sum_{i,j,(j\neq i)}\int d\mathbf{r}'\frac{|\varphi_j(\mathbf{r}')|^2}{|\mathbf{r}-\mathbf{r}'|}]\varphi_i(\mathbf{r}) - \sum_{i,j,(j\neq i)}\int d\mathbf{r}'\frac{\varphi_j^*(\mathbf{r}')\varphi_i(\mathbf{r}')}{|\mathbf{r}-\mathbf{r}'|}\varphi_j(\mathbf{r}) = E_i\varphi_i(\mathbf{r}).$$
(2.7)

In comparison with the Hartree equation, it contains one extra term, called the 'exchange' term, which describes the effects of interelectronic exchange.

2.1.1 Kohn-Sham equation

Based on the Thomas-Fermi approximation,[97,98] Hohenberg, Kohn and Sham developed the density functional theory,[99,100] which can be applied to any system of interaction particles in an external potential. The basic idea of density functional theory is to use the electronic density as a basic variable to describe the many-body system, which dramatically simplifies the many-body schrödinger equation (2.1). This theory is based on two theorems proposed by Hohenberg and Kohn[99] in 1964.

Theorem I. For any system of interacting particles in an external potential $V_{ext}(\mathbf{r})$, the external potential and hence the total energy is an unique functional of the ground state electron density $n_0(\mathbf{r})$.

Theorem II. The ground state energy can be obtained variationally. For any particular external potential $V_{ext}(\mathbf{r})$, the ground state energy of the system is the global minimum of this functional. The density $n(\mathbf{r})$ that minimizes the total energy is the exact ground state density $n_0(\mathbf{r})$. As a self-consistent method, the Kohn-Sham approach replaces the many-body problem by using independent particles equation but interacting density. The Kohn-Sham approach to the full interacting many-body problem expresses the ground state energy of the system by a functional of electronic density $n(\mathbf{r})$,

$$E[n(\mathbf{r})] = T[n(\mathbf{r})] + \frac{1}{2}\iint d\mathbf{r}d\mathbf{r}'\frac{n(\mathbf{r})n(\mathbf{r}')}{|\mathbf{r}-\mathbf{r}'|} + E_{xc}[n(\mathbf{r})] + \int d\mathbf{r}v_{ext}(\mathbf{r})n(\mathbf{r}), \quad (2.8)$$

where $v_{ext}(\mathbf{r})$ is the external potential, and $E_{xc}[n]$ is the exchange-correlation energy functional. Thus, all the difficult term in the many-body problem is incorporated into an exchange-correlation functional of electronic density. The density is given by sums of squares of the single-particle orbitals,

$$n(\mathbf{r}) = \sum_{i=1}^{N}|\varphi_i(\mathbf{r})|^2. \tag{2.9}$$

The independent-particle kinetic energy T[n($\mathbf{r}$)] is given by

$$T_0[n(\mathbf{r})] = \sum_{i=1}^{N}\int d\mathbf{r}\varphi_i^*(\mathbf{r})(-\frac{\hbar^2}{2m_e}\nabla^2)\varphi_i(\mathbf{r}). \tag{2.10}$$

We apply the variational principle to the Kohn-Sham functional

$$\delta\{E[n(\mathbf{r})] - \sum_{i=1}^{N}\varepsilon_i[\int d\mathbf{r}\varphi_i^*(\mathbf{r})\varphi_i(\mathbf{r}) - 1]\}/\delta\varphi_i(\mathbf{r}) = 0. \tag{2.11}$$

Finally, we arrive the single-particle Kohn-Sham equation:[100]

$$\{-\frac{\hbar^2}{2m_e}\nabla^2 + v_{ext}(\mathbf{r}) + \int d\mathbf{r}\frac{n(\mathbf{r})}{|\mathbf{r}-\mathbf{r}'|} + \frac{\delta E_{xc}[n]}{\delta n}\}\varphi_i(\mathbf{r}) = \varepsilon_i\varphi_i(\mathbf{r}), \qquad (2.12)$$

which can be solved by iteration until it reaches self-consistency. Unfortunately, the exact form of $E_{xc}[n(\mathbf{r})]$ is still unknown. Therefore, to address this issue, consistent approximations to exchange-correlation energy are need.

2.1.2 Local density approximation and the gradient corrections

The local density approximation (LDA) is the simplest approximation to the exchange-correlation energy $E_{xc}[n(\mathbf{r})]$ by considering the local form of the exchange-correlation term of a uniform electron gas. The main idea is to treat a general inhomogenous electronic system as locally homogeneous. This was proposed by Kohn and Sham,[100] in which the exchange-correlation energy term is an integral over all the volume of the system with the relevant energy density at each point assumed to be the same as in a homogeneous electron gas with the same density.

$$E_{xc}^{LDA}[n] = \int d\mathbf{r}n(\mathbf{r})\varepsilon_{xc}^{unif}(n(\mathbf{r})). \qquad (2.13)$$

The common form of ε_{xc} in LDA is obtained by the Ceperley and Alder's Monte Carlo simulation[101] for the uniform electron gas. The corresponding exchange energy is given as

$$\varepsilon_x^{LDA}(r_s) = -0.9164/r_s, \qquad (2.14)$$

$$\varepsilon_c^{LDA}(r_s) = \begin{cases} -0.2846/(1+1.0529\sqrt{r_s}+0.3334r_s) & \text{if } r_s \geq 1 \\ \\ -0.0960+0.0622\ln r_s - 0.0232r_s + 0.0040r_s\ln r_s & \text{if } r_s \leq 1. \end{cases}$$
$$(2.15)$$

where the Wigner-Seitz radius is $r_s = \sqrt[3]{3/4\pi n}$.

The LDA is very successful approximation in the calculation for many systems, in particular whose electronic density is uniform, such as most bulk metals, and less uniform systems, such as semiconductors, alloys and ionic crystals. However, the main limits of the LDA: not taking into account the inhomogeneities in the density and non-local exchange-correlation effects; and the lack of cancelation of the self-interaction, make it less accurate for the systems where the electronic density varies rapidly, such as in molecules and at surfaces. To address the issue of inhomogeneities in electronic density, an expansion of the density in terms of the gradient of the density as well as the density at each point is used to improve the LDA. In general, the exchange-correlation functional can be formally written as

$$E_{xc}^{GGA}[n(\mathbf{r})] = \int d\mathbf{r}f_{xc}(n(\mathbf{r}),|\nabla n(\mathbf{r})|). \qquad (2.16)$$

The exchange energy could be represented by the revised Becke functional,[102]

$$E_x^{GGA} = E_x^{LDA} - \beta\int d\mathbf{r}n^{\frac{4}{3}}\frac{[1-0.55\exp(-1.65x^2)]x^2 - 2.40\times10^{-4}x^4}{1+6\beta x\sinh^{-1}x+1.08\times10^{-6}x^4}, \qquad (2.17)$$

where $x = |\nabla n| / n^{4/3}$. The above exchange-correlation functional is called as the generalized gradient approximation (GGA). Normally, the GGA works very well for molecules, which improves over some of drawbacks of the LDA. The common used functional is composed of Langreth-Mehl,[103] Becke[102], BLYP,[104] Perdew-Wang 91 (PW91),[105] and its simplified version PBE.[106]

Recently, a revised version of the PBE, known as RPBE[107] has also been proposed, which provides an improved description of adsorption and hydrogen-bonded system. In addition, a practical meta-GGA[108] with the fourth order gradient correction is in progress to give very good geometries, frequencies, and quite reasonable energy barriers.

2.1.3 Hybrid density functionals

The hybrid density functionals describe a wide range of molecular systems accurately. The basic idea is to incorporate a certain amount of Hartree-Fock (HF) exchange with the exchange and correlation from LDA or GGA functional. The "half-and-half" form of the hybrid functional was proposed by Becke,[109]

$$E_{xc} = \frac{1}{2}(E_x^{HF} + E_{xc}^{LSDA}). \tag{2.18}$$

Later Becke proposed a semiempirical exchange-correlation functional (B3P91)[110] with three parameters containing Hartree-Fock exchange, the Becke exchange functional (B88),[102] and PW91 correlation,[105] which are successful in describing many molecules.

$$E_{xc} = E_{xc}^{LSDA} + a_0(E_x^{HF} - E_x^{LSDA}) + a_x \Delta E_x^{B88} + a_c \Delta E_c^{PW91}. \tag{2.19}$$

where the semiempirical coefficients (a_0=0.20, a_x=0.72, a_c=0.81) have been determined by fitting to a data set of measured atomization energies. Alternatively, the B3LYP[102, 104] exchange-correlation functional uses the LYP correlation[104] instead of PW91 correlation, which are widely used in chemistry field.

Based on the arguments that the exchange-correlation energy varies as a function of the interelectronic coupling strength, Perdew, Ernzerhof, and Burke[111] introduced the form:

$$E_{xc} = E_{xc}^{DFA} + \frac{1}{4}(E_x^{HF} - E_x^{DFA}), \tag{2.20}$$

where DFA is GGA. They mixed 1/4 Hartree-Fock exchange energy, and gave physical explanations.

Recently, a new hybrid density functional based on a screened Coulomb potential for exchange interaction was introduced by Heyd, Scuseria, and Ernzerhof (HSE).[112]

$$E_{xc}^{SR,HF\ PBE0} = \frac{1}{4}E_x^{HF,SR} + \frac{3}{4}E_x^{PBE} + E_c^{PBE}. \tag{2.21}$$

They used the screened short range (SR) HF exchange instead of the full HF exchange to construct new hybrid functional. Significant reduction in computational cost can be used in calculation for large molecules and clusters, in particular for systems with small band gaps, with reasonable accuracy.

2.1.4 Van der Waals density functional

Sparse systems, including soft matters, biostructures and adsorption systems, are abundant and have strong local bonds and weak nonlocal interaction, such as van der Waals forces, which exist between atoms separated by space. The common use of semilocal correction functionals in Kohn-Sham density functional theory completely miss nonlocal dispersion interaction. Recently, a van der Waals density functional (vdW-DF) was introduced[113, 114] to deal with several layered materials with good accuracy. The basic idea is to split the correlation energy into short and long range parts:

$$E_c[n] = E_c^0[n] + E_c^{nl}[n]. \tag{2.22}$$

The short-ranged term $E_c^0[n]$, is treated by the LDA, and the long-ranged term $E_c^{nl}[n]$ depending on densities, is written as

$$E_c^{nl}[n] = \frac{1}{2}\int d\mathbf{r}d\mathbf{r}' n(\mathbf{r})\varphi(\mathbf{r},\mathbf{r}')n(\mathbf{r}'). \tag{2.23}$$

The vdW-DF is promising to get the comparable binding energy for the molecular adsorption system with experimental results. But the interlayer separation predicted by the vdW-DF is a few percents higher than that of experimental value.

2.1.5 Atomic orbitals and Pseudopotentials

When studying periodic crystals and nonperiodic systems, such as solids, surfaces, interfaces, and isolated molecules, Bloch's theorem is usually utilized in combination with basis orbitals which represent a solution of Schrödinger equation to verify the translational periodicity of the supercell. According to Bloch's theorem, the single-particle wavefunctions have the form

$$\Psi_{j,\mathbf{k}}(\mathbf{r}) = \exp(i\mathbf{k}\cdot\mathbf{r})u_{j,\mathbf{k}}(\mathbf{r}), \tag{2.24}$$

where j labels the band, $\mathbf{k}$ indicates wave vector, and $u_{j\mathbf{k}}(\mathbf{r})$ is a periodic function which can be expanded in planewave (PW) or atomic orbitals (AO) basis sets. Thus, the wavefunctions can be written as

$$\Psi_{j,\mathbf{k}}(\mathbf{r}) = \sum_m c_m(\mathbf{k})\chi_{m,\mathbf{k}}(\mathbf{r}), \tag{2.25}$$

where m labels the states, $c_m(\mathbf{k})$ is the expansion coefficient, $\chi_{m,\mathbf{k}}(\mathbf{r})$ is a basis state, and the summation is over the all the states in the basis.

For solids and general condensed phases with periodic boundary condition, it naturally introduces the truncated PW basis set as solutions of Schrödinger equation. It has some advantages, quite simple and analytic calculation of energy, forces, and stress, and representing the same accuracy for all regions of space. However, the truncated PW basis sets show bad performance for systems of low dimensionality, such as molecules, wires, or surfaces, and charged systems unless compensating

background is added. In addition, the calculation is quite expensive with increase of number of atoms in systems.

In contrast, a suitable AO combination constructed from the eigenstates of the atomic pseudopotentials[115,116] as basis functions is successful to describe molecular systems or condensed phases. The linear combination of atomic orbitals (LCAOs) denotes a basis of atomic functions, which provides a good description of electronic states in materials. The numerical AOs are spatially confined, being strictly zero beyond a certain radius from the nucleus. The use of confined numerical AOs plays a crucial role in achieving the high efficiency of calculations, making it suitable for large system calculations, because the matrix sizes in LCAO representation is considerably smaller than that for other basis sets, such as PW and real-space grids.[117] When the electron wave functions and density are projected onto a real-space grid in order to calculate the Hartree and exchange-correlation potentials and their matrix elements, the computational cost for the construction and storage of the Hamiltonian and the electronic density can be made to scale linearly with the number of atoms in large systems.[118]

Due to the divergence of nuclear potential ($\sim 1/r$) at the origin, the wavefunction of core electrons varies rapidly, which requires a huge number of PW components to represent such steep wavefunctions. To solve this problem, one way is to modify the PW by using linearized augmented planewaves (LAPW)[119] or linear combination of muffin orbitals (LMTO);[120] another way is to modify the potential. The modified potential, known as "pseudopotential",[121] is to replace the strong Coulomb potential of the nucleus by an effective ionic potential acting on the valence electrons. It has a Coulomb attractive potential plus a repulsive potential to mimic the effect of core electrons, thus the potential varies slowly in the nucleus region. As a rule of thumb, the construction of pseudopotential should maintain that the corresponding eigenvalues and wavefunctions are the same as that in valence region. Assuming the exact Hamiltonian for the valence states φ_v and core states φ_c is H,

$$H|\varphi_v\rangle = E_v|\varphi_v\rangle, \quad H|\varphi_c\rangle = E_c|\varphi_c\rangle. \tag{2.26}$$

Noting $\langle\varphi_c|\varphi_v\rangle = 0$, we can construct a pseudo-wavefunctions φ_v^{ps} by combining the core and the true valence wave function in the following form:

$$|\varphi_v^{ps}\rangle = |\varphi_v\rangle + \sum_c \langle\varphi_c|\varphi_v^{ps}\rangle|\varphi_c\rangle. \tag{2.27}$$

Here, the pseudo-wavefunction is not orthogonalized to the core states. Thus the pseudo-wavefunction satisfies the modified Schrödinger equation:

$$(H + \sum_c (E_c - E_v)|\varphi_c\rangle\langle\varphi_c|)|\varphi_v^{ps}\rangle = E_v|\varphi_v^{ps}\rangle. \tag{2.28}$$

In this expression, $H = T + V$, $V^{ps} = V + \sum_c (E_v - E_c)|\varphi_c\rangle\langle\varphi_c|$, thus we obtain

$$(T + V^{ps})|\varphi_v^{ps}\rangle = E_v|\varphi_v^{ps}\rangle. \tag{2.29}$$

V^{ps} in the equation (2.29) is called the pseudopotential.

The goal of pseudopotentials is to generate the smooth and accurate pseudo-functions. It is not easy to construct pseudopotentials since they are nonlocal and depend on real eigenvalues. The common approaches to construction pseudopotentials include fitting experimental energy gap,[122] semiempirical model pseudopotentials, and ab initio norm-conserving pseudopotentials.[123] The latter one reproduces the all-electron wavefunctions out of cutoff radius, and real charge density in the whole space.

2.2   Time-dependent density functional theory

Although DFT gives a successful description of the ground state properties, it is less successful to describe the optical response and excitation spectra. Time-dependent density functional theory (TDDFT) is an extension version of DFT, which is used in calculation of excited states. The fundamental idea is to describe the excitations in terms of interacting electronic density. In the many-body problems, the response functions (the response of systems to external perturbation) is usually used in description of excitations. The basic formulas relating the response to the corresponding electronic properties are based on the perturbation theory and response functions. In the framework of current TDDFT,[117] we propagate the occupied Kohn-Sham eigenstates for subsequent time step by solving the time-dependent Kohn-Sham equation of the coupled electron-ion systems:

$$i\hbar\frac{\partial\Psi(\{\mathbf{r}_i\},\{\mathbf{R}_I\},t)}{\partial t} = H_{tot}(\{\mathbf{r}_i\},\{\mathbf{R}_I\},t)\Psi(\{\mathbf{r}_i\},\{\mathbf{R}_I\},t). \qquad (2.30)$$

H_{tot} is the time-dependent Hamiltonian of the multicomponent system[124] in the form of

$$\begin{aligned} H_{tot} &= -\sum_i \frac{\hbar^2}{2m_e}\nabla_i^2 - \sum_I \frac{\hbar^2}{2M_I}\nabla_I^2 + \frac{1}{2}\sum_{i,j,(i\neq j)}\frac{e^2}{|\mathbf{r}_i-\mathbf{r}_j|} \\ &\quad - \sum_{i,I}\frac{Z_I e^2}{|\mathbf{r}_i-\mathbf{R}_I|} + \frac{1}{2}\sum_{I,J,(J\neq I)}\frac{Z_I Z_J e^2}{|\mathbf{R}_I-\mathbf{R}_J|} + V_{ext}(\{\mathbf{r}_i\},\{\mathbf{R}_I\},t). \end{aligned} \qquad (2.31)$$

$\Psi(\{\mathbf{r}_i\},\{\mathbf{R}_I\},t)$ is the many-body wave function for the system. The definition of the parameters in the equations are the same as previous DFT section. The Runge-Gross theorem[125] states that the external potentials is one-to-one corresponding to the particle densities for a given initial many-body state $\Psi(\{\mathbf{r}_i\},\{\mathbf{R}_I\},t=0)$. It can be applied to both electronic and ionic system, consequently the external potentials for the electrons and ions are determined by their own densities, respectively. Therefore, the time dependent Kohn-Sham (TDKS) can be written as:

$$i\hbar\frac{\partial\phi_i(\mathbf{r},t)}{\partial t} = (-\frac{\hbar^2}{2m_e}\nabla_\mathbf{r}^2 + v_s[n](\mathbf{r},t))\phi_i(\mathbf{r},t), \qquad (2.32)$$

$$n(\mathbf{r},t) = \sum_i |\phi_i(\mathbf{r},t)|^2, \qquad (2.33)$$

$$i\hbar\frac{\partial\psi_I(\mathbf{R},t)}{\partial t} = (-\frac{\hbar^2}{2M_I}\nabla_{\mathbf{R}}^2 + v_s^I[n_I](\mathbf{R},t))\psi_I(\mathbf{R},t), \tag{2.34}$$

$$n_I(\mathbf{R},t) = |\psi_i(\mathbf{R},t)|^2. \tag{2.35}$$

where n and n_I in the expression is the density for the electrons and ions, respectively. The single-particle KS potential v_s and V_s^I includings the external potential, the Hartree potential, and the exchange-correlation potential depends merely on the corresponding density. Note that the electronic and ionic subsystems are decoupled in the exchange-correlation functionals in this approximation. However, the correlation between ions and electrons is of importance to obtain the accurate ionic wave functions and ionic energy separations, especially for photons.[126] By invoking the Ehrenfest theorem and classical trajectories for ions, the absence of explicit ion-electron correlation leads to Born-Oppenheimer-type dynamics for ground state simulations and correct vibration frequencies in both ground state and excited state, indicating that the ion-electron correlation is implicitly taken into account by Coulomb interactions. The expression for v_s and V_s^I is given by:

$$\begin{aligned} v_s[n](\mathbf{r},t) &= v_{ext}(\mathbf{r},t) - \sum_I \int d\mathbf{R}\frac{Z_I n_I(\mathbf{R},t)}{|\mathbf{r}-\mathbf{R}|} \\ &+ \int d\mathbf{r}'\frac{n(\mathbf{r}',t)}{|\mathbf{r}-\mathbf{r}'|} + v_{xc}[n](\mathbf{r},t), \end{aligned} \tag{2.36}$$

$$\begin{aligned} V_s[n_I](\mathbf{R},t) &= V_{ext}^I(\mathbf{R},t) + Z_I\sum_I \int d\mathbf{R}'\frac{Z_I n_I(\mathbf{R}',t)}{|\mathbf{R}-\mathbf{R}'|} \\ &- Z_I \int d\mathbf{r}\frac{n(\mathbf{r},t)}{|\mathbf{R}-\mathbf{r}|} + V_{xc}^I[n_I](\mathbf{R},t). \end{aligned} \tag{2.37}$$

We treat the ionic subsystems classically because ions are much heavier than electrons. The ionic TDKS equation can be derived by invoking Ehrenfest theorem. The classic ionic path $\mathbf{R}_I^{cl}(t)$ and forces $\langle\mathbf{F}_I(t)\rangle$ is defined as:

$$\mathbf{R}_I^{cl}(t) = \langle\psi_I(\mathbf{R},t)|\hat{\mathbf{R}}|\psi_I(\mathbf{R},t)\rangle = \int \mathbf{R}n_I(\mathbf{R},t)d\mathbf{R}, \tag{2.38}$$

$$\begin{aligned} \langle\mathbf{F}_I(t)\rangle &= -\langle\psi_I(\mathbf{R},t)|\nabla_{\mathbf{R}}V_s^I|\psi_I(\mathbf{R},t)\rangle \\ &= -\int n_I(\mathbf{R},t)\nabla_{\mathbf{R}}V_s^I[n_I](\mathbf{R},t)d\mathbf{R}, \end{aligned} \tag{2.39}$$

we obtain:

$$M_I\frac{d^2\mathbf{R}_I^{cl}(t)}{dt^2} = \langle\mathbf{F}_I(t)\rangle, \tag{2.40}$$

which recall Newton's second law of motion for the ionic degrees of freedom. The ion-ion exchange-correlation function is negligible, so we can ignore it and assume that the ionic density behaves as a $\delta-$function:

$$n_I(\mathbf{R},t) = \delta(\mathbf{R}-\mathbf{R}_I^{cl}(t)), \tag{2.41}$$

19

then, we obtain the simpler coupled ion-electron equations,

$$
M_I \frac{d^2 \mathbf{R}_I^{cl}(t)}{dt^2} = -\nabla_{\mathbf{R}_I^{cl}} [V_{ext}^I(\mathbf{R}_I^{cl}, t) - \int \frac{Z_I n(\mathbf{r}, t) d\mathbf{r}}{\left| \mathbf{R}_I^{cl} - \mathbf{r} \right|}
$$
$$
+ \sum_{I,J,(J \neq I)} \frac{Z_I Z_J}{\left| \mathbf{R}_I^{cl} - \mathbf{R}_J^{cl} \right|}], \tag{2.42}
$$

$$
i\hbar \frac{\partial \phi_i(\mathbf{r}, t)}{\partial t} = [-\frac{\hbar^2}{2m_e} \nabla_{\mathbf{r}}^2 + v_{ext}(\mathbf{r}, t) + \int d\mathbf{r}' \frac{n(\mathbf{r}', t)}{|\mathbf{r} - \mathbf{r}'|}
$$
$$
- \sum_I \frac{Z_I}{\left| \mathbf{r} - \mathbf{R}_I^{cl} \right|} + v_{xc}[n](\mathbf{r}, t)] \phi_i(\mathbf{r}, t). \tag{2.43}
$$

Therefore, the time-dependent evolution of a coupled ion-electron system can be described by equations (2.42) and (2.43). Within TDDFT, the evolution of electronic subsystems only depends on its density and the initial state with a total potential that contains a term describing the moving ions. The ionic subsystem, however, is treated classically, evolving along the Newtonian trajectories with forces which consider the electron effects by invoking Ehrenfest theorem and rest on the electronic density corresponding to either the ground state or the excited state. It is worth pointing out that the above derivation does not involve the Born-Oppenheimer approximation since the electronic and ionic subsystems evolve separately without finding the electronic ground state each time the ions move.

Optical properties of clusters and molecules from real-time time-dependent density functional theory

Optical excitation of finite-size structures like molecules and clusters is one of the most fundamental and versatile methods for investigating their structure and stability, since experimental measurements can be linked to the electronic structure by careful analysis of the excitation spectrum. Methods that can obtain very accurately the optical properties of very small systems of limited compositional variability do exist, however, these methods cannot be applied to large systems because of their very high computational cost. Methods that can handle large systems usually have to rely on approximations that sacrifice accuracy for the sake of efficiency, and can access the general trends of optical excitations but often miss the crucial details of small systems. In our work, we present an alternative approach bridging these two extremes, which should be a useful tool for investigating the optical properties of a wide range of finite-size systems.

This method is based on time-dependent density functional theory (TDDFT), which involves a self-consistent field for the propagation of the Kohn-Sham wavefunctions in real-time region. Although our approach does not provide a straightforward assignment of absorption features to corresponding transitions between Kohn-Sham orbitals, as in the case in frequency-domain TDDFT methods, it allows the use of larger timesteps while conserving total energy and maintaining stable dipole moment oscillations. These features enable us to study larger systems more efficiently.

3.1   Comparison with other methods

Model systems. In order to validate our approach, we apply it to the study of the optical properties of a representative group of small molecules, for which accurate experimental measurements exist. It includes fifteen small molecules: N_2, O_2, O_3, NO_2, N_2O, NH_3, H_2O, H_2CO, H_2CO_3, CO_2, CH_4, C_2H_2, C_2H_4, C_2H_6, and C_6H_6. In addition, application to a large atomic cluster, consisting of 220 Si and 144 H atoms, is also reported to demonstrate its efficiency. We choose these typical small molecules, because some of them, encountering in the Earth's atmosphere, play an important role in not only shielding living organisms from harmful solar ultraviolet (UV) radiation;[127–129] but also in modifying the composition of the atmosphere.[130–133] Some small hydrocarbons are crucial in the photochemistry of the Earth's upper atmosphere[132,134] and in various industrial application. The UV absorption of these molecules is of particular interest, since they are activated under UV light.

Quantum chemistry approaches. Theoretical studies, based on *ab initio* quantum chemistry approaches, such as configuration interaction (CI),[135] coupled cluster (CC),[136] and complete active space perturbation theory (CASPT),[137] can easily provide a complete description of the energies, geometries, and dynamics of excited states of these small molecules with sufficient accuracy and at a reasonable computational cost without invoking any important approximations. While the majority of previous such theoretical studies of small molecules focus on their atomic structure and electronic properties, some calculations for their excited states and photoabsorption spectra have also been reported.[138] These studies typically compare the excitation energies with experimental values but do not provide a detailed analysis of the relationship between absorption peaks and the corresponding electronic structure. As mentioned, these methods cannot usually be applied to large systems containing more than ∼100 atoms.

The frequency-domain TDDFT. An alternative approach employs density functional theory and its time-dependent version. The adiabatic approximation is usually employed in TDDFT approaches, and this is also the case in the present work. Compared to the high-level, computationally demanding methods, TDDFT in its current form has spectral accuracy close to that of the quantum chemical approaches,[139,140] and computational cost scaling as $O(N^3)$ with N being the size of a system, which is better than time-dependent Hartree-Fock theory.[141,142]

Traditionally, TDDFT calculations are performed in the frequency domain[143–146] within the linear response approximation to an external field of a given frequency. The absorption spectra and oscillator strength are obtained by calculating the poles of the density-density response function. This approach has proven very successful in reproducing the observed vertical excitation energies and oscillator strength of small molecules, and has been pursued extensively in the last decade with various approximations for the exchange-correlation energy functionals[147–150] and types of basis-sets.[148,151–153] In these cases, excited states in a small energy range, typically up to ∼10 eV, are calculated, since at higher excitation energies the number of fic-

titious electron-hole pairs increases significantly and the frequency-domain TDDFT calculations become very difficult.

Real-time TDDFT. In contrast to the frequency-domain formulation of TDDFT, real-time propagation of wavefunctions[154–157] can produce the full absorption spectrum by a single calculation, albeit at the cost of a large number of propagation timesteps.[154–156] In addition, the real-time approach has the advantage of automatically including non-linear effects since it does not rely on perturbation theory. A practical problem in real-time TDDFT calculations for finite-size structures, especially for polar ones such as water and ammonia, is that the electron density is very sensitive to the external field so that a very small timestep is needed to ensure the conservation of the total energy.

In our approach,[118, 158] we use local atomic basis sets and real-time propagation of wavefunctions for solving the time dependent Kohn-Sham equations with a self-consistent field (SCF), based on the adiabatic local density approximation. TDDFT simulations with a self-consistent field (SCF) are not new, and have been applied to electron dynamics[155] and implied in general procedure.[156] However, they have seldom been used for optical calculations[159] and their applicability in this domain has not been carefully examined. Our approach with SCF shows several important advantages: 1) nonlinear effects and strong electric fields can be applied; 2) reveal directly the information about the ultrafast dynamics of electrons and ions; 3) utilization of local basis sets maintains relatively high accuracy with the high efficiency, leading to a linear scaling (order-N) of the algorithm with respect to the number of electrons N; 4) absorption spectra and polarizability can also be obtained readily. All of these advantages makes it suitable for simulation of excited states dynamics for large systems.

3.2 Computational methods

Computational parameters. First-principle calculations are carried out with the SIESTA code.[160] We use pseudopotentials of the Troullier-Martins type[123] to model the atomic cores, and the Ceperley-Alder form[101] of the local density approximation for the exchange-correlation functional, as parameterized by Perdew and Zunger.[161] Periodic boundary conditions with box sizes of 7-13 Å to minimize interactions with periodic images are employed to calculate Hartree energies. An auxiliary real space grid equivalent to a plane-wave cutoff of 100 Ry is used. For geometry optimization, a structure is considered fully relaxed when the magnitude of forces on the atoms is smaller than 0.01 eV/Å. We use a basis of double-zeta polarized orbitals. For C, the basis set includes two radial functions to represent the $2s$ states with confinement radii r_s=5.12 a.u. and two additional $2p$ shells plus a d-type polarization shell for p electrons[162] with confinement radii $r_p = r_p^{Pol}$=6.25 a.u., so that the total number of basis functions for a C atom is $2 \times 1 + 2 \times 3 + 1 \times 5 = 13$. The use of additional polarization orbitals is necessary, since d polarization functions are essential for TDDFT excitation energy calculations.[153] For N atoms we use a similar basis of

13 orbitals, including two $2s$ shells, two $2p$ shells, and a d orbital for p-electron polarization with radii r_s=4.50 a.u., and r_p=$r_p^{Pol.}$=5.50 a.u., respectively. The number of orbitals for O is also 13, with two $2s$ shells, two $2p$ shells, and a d polarization shell with confinement radii r_s=3.93 a.u. and r_p=$r_p^{Pol.}$=4.93 a.u., respectively. For Si and P, thirteen numerical atomic basis: two $3s$ shells with r_s=5.01 a.u. and 4.56 a.u., two $3p$ shells and a $4d$ polarization shell with confinement radii r_p=$r_p^{Pol.}$=6.27 a.u. and 5.57 a.u., respectively, are considered. Finally, two radial shapes for the $1s$ orbital and a p-type polarized orbital with confinement radii r_s=$r_s^{Pol.}$=6.05 a.u are employed for H.

For the optical absorbance calculation within our modified TDDFT scheme, the Crank-Nicholson operator,[118] a timestep of 3.4×10^{-3} fs and 6107 steps to propagate the wavefunctions for all molecules, which gives an energy resolution of 0.1 eV. The perturbing external electric field we add on all the molecules is 0.1 V/Å. For the O_2 and NO_2 molecules, spin polarization is used to calculate the optical absorbance spectra. All calculations are performed in vacuum.

Procedure of calculation. We have modified the TDDFT scheme, used in earlier work to calculate optical absorption of small biological molecules like DNA bases[117,163] based on linear response, to include a self-consistent time propagation of the electron density. This approach, when applied to a photoabsorption calculation which is essentially within the linear response regime, proceeds as follows: At time t=0, an initial diagonalization step is performed to obtain the Kohn-Sham wavefunctions for each orbital under a perturbative external electric field. The resulting KS eigenstates are denoted as $\{\phi_j(0)\}$, where j is the index of the occupied states. At $t > 0$, the external field is switched off and the KS orbitals are allowed to evolve. The time propagation of $\{\phi_j(t)\}$ is realized by multiplying it by the propagator $\exp(-i\mathcal{H}[\rho, t_n] \Delta t)$, at the nth step $t_n = n\Delta t$:

$$\phi_j(t_n + \Delta t) = \exp(-i\mathcal{H}[\rho, t_n] \Delta t) \ \phi_j(t_n). \quad (3.1)$$

Here $\mathcal{H}$ is the DFT single-particle hamiltonian, including the kinetic energy operator, $-\frac{\hbar^2}{2m}\nabla^2$, and the electron-electron, electron-ion, and ion-ion interactions; ρ is the time-dependent density of electrons, $\rho(t) = \sum_j |\phi_j(t)|^2$, which enters the Hartree term (electron-electron repulsion) and the exchange-correlation term of the the hamiltonian. The propagation of KS orbitals is based on the variation of TDDFT action functions in the adiabatic approximation. The detailed description of the self-consistency loop was presented in Ref. [118].

In the present work, the assignment of absorption peaks obtained from TDDFT to specific excitation transitions in the molecular electronic structure was obtained by comparing to the peaks of the joint density of states weighted by the magnitude of the transition dipole moments calculated from DFT:

$$S_{\text{DFT}}(\omega) = \frac{2m\omega}{3e^2\hbar^2} \sum_{i,j} n(\varepsilon_i) \ (1 - n(\varepsilon_j)) \ \delta(\omega - \varepsilon_i - \varepsilon_j) \ |t_{i \to j}|^2 \quad (3.2)$$

where $S_{\text{DFT}}(\omega)$ is the optical oscillator strength based on fictitious KS orbitals, e and m are the charge and mass of the electron, $n(\varepsilon_{i,j})$ is the occupation of the KS eigen-

state i (j) with energy $\varepsilon_{i,j}$, with the indices i and j running over occupied and unoccupied states, respectively. $t_{i \to j}$ is the transition dipole moment between the Kohn-Sham orbitals $\phi_i(\mathbf{r})$ and $\phi_j(\mathbf{r})$ in the ground-state configuration of the molecule, given by:

$$t_{i \to j} = <\phi_j(\mathbf{r}) \mid \mathbf{r} \mid \phi_i(\mathbf{r})> \qquad (3.3)$$

The DFT calculations give main peaks of the optical absorption spectrum which exhibit a pattern similar to that obtained from the real-time TDDFT simulation. In the DFT calculation, the peak position is the energy difference between a pair of KS orbitals and the intensity is proportional to the square of the TDM.

Advantages of the self-consistency loop. The TDDFT density evolution with the self-consistency loop increases significantly the stability of the simulation, therefore a longer timestep can be used. To illustrate these features, we report the results for the optical absorption spectrum of quinone-imine, an interesting biomolecule which is a key component of melanin.[164] This molecule has a small optical gap. In Fig. 3.1a we compare the total energy of this molecule as a function of time during time evolution *with* and *without* the self-consistency loop. In the regular time-propagation scheme without the self-consistency loop, the larger the timestep we use, the sooner the total energy of the system diverges. When self-consistency is imposed by the scheme described above, we find that it leads to excellent total-energy conservation, with variations smaller than 1.5 meV (or 0.06% of the total energy) after 40 fs.

The TDDFT propagation with a self-consistent field also results in long-time stability of the dipole moment oscillations of the system, which is particularly important for the low energy excitations. Stable dipole moment oscillation is maintained for a time interval exceeding 40 fs with SCF, while it starts to diverge at $t = 12$ fs without SCF (see Fig. 3.1b). As a result, the optical spectrum obtained from the Fourier transform of the dipole moment evolution is well converged with SCF, while the spectrum without SCF shows broader distribution and much more noise (Fig. 3.1c). Although the optical absorption of this molecule has not been directly measured, its very small optical gap of 0.9 eV (1378 nm) is consistent with the energy gap measured at 1.2±0.2 eV in melanin samples.[165] The second peak at 2.73 eV (454 nm) also agrees with the measured peak at 2.88 eV in melanin intermediates.[164] The computational cost for TDDFT with SCF is only ~ 2 times that without SCF on average. As a result, the efficiency of the optical spectrum calculation is greatly enhanced, since the self-consistency loop allows a much larger timestep (by an order of magnitude or more). In addition, the longer total time span T of the simulation without energy divergence leads to enhanced resolution ΔE in the optical spectrum, since $\Delta E \sim h/T$ with h being Planck's constant. On the other hand, the timestep can not be arbitrarily large because it then washes out the fast oscillations of the dipole moment, thus removing high-energy features of the absorption spectrum.
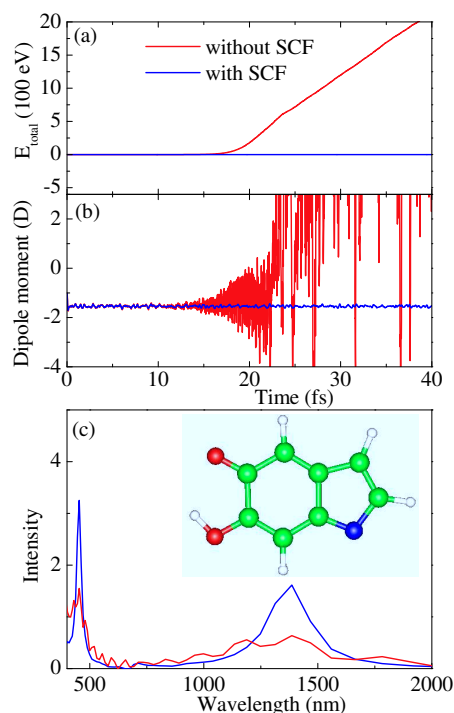
Figure 3.1: (a) Total energy; (b) dipole moment; and (c) optical spectrum of the quinone-imine molecule (structure shown in (c) inset), *without* (red lines) and *with* (blue lines) the self-consistency field (SCF) in TDDFT (for computational details see text).

3.3 Results and discussion

Large $Si_{220}H_{144}$ cluster. We begin with an example which clearly demonstrates the computational efficiency of our self-consistency scheme through the calculation of the optical absorption spectrum of a rather large system ($Si_{220}H_{144}$) by the present standards. The relevant structure of Si nanocrystals, exhibiting an approximately spherical shape with a diameter of 2 nm is shown in Fig. 3.2. This size range attracts more attention recently because of their potential applications in nano-scale devices. Issues related to their electronic and optical excitations are of central importance in their potential usefulness(see, for example, Ref. [166]). Therefore, being able to calculate the optical and electronic spectrum of such structures efficiently and accurately becomes of paramount importance in determining their properties. The optical spectrum of this model Si nanocrystal is shown in Fig. 3.2. The calculation required 2100 steps (with a timestep $\Delta t = 0.0102$ fs) and a total computational time 140 cpu hours on an Opteron single-node. The calculated overall shape and optical gap of $\sim$3.0 eV are consistent with previous calculations and experiments on clusters of similar size (2.6-3.2 eV).[167, 168] More details and examples are described in our paper.[158]

    The small molecules. We next consider the small molecules mentioned in the introduction, for which detailed experimental and theoretical results are readily available for comparison. Based on the different chemical composition and complexity
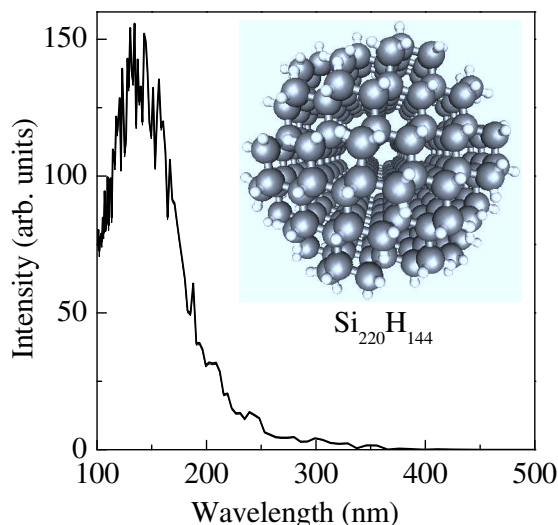
Figure 3.2: Optical spectrum of the $Si_{220}H_{144}$ cluster obtained from TDDFT with the SCF. Atomic structure is shown in the inset, with grey spheres representing Si atoms and white spheres representing H atoms.

of the molecules we studied, we divide them into four groups: Group I, consisting of N_2, O_2, and O_3, are the simplest elemental molecules; Group II, NO_2, N_2O, NH_3, and H_2O, are the simple bi-elemental compounds composed of N, O, and H; Group III, H_2CO, H_2CO_3, and CO_2, are the carbon oxides; and Group IV, CH_4, C_2H_2, C_2H_4, C_2H_6, and C_6H_6, are the hydrocarbons. The ground state geometry for each of these molecules is shown in Fig. 3.3.

A compilation of optical absorption spectra for representative cases is shown in Fig. 3.4.

Group I: The O_2 and N_2 molecules show two dominant absorbance bands in the UV region. The positions of the second peak for both molecules are very close, around 83 nm, though with very different intensity. The first peak for O_2 is located at 139 nm, different from that for N_2, which is at 95 nm. The differences can be attributed to features of the electronic structure of the two molecules: the strong triple-bond between the two N atoms in N_2 is related to the stronger absorbance at the higher energy (83 nm), while the presence of the triplet electronic states in O_2 results in a lower-energy transition at 139 nm.

Group II: The first peak of the N_2O molecule, compared to the first peak of N_2, is red-shifted to 112 nm, due to the presence of the O atom. The other two peaks are located at similar positions as those for N_2, suggesting a similar origin in electronic transitions. Overall, the oscillator strength (intensity) is enhanced relative to N_2, indicating a larger polarizability in this region. In the NO_2 molecule, the first peak has a large shift to 367 nm with a small intensity, and the other three absorbance bands are evenly distributed in the region from 100 nm to 160 nm.

Group III: For the H_2CO and H_2CO_3 molecules, the trends for the intensity of the first four bands are similar in both cases, that is, alternating large-small-large-

27
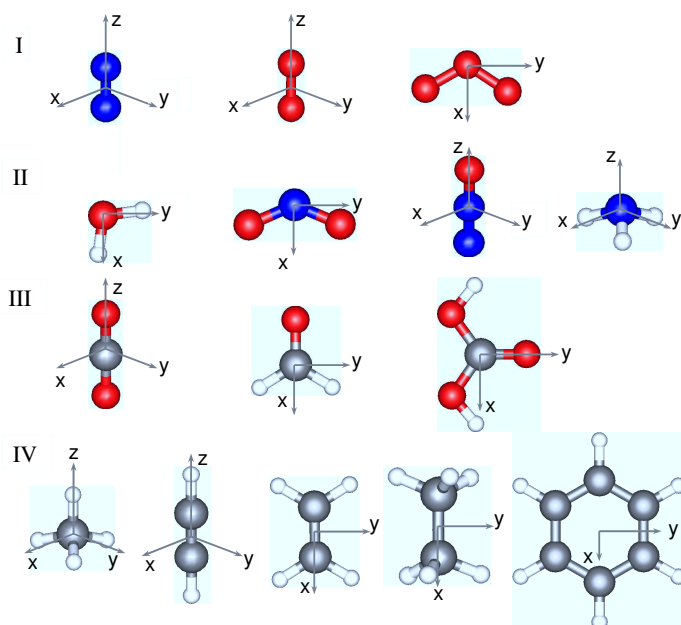
Figure 3.3: The geometry of the fifteen small molecules studied, in four groups (I–IV) as discussed in the text; Group I: N_2, O_2, O_3; Group II: H_2O, NO_2, N_2O, NH_3; Group III: CO_2, H_2CO, H_2CO_3; Group IV: CH_4, C_2H_2, C_2H_4, C_2H_6, C_6H_6. Red, white, gray, and blue spheres denote the oxygen, hydrogen, carbon, and nitrogen atoms, respectively.
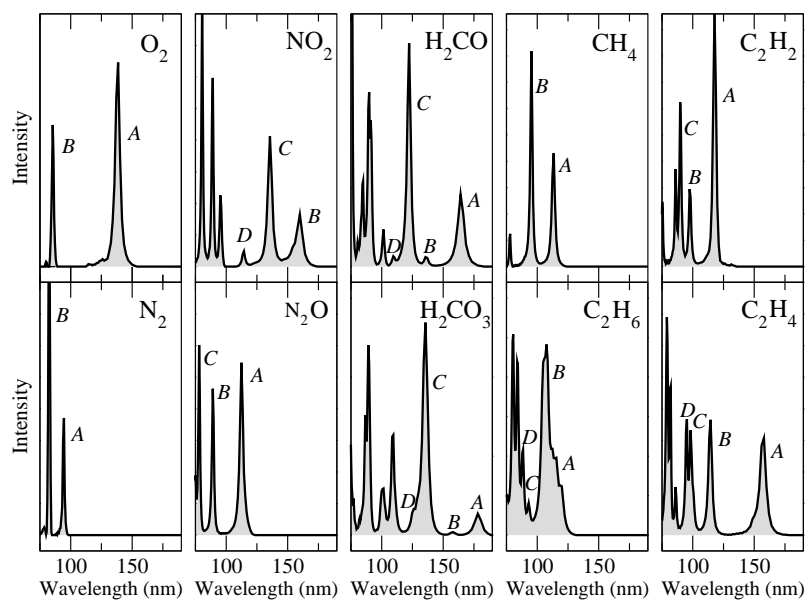
Figure 3.4: The calculated absorption spectra for several small molecules in the 80 nm to 200 nm range. For NO_2, the first absorption peak, A, lies outside the range shown.

small peaks with decreasing wavelength. With the presence of more O atoms, the peaks of H_2CO_3 are red-shifted by $\sim$14 nm, accompanied by a sharp decrease in the intensity of the first peak.

Group IV: Two peaks, at 95 nm (13.02 eV) and 113 nm (10.93 eV), are prominent in the UV spectrum of the simplest of the hydrocarbon molecules, CH_4. They are close to experimental values[169] of 13.6 eV and 10.4 eV. It seems that the first peak in experiment at 9.6 eV is missing or mixed with the peak at 10.93 eV in Fig. 3.4. The calculated oscillator strength for the first peak, integrated from 106 nm to 124 nm, is 0.401, in very good agreement with experimental value 0.4.[170] In literature the low energy excitation in CH_4 at 9-11 eV has been assigned to Rydberg transitions to states that involve C $3s$ orbitals.[171] The explicit inclusion of C $3s$ orbitals in basis-set, however, does not change the spectrum at low energy <15 eV in the present work. This question is open to further investigation. C_2H_6 has similar peaks in its absorption spectrum to those of CH_4, except that each peak is split into two due to the presence of two CH_3 groups connected by a C-C bond and smeared out. The optical spectra of molecules C_2H_4 and C_2H_6 exhibit similar overall trends. The C=C double bond in the C_2H_4 molecule leads to a large red-shift in the position of the first band compared to the C_2H_6 molecule, and the other three peaks are red-shifted by a smaller amount. Compared to the spectrum of C_2H_4, the C≡C triple bond of C_2H_2 results in a large increase in intensity for its first absorption peak without significant change in the peak position. However, a new peak with a significant red-shift is present at 158 nm for the case of C_2H_4, due to the transition from a triple bond to a double bond. At higher energy, absorption peaks show similar features for the two molecules C_2H_2 and C_2H_4. The calculated excitation energy (158 nm) and oscillator strength (0.324) for the first peak of C_2H_2 are very close to corresponding experimental values (161 nm and 0.30, respectively).[170]

We also compare our theoretical excitation energies obtained from TDDFT with available experimental values. More importantly, our results represent a complete set of electron excitations within a consistent theoretical treatment, which provides not only the unbiased excitation energies but also the corresponding transitions between electronic states, TDMs and number of excitation channels. This information can help interpret optical spectra measured in experiment and the electronic properties of these molecules. More details of the corresponding absorption bands, transitions, and dipole moments for these molecules are presented in Ref [158].

Water molecule. The simplest case we considered is H_2O molecule as an example to analyze in detail the spectral features, the corresponding wavefunctions, the electronic excitation channels, and TDMs, as presented in Table 3.1.

The H_2O molecule exhibits four major absorption bands with wavelength in the range of 80 to 250 nm, shown in Fig. 3.5a, together with the DFT peaks of $S_{DFT}(\omega)$, which in the case of this molecule happen to be in rather good agreement. The first two peaks are at 164.2 nm (7.553 eV) and 127.9 nm (9.740 eV), respectively. In experiment, the primary photoabsorption peaks of gaseous H_2O are centered at 7.447 and 9.672 eV,[128] in excellent agreement with our calculations. The oscillator strength for the first peak, calculated at 0.036, is also very close to the experimental

Table 3.1: Absorption bands, corresponding transitions between electronic states, and transition dipole moments for H_2O molecule. Molecular axial directions are defined in Fig. 3.3 (Group II).

| | Band | E_{abs}(eV) | | Assignment | Transition dipole moments | | | |
		Exp.	The.		D_x	D_y	D_z	N
H_2O	A	7.45^{128}	7.55	H$\to$L	0	0	0.32	1
	B	9.67	9.74	H–1$\to$L	0.39	0.39	0	1
	C		11.93	H–1$\to$L+1	–0.32	0.32	0	1
	D		13.72	H–2$\to$L	0.51	–0.51	0	1
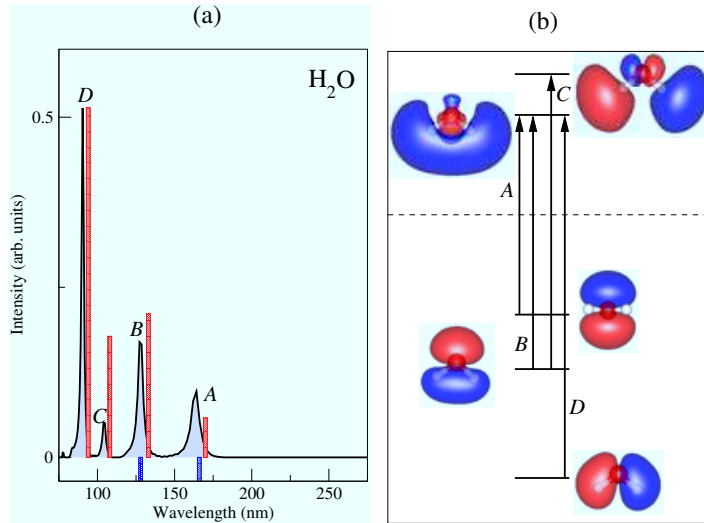
Figure 3.5: (a) Absorption spectrum of H_2O molecule. The red bars represent the peaks of $S_{DFT}(\omega)$, Equation (3.2), which help identify the nature of the TDDFT peaks, and are scaled so that the heights of the dominant peak (*D*) from the two calculations match. The small blue bars below the zero intensity line indicate the position of experimental peaks. (b) Energy level diagram and transitions corresponding to the absorption peaks. For each energy level, the corresponding wavefunction is shown as blue (positive) and red (negative) iso-electronic contours. The letters in (b) identify the transitions that correspond to labelled peaks in (a). Black vertical arrows represent single-channel electronic transitions between two states.

value of 0.03.[170] The other two peaks in our calculation are located in the higher energy region: at 104.5 nm (11.926 eV) and 90.3 nm (13.715 eV), respectively. They are mixed with the Rydberg series with significant vibronic features in experimental measurements. In order to demonstrate the relationship between optical absorption and the electronic structure, we explore in detail the relevant state transitions in water, as shown in Fig. 3.5b. The first absorption peak, A, is attributed to the HOMO→LUMO transition. The HOMO, often referred to as the $1B_1$ molecular orbital, is primarily composed of O $2p_z$ orbitals. The LUMO, the $4A_1$ orbital, however, is primarily composed of the $1s$ orbital from the two H atoms and the $2s$, $2p_x$, and $2p_y$ orbitals from the O atom, with the H $1s$ contribution being dominant. Therefore, the first absorption peak has $1B_1$→$4A_1$ character. The calculated TDM in Table 3.1 shows that the orientation of the electronic arrangement aligns along the z direction. The second absorption band, B, is ascribed to the H−1→LUMO transition. The electronic orbital assignment of the H−1 state, the $3A_1$ orbital, is similar to the LUMO, except that the linear combination has equal contributions from all orbitals. Therefore, the second absorption peak corresponds to the $3A_1$→$4A_1$ transition. From the TDM analysis we find that the electrons are polarized along the diagonal direction of the x-y plane. The third peak, C, in Fig. 3.5a results from the contribution of electron excitation from the H−1→L+1 state. In the L+1 state, with $2B_2$ character, the $1s$ orbital of the two H atoms also dominates the wavefunction, in combination with the contributions from O $2p_x$ and $2p_y$ orbitals. In the H−1→L+1 transition, which has $3A_1$→$2B_2$ character, the electron is distributed on the diagonal direction in the x-y plane with a change of sign in the x direction. The fourth absorption peak, D, is related to the H−2→LUMO transition. The H−2, $1B_2$ orbital, is the linear conformation of the H $1s$, O $2p_x$, and O $2p_y$ orbitals. The orientation of electronic charge of H_2O for the $1B_2$→$4A_1$ transition is located in the diagonal of the x–$(-y)$ plane.

Biological systems: Complexation of flavonoids with iron

It is well known that flavonoids, the potent antioxidants, can be used in pharmacology fields, because their powerful ability of scavenging free radicals and metal ions chelation can prevent effectively from oxidative damages. Special attention has been paid to study the metal ions chelation mechanisms of flavonoids with Fe ions, the most abundant metal element in a human body. Several investigations have emphasized that the biochemical activity of metal-flavonoid complexes depends strongly on the number of hydroxyl (OH) groups, the relative position of the OH groups on the different rings of flavonoids, and the metal chelation sites.[15–17] Despite extensive efforts, the atomic structure of metal-flavonoid complexes and binding mechanism are far from understood, primarily attributed to experimental difficulties in detecting these complexes with molecular resolution in solution.[18–20] In this work, we dedicate in studying the complexation mechanism of several flavonoids with Fe using first-principles calculations based on density functional theory (DFT).

4.1 Models and computational details

In order to study the complexation mechanism, we choose several flavonoid molecules as model systems, including quercetin (Que), luteolin (Lut), kaempferol (Kae), galangin (Gal), and chrysin (Chr). All of these flavonoid molecules are composed of two aromatic rings (A and B) and an oxygenated heterocyclic ring (C), as shown in Fig. 4.1 for Que molecule, the $3,5,7,3',4'$-pentahydroxylflavonol. Others just differ in the number and position of OH groups in these rings, for instance, Lut, $5,7,3',4'$-OH; Kae, $3,5,7,4'$-OH; Gal, $3,5,7$-OH; Chr, $5,7$-OH. Depending on the number and sites of the OH groups they contain, the relevant antioxidant capacity is different, which can help us to understand the relationship between the chelation sites and an-
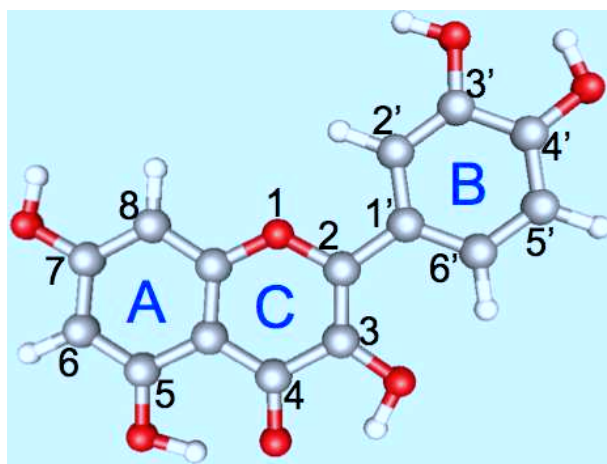
Figure 4.1: Geometry and numbering of a quercetin molecule. C, H, and O atoms are shown as gray, white, and red spheres, respectively.

tioxidant activity. Furthermore, the different chelation sites are tightly related to the binding strength based on complexation with Fe ions, which can be used to predict the trend of scavenging ability for these typical flavonoid molecules.

The first-principle calculations are carried out with the SIESTA code, and the computational details are discussed in Chapter 3.

4.2 Structural dependence of antioxidant activity

Two main mechanisms to explain the antioxidant activity of flavonoids were widely discussed in the literatures.[172,173] First, the deprotonation makes flavonoids become nonreactive phenoxyl radicals, which can interrupt the chain reaction:

$$R^{\bullet} + ArOH \rightarrow RH + ArO^{\bullet} \tag{4.1}$$

In this mechanism, the bond dissociation enthalpy of the OH bond plays an essential role in determining the antioxidant activity. The weaker the OH bond the easier the reaction occurs. Second, the one-electron transfer mechanism, the antioxidant can deactivate a free radical by transferring an electron to form a stable radical cation:

$$R^{\bullet} + ArOH \rightarrow R^{-} + ArOH^{\bullet+} \tag{4.2}$$

In this case, the ionization potential is of importance in evaluating the antioxidant action. The lower ionization potential facilitates the electron abstraction.

Unfortunately, another antioxidant mechanism, based on chelation of metal ions to form stable complexes, is still not clear. In fact, the ability of scavenging metal ions, especially for iron, copper, and other transition metal ions, for flavonoids plays a crucial role in protecting our body from oxidative damages, and largely enhance the antioxidant capacity of pure flavonoids.

4.2.1 Chelation sites

Bors first proposed the three important criteria for effective radical scavenging:[8, 174] (1) the *ortho*-dihydroxy (catechol) structure in the B ring can confer higher stability of radicals and involve in electron delocalization; (2) the 2,3-double bond in conjugation with a 4-oxo function in the C ring is responsible for electron delocalization from the B ring; (3) the additional presence of the 3- and 5-OH groups in the A and C rings largely accounts for maximal radical scavenging potential and the strongest radical adsorption.

In addition, the numbers and positions of the OH groups also determine the potency of scavenging metal ions for flavonoids. Quercetin, one member of a flavonoid family, exhibits potent radical-scavenging activity and strong antioxidant ability, because it meets all of these conditions. Flavonoids can chelate metal ions by removing one H atom, however, the ordering of chelation site is still in debate. Some papers proposed that the first preferential site in the complexation process is the 3-OH group, and the second one is the *ortho*-dihydroxyl group.[3, 16, 19, 175] But others hold the opposite opinions, which means the first site is the *ortho*-dihydroxyl group and then the 3-OH group.[18, 20, 176, 177] In this chapter, we try to address which chelation site is the most preferential site for chelating Fe ion in the complexation with the five flavonoids mentioned above.

We analyze in detail the structure and properties of quercetin, which has the largest number of OH groups, and thus has the highest degree of variability in terms of complexation with metals. For the other flavonoids consider here, we will mostly point out the difference and similarities with quercetin. In optimized geometry of pure quercetin, the hydrogen atoms in the hydroxyl groups at positions 3, 5 and 4′ are arranged so as to allow for hydrogen bond formation to the nearby O atoms (of the doubly-bonded O at position 4, and of the hydroxyl group at position 3′). The calculated bond length between C4=O4 is 1.279 Å [1.267Å], between C10-C4 is 1.419 Å [1.418Å], and between C2-C1′ is 1.456 Å [1.479Å]; these are all in good agreement with the corresponding experimental values[178] given in parenthesis.

In the complexation process, we consider two H reservoirs to define the chemical potential for the removed H atoms: one is corresponding to H_2 molecules (energy gain of 2.34 eV per H atom) and the second to H_2O molecules (3.04 eV per H). According to the choice of reservoir, the relevant binding energy of the complex is defined as

$$E_b = E_{total} - n_{Fe}E_{Fe} - n_{Que}E_{Que} + n_H E_H + n_H \frac{1}{2}E_{H_2} \qquad (4.3)$$

$$E_b' = E_{total} - n_{Fe}E_{Fe} - n_{Que}E_{Que} + n_H E_H + n_H \frac{1}{2}(E_{H_2O} - E_H - E_{OH}) \qquad (4.4)$$

where E_{total} is the total energy of the complex and E_X, n_X, are the energy and number of species X involved in the complexation reaction (X = Fe, Que, H); in particular, n_H is the number of H atoms missing from the neutral Que molecules after complexation, and E_{H_2} is the binding energy per H_2 molecule.

For a single flavonoid molecule, there are several possible sites that could bind an iron atom. We classify the chelation sites by binding energy calculated using

the H_2 molecule as a reservoir for the removed H atoms. The most favorable one are shown Fig. 4.2a-c for quercetin. The corresponding binding energy is 2.09 eV,
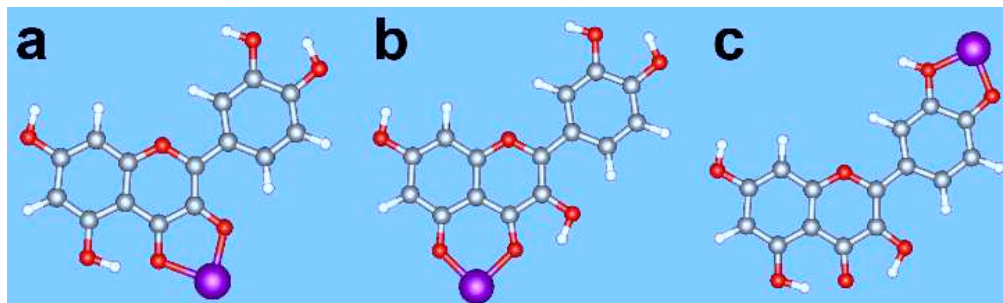

Figure 4.2: Configurations of Fe-quercetin complexes at ratio of 1:1 for Fe and quercetin. The Fe-Que complex with Fe (denoted by a purple sphere) at the 3-4 site (a), at the 4-5 site (b), and at the $3'_H$-$4'$ site (c).

1.87 eV, and 1.64 eV per complex (see Table 4.1, E_b), respectively. Our results indicate that the preferred site for Fe chelation is the 3-OH and 4-carbonyl group (denoted as 3-4 site). The attachment of the Fe atom to the molecule breaks the double bond of the 4-carbonyl group and deprotonates the 3-hydroxyl group to form the two Fe-O bonds. The next site is the 4-5 site, however, it is less likely not only because of kinetics: deprotonation of the 5-OH group requires 0.5 eV more energy than that of the 3-OH group, but also steric repulsion and H-bond formation after Fe binding at 3-4 site.

The next available site is $3'$-$4'$ site. Here, either one or both H atoms can be removed from the $3'$- and $4'$-hydroxyls, denoted as $3'_H$-$4'$, $3'$-$4'_H$, $3'$-$4'$ sites, respectively, in Table 4.1. Therefore, our results suggest the Fe-Que binding strength at different chelation sites has the order 3-4 > 4-5 > $3'$-$4'$. For the complex with two Fe atoms, binding to the 3-4 and $3'$-$4'$ sites simultaneously, the binding energy (3.4−3.6 eV) is considerably smaller than twice that of one Fe-Que with Fe bound at the 3-4 site (4.2 eV). In addition, the same trend is found in Cu-Que complex.[179]

Other possible chelation sites, such as the 7-hydroxyl, have a lower binding energy ~1.3 eV per complex. The 1-oxygen and 4-carbonyl have much lower binding energies (<0.4 eV) and will not not be considered further. Furthermore, experimental measurements of ^{1}H Nuclear Magnetic Resonance (NMR) spectra[18] show that the signal for the proton of the 3-OH group disappears after the Fe-Que complex is formed, which confirms the importance of the 3-hydroxyl-4-carbonyl site (Fig. 4.2a) as the preferred site for Fe chelation.

The same trends apply for complexation of other flavonoids (Lut, Kae, Gal and Chr) with Fe. Our results show that for all flavonoids investigated, the Fe binding energies are around 2.06−2.09 eV for the 3-4 site, and 1.84−1.88 eV for the 4-5 site, 1.6 eV for the $3'_H$-$4'$ site or the $3'$-$4'_H$ (with one H remaining on the $3'$ or $4'$ hydroxyl sites), and less than 1.3 eV for other sites, using the first H reservoir. This suggests that there is a universal trend for Fe-flavonoid complexation: the 3-4 site is the most favored site if present; otherwise the 4-5 site also binds Fe strongly; then the $3'$-$4'$
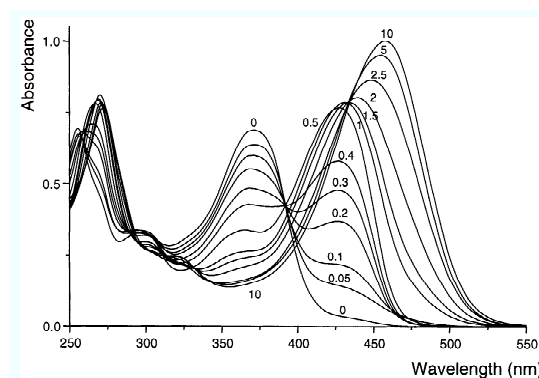
Figure 4.3: Electronic absorption spectra of quercetin in methanol in absence and in presence of Al(III). The molar ratios [AlCl$_3$]/[Q] are indicated on each spectrum, from Ref. [16].

site. The comparison of energy and structural characteristics of these complexes contained in Table 4.1 leads to the following ordering in Fe chelation ability:

$$Que > Lut > Kae > Gal > Chr,$$

which agrees with experiments.[180–182]

4.2.2 Stoichiometry of the complexes

Complexes with a wide range of stoichiometry of metal/flavonoids were investigated by the UV-vis absorption spectra and electrospray mass spectrometry.[16, 20, 175, 182] Different metal-flavonoid complexes exhibit distinct stoichiometry of metal/flavonoid from 1:1, 1:2, 2:1 to 1:3[10, 16, 19, 20, 175, 182], in terms of chelation sites, environment, and metal ion concentration. Fig. 4.3 shows electronic absorption spectra of Al-Que in methanol with increase of the concentration of metal ions.[16] It is clear that with the increase of ratio of metal ions, the first absorption band shift largely, indicating the formation of complexation. However, the general complexation mechanism at different ratios and the optimal stoichiometry for the metal-flavonoid complexes is far to understand.

To this end, we consider higher quercetin concentration for the Fe/Que complexes. At the ratio of Fe/Que=1:2, three highly symmetric structures are presented in Fig. 4.4a-c. Two molecules are coplanar, with reflection symmetry for Fig. 4.4a, denoted as P_R; with inversion symmetry for Fig. 4.4b, denoted as P_I, respectively. Two molecules are perpendicular to each other with respect to Fe atom, denoted as O symmetry, as shown in Fig. 4.4c. The binding energies for Fe in these three structures, per complex, are 4.69 eV for the P_R structure, 4.72 eV for the P_I structure, and 4.78 eV for the O structure. The difference of binding energy suggests that the spatial symmetry plays a role in the Fe complexation process: the quercetin molecules prefer to be arranged on orthogonal planes. Furthermore, the binding energy in the same structure but with Fe bound at the 4-5 site is smaller by 0.36 eV per complex, indicating that in the complexes containing two quercetin molecules the 3-4 chela-
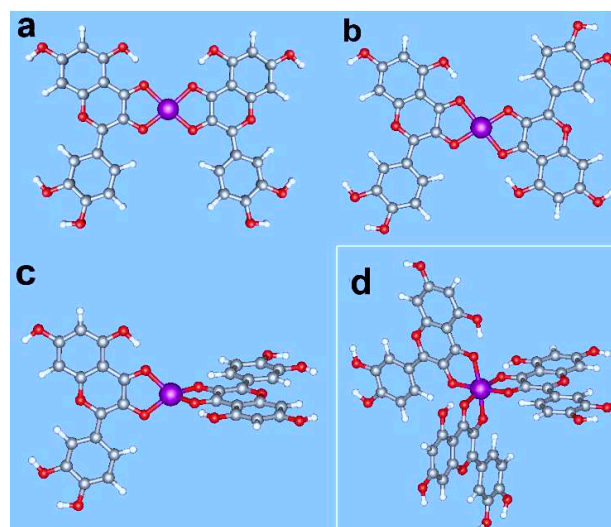
37

Figure 4.4: Configurations of Fe and quercetin complexes with higher concentration of quercetin. (a) Fe-2Que in P_R, a planar structure with reflection symmetry; (b) Fe-2Que in P_I, a planar structure with inversion symmetry; (c) Fe-2Que in O, a structure with the two molecules on orthogonal planes; (d) Fe-3Que with Fe having six covalent bonds. In (a)-(d), the Fe atom is at the 3-4 site of each molecule.

tion site is again preferred. These results are in general agreement with Ref. [17]: for instance, the orthogonal complex is favored over the planar complexes in vacuum.

At the ratio of Fe/Que=1:3, the planes of the three molecules are mutually perpendicular, as shown in Fig. 4.4d. In this structure, Fe is bound to the quercetin molecules by six Fe-O bonds in an octahedral configuration. The calculated binding energy of 6.47 eV per complex indicates that this structure is of stability comparable to that of the one- and two-Que complexes. However, the binding strength is the strongest in the two-Que complex, with an energy of 2.39 eV per Que molecule, compared with 2.16 eV per Que here in the three-Que complex, and 2.09 eV in the one-Que complex. This is consistent with experimental observations in the mass spectrometry, where metal-flavonoid complexes of stoichiometry 1:2 are usually preferred.[182] From these results we conclude that the Fe ions are chemically saturated when bound to three quercetin molecules. The high stability of Fe-3Que complex may have important and profound biological significance, as was revealed in a recent study that protection against intracellular DNA damage in the presence of peroxides dies when the Fe:Que ratio is larger than 1:3.[12]

4.2.3   Solvent dependence

The stoichiometry and preferential chelation sites of metal-flavonoid complexes will vary slightly, depending on different solution. In pure methanol, the 3-OH group exhibits the strongest chelation strength with 1:2 stoichiometry for Al-Que complex;[16] while in the presence of alkaline medium, the *ortho*-dihydroxyl group with the Al/Que ratio of 1:3 is more favorable. However, the Cu, Ni, Zn, Pb-Que complex
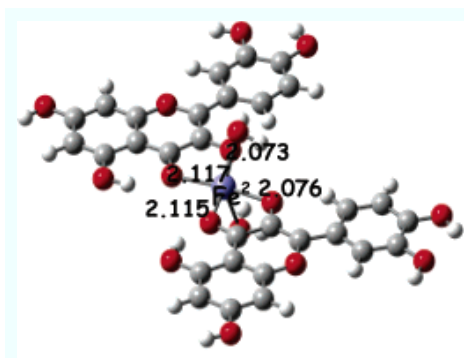
Figure 4.5: Optimized geometry of hydrated Fe-deprotonated quercetin (1:2 ratio) complex.[17]

presents the deprontation of the 3-OH group and stoichiometric ratio of metal/Que as 1:2 in the water.[175]

In our work, we choose H_2 and H_2O molecules in Eqn. (4.3 and 4.4) as H reservoirs to provide information of energetic favorable chelation site and the relevant stoichiometric ratio in an acidic and basic condition. For the first choice, the 3-4 site is the preferred chelation site; while for the second choice, the $3'$-$4'$ site with two H atoms removed becomes slightly more favorable. But the sequence of binding energy and the relative stability of complexes remain unchanged, when the same number of removed H atoms is involved. Furthermore, the water hydrated Fe-Que complex, as depicted in Fig. 4.5, confirms that the 3-4 site is preferred for both ratio of 1:1 and 1:2.[17] It is worth pointing out that the water molecules surrounded prefer to form the octahedral configuration with other four Fe-O bonds.

In addition, our study of the Cu and Que complexation[179] also approves the preferred chelation site of the 3-4 site under the gas phase and solvated by OH group and H_2O molecules. At pH 5.5 (acidic media), the 1:1 complex is responsible for spectroscopic features, while the 1:2 complex is mainly existed at pH 7.4, which is in good agreement with experimental findings.[183] Therefore, the Fe-O binding strength may be modified in the presence of water molecules, but we expect this to be a small change because the Fe-H_2O bond is relatively weaker than the covalent bonds between Fe and O responsible for the binding energies compared here.

4.3 Optical signatures

In experiment, the optical absorption of the molecules is used to identify changes in their structure and stoichiometric ratio, such as complexation with metal atoms. To address this issue, we calculate the optical properties of quercetin and its various complexes with Fe using TDDFT. The free quercetin molecule exhibits two major absorption bands as indicated in Fig. 4.6a. The first peak is at 390 nm and the second one at 283 nm. The primary peaks in the measured UV-vis spectra are at 372 nm and 256 nm.[16, 18] Our calculation for the optical absorption of quercetin is in good
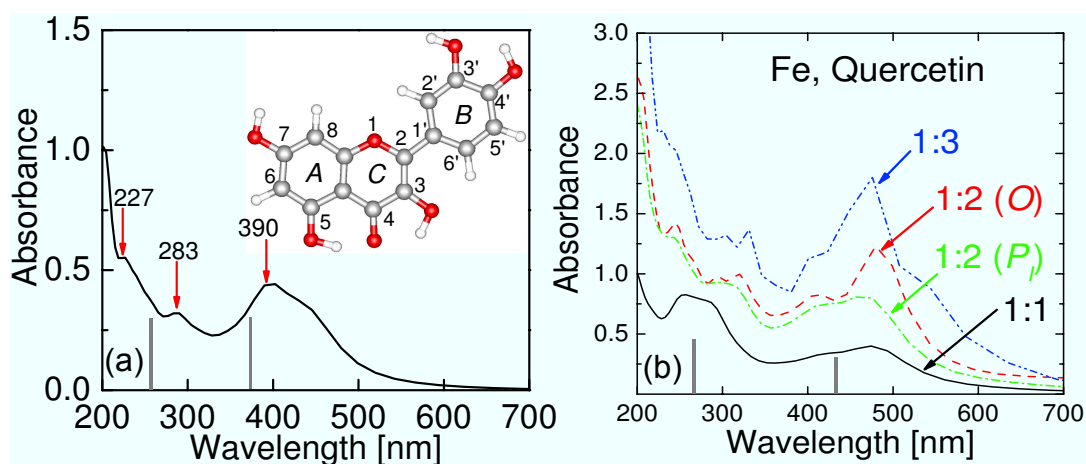
Figure 4.6: The UV-vis spectra calculated from TDDFT for pure quercetin molecule (a), and Fe-Que complexes (b). The ratio of Fe/Que concentration ranges from 1:1 to 1:3. P_I: planar geometry with inversion symmetry; O: orthogonal geometry (see text). The two vertical grey lines represent experimental peaks.

agreement with the experimental values, as shown in Fig. 4.6a.

For the Fe-Que (1:1 ratio) complex, the first absorption bands are red shifted with respect to the free quercetin molecule, as shown in Fig. 4.6b: the first two peaks are at 474 nm and 290 nm. With the increase of the concentration of quercetin molecules, the first absorption peak is almost at the same position at 470-480 nm, but the intensity is gradually enhanced with increase of the quercetin concentration. In addition, the relative intensity of the shoulder at 410 nm decreases and the the second band at around 300 nm shifts to longer wavelength. These intensity changes can be used to identify different stoichiometric ratios of the Fe-Que complex.

To elucidate the nature of the absorption peaks and the reasons for their shifts upon complexation, we analyze the electronic structure of the quercetin molecule and its complexes with Fe. The peak at 390 nm in the quercetin absorption spectrum is attributed to electronic excitations from the highest occupied molecular orbital (HOMO) of quercetin to the lowest unoccupied molecular orbital (LUMO). The wavefunctions of these states are presented in Fig. 4.7. The HOMO comprises mainly π bonding combinations while in the LUMO the antibonding combinations dominate. The HOMO is more localized at the C and B rings but the LUMO is delocalized from the B ring to the C2-C1$'$ bond and from the C2-C3 bond of the C ring to the C3-C4 and C4=O4 bonds. Therefore, the first absorption band has $\pi \rightarrow \pi^*$ character. The change of wavefunction distribution also indicates that the first band has contributions from both the B and C rings.

Compared to the free quercetin molecule, the HOMO of quercetin in the Fe-Que complex is more delocalized spreading over the C2-C3-C4 atoms, due to the presence of Fe. There exist two singly occupied molecular orbitals (SOMO) between the quercetin-related HOMO and LUMO states. These two states correspond to the $4s$ orbital of the Fe atom, for the majority spin, and the $3d_{z^2}$ orbital for the minority
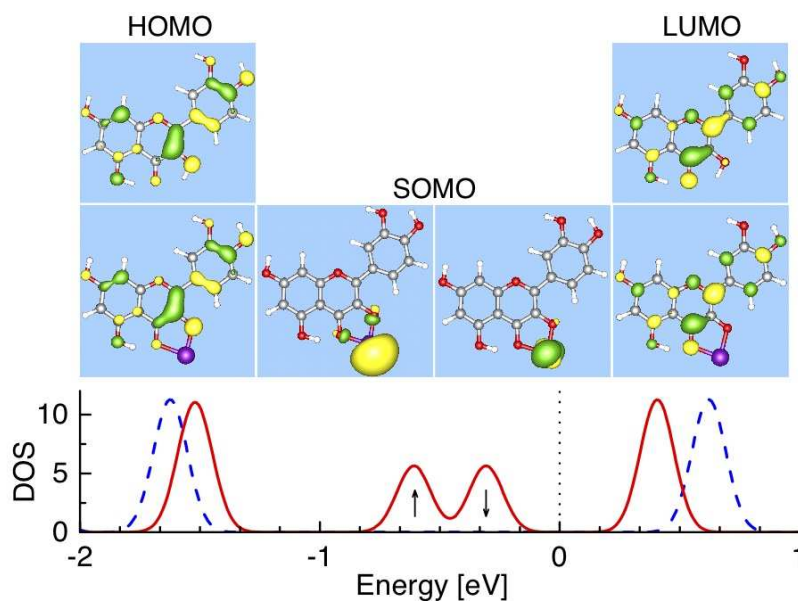
Figure 4.7: Density of states of the quercetin molecule (blue dashed line) and the Fe-Que complex (red solid line), for the configuration shown in Fig. 2a. The upper panels show the corresponding wavefunctions of these orbitals. The dotted vertical line indicates that the Fermi level. Arrows indicates the majority ($\uparrow$) and minority spin component ($\downarrow$).

spin. Consequently, the first absorption band should be around 1920 nm, which corresponds to transitions between the SOMO states related to the bound Fe atom and the LUMO state of the Que/complex, which is assigned to the ligand-to-metal charge transfer (LMCT).[17] However, this band will have very small intensity and will be difficult to detect in experiments. As a result, the first band at ∼430 nm in experimental UV-vis spectra reflects the transition between the HOMO and LUMO states associated with quercetin, as they have been modified by the presence of the Fe atom. From Fig. 4.7, it is obvious that the complexation with Fe moves the HOMO and LUMO states of quercetin closer in energy which accounts for the observed red shift in the first absorption peak.

Table 4.1: Energies and structural parameters for different Fe-flavonoid complexes[a].

Complex	Site	E_b(eV)	E_b'(eV)	N	d(Å)
Fe-Que	3-4	2.086	2.785	2	1.99
	4-5	1.870	2.569	2	1.95
	$3_H'$-$4'$	1.639	2.338	2	2.01
	$3'$-$4_H'$	1.624	2.323	2	2.02
	$3'$-$4'$	1.426	2.823*	2	1.90
	$3'$	1.364	2.063	1	1.80
	$4'$	1.367	2.066	1	1.81
	7	1.265	1.964	1	1.77
Fe$_2$-Que	3-4;$3_H'$-$4'$	3.585	4.982	4	2.00
	3-4;$3'$-$4_H'$	3.546	4.943	4	2.01
	3-4;$3'$-$4'$	3.370	5.466*	4	1.91
Fe-Lut	4-5	1.873	2.572	2	1.92
	$3_H'$-$4'$	1.667	2.366	2	2.02
	7	1.324	2.023	1	1.79
	$3'$-$4'$	1.191	2.588*	2	1.85
Fe$_2$-Lut	4-5;$3_H'$-$4'$	3.495	4.892	4	1.96
Fe-Kae	3-4	2.093	2.792	2	2.00
	4-5	1.877	2.576	2	1.96
	7	1.326	2.025	1	1.80
	$4'$	1.323	2.022	1	1.80
Fe-Gal	3-4	2.056	2.755	2	2.01
	4-5	1.842	2.541	2	1.93
	7	1.316	2.015	1	1.79
Fe-Chr	4-5	1.880	2.579	2	1.93
	7	1.290	1.989	1	1.80

[a] The iron binding energy (E_b and E_b', with respect to different reservoir choice for the removed H atoms, see text), number of Fe-O bonds (N), and average Fe-O bond length (d) are listed. H atoms are removed from the OH binding sites unless denoted with a subscript H. The cases in which the choice of reservoir makes a difference in the ordering of the binding energy are marked by an asterisk.

Dye Solar Cells: sensitizing inorganic nanowires

Dye-sensitized solar cells (DSSCs) are the promising alternatives to conventional solid state photovoltaic devices, due to the lower cost and more environment friendly. Recently, much attention has been particularly paid to natural dye, such as cyanidin, chlorophyll, and carotene, sensitized TiO_2 solar cells, because natural dye molecules are cheaper, simpler, and safer dyes in comparison with the sensitizer based on ruthenium polypyridyl complexes.[35, 38] In addition, the use of one-dimensional (1D) nanostructural materials including nanowires, nanorods, nanotubes, and nanoparticles, as the inorganic semiconductor in DSSCs provides good opportunities to reduce the size and improve the efficiency.[43] Despite intensive experimental and theoretical studies on surface-based (2D) and nanopartical-based (0D) DSSC, the mechanism and electronic interaction between the TiO_2 nanowire and natural dye molecule (cyanidin), has never been elucidated. In this chapter, we first compare the structure and properties of the two different kinds of semiconductor nanowires used in DSSC devices: the TiO_2- and GaAs-based nanowire. We will focus on demonstrating the electronic coupling between the cyanidin molecule and TiO_2 nanowire, and provide an insight into charge injection mechanisms of natural-dye sensitized nanowire solar cells.

5.1   Semiconductor nanowire

Semiconductor nanowires or nanotubes have attracted much attention because of their application in photovoltaic solar cells with high conversion efficiency. In comparison with the commonly used nanoparticles, nanowires (including nanotubes) exhibit additional advantages in two aspects: 1) visible light scattering and adsorption are much enhanced because of their long length-to-diameter ratio (about

30:1) and a total length reaching hundreds of nanometers; 2) due to highly oriented crystalline array, the 1D geometry facilitates faster electron transport to the electrodes, and slower charge recombination.[30, 184, 185] Furthermore, several synthesis approaches[185–187] can be used to control morphology of nanowires, including the diameter, wire length, structure, and interwire spacing, which are tightly related to the function and performance of DSSCs.

5.1.1 TiO$_2$ nanowire

Among the inorganic semiconductors, TiO$_2$-based nanostructures have been used most often as a wide bandgap semiconductor in DSSCs, due to their superior photoreactivity, nontoxicity, long-term stability, low price, and easy production.[39, 188, 190] In general, two different crystal structures of TiO$_2$, rutile and anatase phase (see Fig. 5.1), are used in photocatalysis.[189] It is commonly believed that the anatase
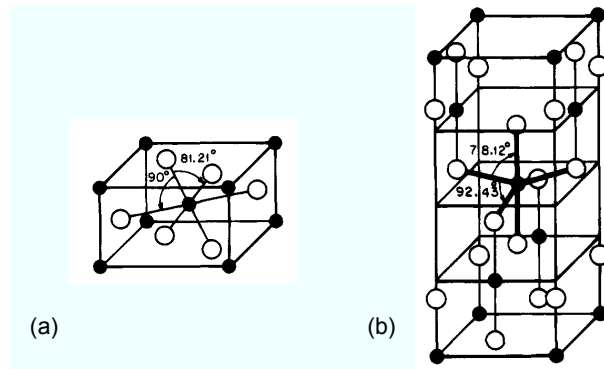

Figure 5.1: Geometry of rutile phase (a) and anatase phase (b) of TiO$_2$ crystal, from Ref. [189]. Black and white spheres represent Ti and O atoms, respectively.

phase exhibits much higher reactivity in light absorption and photon-to-current conversion, and is the prevalent phase used in experiments.[189–192] Therefore, the anatase phase of TiO$_2$ is usually fabricated for an anode in DSSCs, which assists in separating electrons from photon excitation by dye molecules.

In our calculation, we consider the anatase structure of TiO$_2$ nanowire as a model system, as shown in Fig. 5.2a. This segment exposes four (101) and two (001) facets. Both surfaces are stable, with the former being more favorable, as observed in monocrystals and nanoparticles.[29] The experimental lattice constants of $a = b = 3.784$ Å and $c = 9.515$ Å are employed, which are close to the theoretical values of 3.80 Å and 9.53 Å. In principle, the nanowire unit can be repeated along either the [010] or the [101] direction, forming two nanowire structures of different orientation. The latter structure is similar to that repeated along the [1$\bar{1}$1] direction, with all facets being (101). We studied all these structures, and focused on wires along the [010] and [1$\bar{1}$1] directions, to which we refer according to their axial direction, [010]-wire and [1$\bar{1}$1]-wire. Periodic boundary conditions are used in the directions perpendicular to the wire axis, which separate the nanowire from its images by at

least 10 Å of vacuum. We note that the nanowire structures constructed here are smaller than those used in experiment, whose diameter is typically 30-80 nm (wall thickness∼8-20 nm for nanotubes),[184, 185, 192] as shown in Fig. 5.2b.[192] However, our structures have other features (e.g. 1D geometry, orientation and facets) which are the same as experimental ones and thus represent a reasonable model.
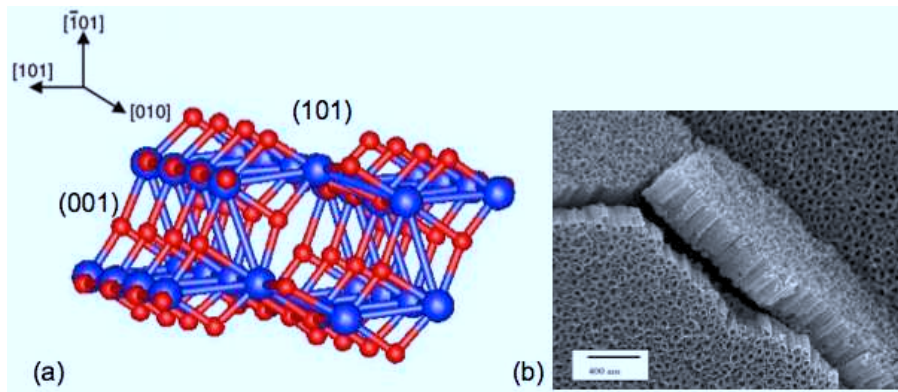

Figure 5.2: Our calculation model for TiO_2 anatase-phase nanowire (a), and lateral view Field Emission Scanning Electron Microscopy (FESEM) images of TiO_2 nanotube (b) from Ref. [192].

5.1.2 Wurtzite/zinc-blende GaAs nanowire heterostructure

Another promising building blocks for nanoscale electronics and optoelectronics is the $p - n$ heterojunction nanowire, such as doped InP nanowire[193] and coaxial silicon nanowires.[43] Their small diameters and unique geometry exhibit the exciting optical and electronic properties which are different from the relevant bulk materials. Furthermore, Integration of lattice-mismatched crystalline structure into a single nanowire presents the possibility in designing and producing relatively cheap devices for solar cell applications.

To this end, two main heterostructures, radial and axial heterostructures,[194, 195] are employed in devices, which increases the functionality of nanowires, and modifies the corresponding properties. The difference between two heterostructure is that the radial heterostructure is formed by the growth of the core/shell nanowires; whereas the axial heterostructure is created by repetition of different composites along the growth axis. Recently, the axial heterostructure, especially for the III-V group materials, such as GaAs, GaP, InP and InAs nanowires,[196, 197] which is composed of a mixture of wurtzite (WZ) and zinc-blende (ZB) segments attracts increasing attention.

Currently, our collaborators have studied the direct correlation between the optical properties and structure at the atomic scale of single GaAs nanowire. They investigate GaAs nanowires either with pure wurtzite or zinc-blende/wurtzite polytypism,[198] by using photoluminescence spectroscopy and transmission electron microscopy (TEM). The corresponding wurtzite/zinc-blende heterostructure of GaAs

nanowire is shown in Fig. 5.3b. In this work, we try to use first-principles calculation based on VASP code with hybrid-exchange functional, (details in chap 2 methodology part) to predict the band offsets for the polytypic zinc-blende/wurtzite nanowire. The unit cells we used for the calculation of both phases are shown in Fig. 5.3a. We
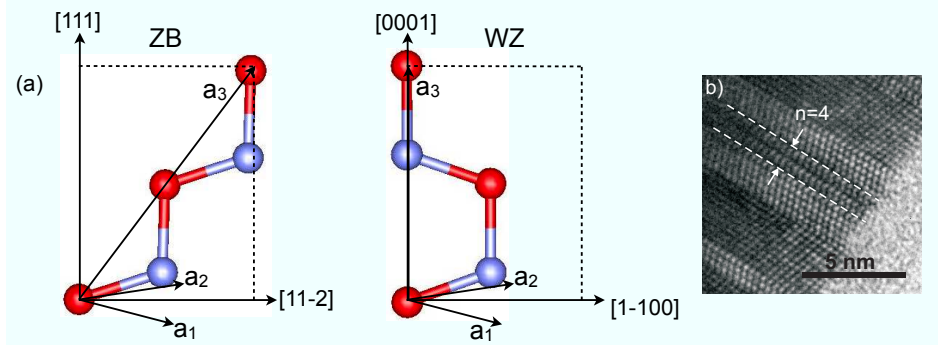

Figure 5.3: (a) Unit cells for zinc-blende and wurtzite phase of GaAs, respectively. Red and light blue spheres represent Ga and As, respectively. (b) HRTEM micrograph of one region of the nanowire from Ref. [198].

use the experimental in-plane lattice constant of 3.99 Å (corresponding to the bulk lattice constant of 5.65 Å) for both ZB and WZ phases, which is very close to the calculated one 3.95 Å.

The corresponding band structures for both phases by using LDA and hybrid functional HSE06 calculations, are shown in Fig. 5.4. The Z direction is responding to the [111] direction for ZB and the[0001] direction for WZ phase, respectively. The hybrid functional calculations obtain the band gap of 1.405 eV for the zinc-blende phase, and 21 meV lower for the wurtzite phase, which are in good agreement with the experimental data.[198] In addition, the relevant band offsets and effective masses match well with experiment, which can be used to understand the electronic properties of heterostructures.

5.2   Natural dyes cyanidin sensitized TiO_2 solar cells

Both TiO_2 and GaAs nanowire are promising candidates in photovoltaic cell devices for assisting electron separations and transport, however, TiO_2 is cheaper and easier to fabricate, which makes TiO_2 more popular in DSSC applications. Therefore, our study focuses on the dye sensitized solar cells based on TiO_2 nanowire, and consider it as a prototype to elucidate the electronic interaction between dye molecule and TiO_2 nanowire.

5.2.1   Configuration and deprotonation process

Configurations. We consider cyanidin (Cya) molecule adsorption on two types of TiO_2 anatase nanowire: one is [010]-wire, as shown in Fig. 5.5, which can be
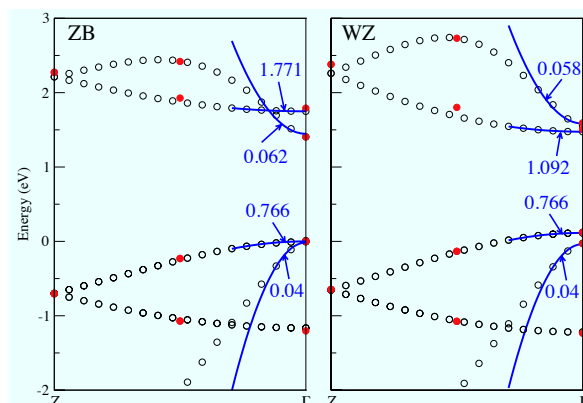
Figure 5.4: The relevant band structures of zinc-blende and wurtzite phase of GaAs along the Z − Γ direction in the Brillouin Zone. Open black circles and red dots represent the LDA results and HSE06 calculation respectively. The effective masses (values in blue) in the units of m_e are obtained from quadratic fits near Γ point (blue curves).

repeated along [010] direction; another is [101]-wire and [1$\bar{1}$1]-wire, which extends along [101] and [1$\bar{1}$1] direction, respectively. Fig. 5.6a presents the structure of the dye sensitized TiO$_2$ [1$\bar{1}$1]-wire with all facets being (101). For the Cya adsorption upon TiO$_2$ [010]-wire, the optimized geometry is that the carbonyl and hydroxyl groups on the ring-*B* adsorb onto neighboring Ti ions of the (101) facet along [010] direction. It is worth pointing out that upon adsorption Cya transfers the H of the hydroxyl group to the nanowire, and is deprotonated. The same is true for the other wire orientations. The [101]-wire and [1$\bar{1}$1]-wire are more stable than the [010]-wire by 0.26 and 0.27 eV per TiO$_2$ unit, respectively.

Deprotonation process and charge injection. For the [010]-wire, Fig. 5.5 shows the deprotonation pathway and the corresponding electronic structures of the initial and final states for the system. Initially, Cya adsorbs intact in the flavylium form, with its OH on ring-*B* pointing to the oxygen atom of the wire forming a hydrogen bond. The OH covalent bond and hydrogen bond lengths are 1.04 Å and 1.51 Å, respectively. The Ti-O bond length formed between the nanowire and the hydroxyl (carbonyl) group is 2.23 Å (1.93 Å). In the transition state, the hydroxyl H atom forms two intermediate bonds with O atoms from Cya and TiO$_2$, the corresponding OH distances being almost identical, 1.31 Å and 1.28 Å, respectively. The total energy increases by 0.23 eV compared to the initial state, indicating a small barrier of 0.23 eV for the H transfer process. After that, the H is completely transferred to the surface O of TiO$_2$ with a bond length of 1.02 Å. The Cya molecule anchors itself on the neighboring O atoms along the [010] direction of the nanowire with Ti-O bond lengths of 1.97 and 1.91 Å, forming the quinonoidal form. The deprotonation process lowers the system energy by 0.27 eV, resulting in a Cya binding energy of 1.0 eV on the TiO$_2$ nanowire with respect to a free Cya molecule and a bare nanowire.

The total density of states (DOS) and that projected on Cya are shown for the dye/wire system before and after deprotonation. Overall, the DOS of the TiO$_2$
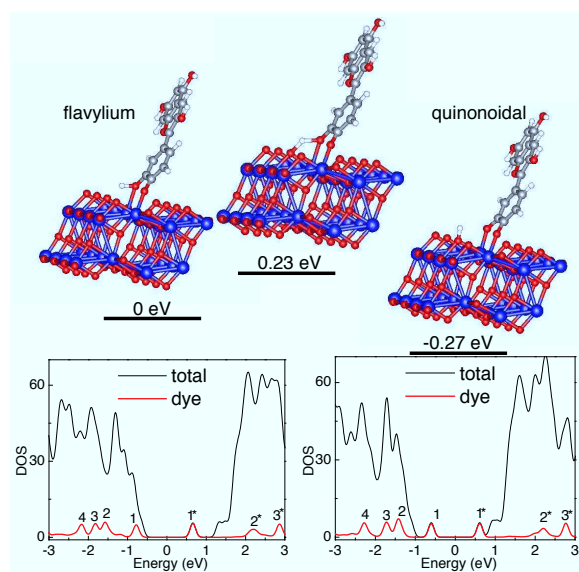
Figure 5.5: Deprotonation pathway and energy profile for a cyanidin adsorbed on the TiO_2 nanowire with the axis along the [010] direction (the [010]-wire). Total DOS (thin black line) and that projected on the dye molecule (thick red line) are shown for structures before and after the deprotonation. States from the dye molecule are numbered as 1, 2, 3 ... for occupied states counting from the HOMO toward lower energies, and 1*, 2*, 3* ... for unoccupied states counting from the LUMO toward higher energies. The Fermi level is set to zero.

nanowire is similar to that for bulk TiO_2. Before deprotonation, the Cya HOMO lies within the valence band (VB) of TiO_2 while the LUMO is far from the conduction band minimum (CBM) of TiO_2 (the latter being higher by 0.7 eV); both are unfavorable for charge injection. After deprotonation, however, the HOMO is shifted into the bandgap region of TiO_2, and the LUMO moves toward the CBM of TiO_2, which is now higher by only 0.3 eV. This is critical for solar cell applications, because in such cases excitation from the dye HOMO to the conduction band of TiO_2 is much easier than from the TiO_2 VB and involves visible light, given the smaller bandgap of isolated cyanidin (2.4 eV) compared to that of anatase TiO_2 (3.2-3.3 eV).[199] Our finding is consistent with the experimental observation[35] that upon Cya adsorption the color of the solution changes from red (flavylium) to purple (quinonoidal), indicating that depronation takes place. Deprotonation of Ru-complex dyes attached to TiO_2 nanoparticles was found to be responsible for the strong dye/TiO_2 coupling recently.[199]

This behavior is quite general for other dye/wire configurations. Deprotonation of Cya results in favorable overlap of the dye orbitals and the TiO_2 bandgap, though the HOMO and LUMO positions may vary from case to case. For example, the LUMO is 0.42 eV lower than the CBM of TiO_2 for Cya attached on the edge of the (101) facet, and 0.48 eV lower for Cya attached on the (001) facet, while the HOMO-LUMO difference is almost constant. These structures are 0.4 and 0.1 eV less stable than that shown in Fig. 5.5. We also studied configurations with the
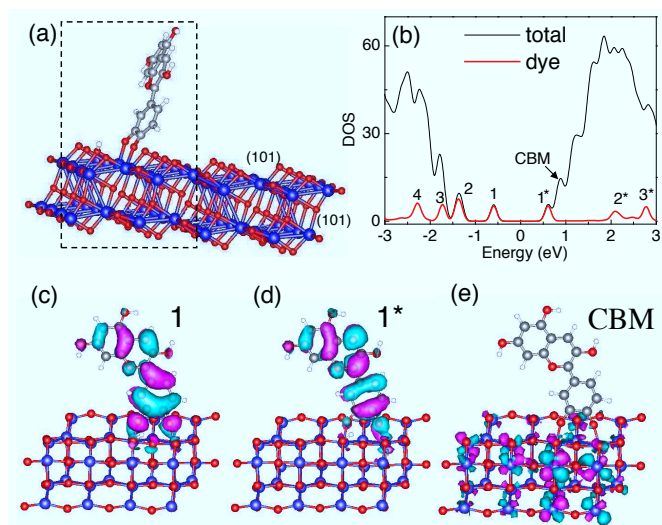
Figure 5.6: (a) Structure of the dye-sensitized TiO$_2$ [1$\bar{1}$1]-wire with all facets being (101). Dashed lines mark the unit cell in the calculation. (b) Total (thin black line) and projected (thick red line) density of states for this system. The corresponding wavefunctions for: the (c) HOMO, (d) LUMO, and (e) LUMO+1 states at the Γ k-point.

proton transferred to different TiO$_2$ sites, which are typically less stable by 0.2 eV .

For the [101]-wire and [1$\bar{1}$1]-wire, the Cya LUMO is 0.27 and 0.20 eV lower than the CBM of TiO$_2$ after deprotonation, respectively, resulting in Cya adsorption energies around 1.5 eV. The latter structure with dye adsorption is shown in Fig. 5.6a. From the corresponding DOS plot, the LUMO of Cya is almost degenerate with the CBM of TiO$_2$ (Fig. 5.6b). The wavefunctions of the states labelled 1 (HOMO), 1* (LUMO) and CBM (LUMO+1) at the Γ k-point are shown in Fig. 5.6c-e. In the HOMO and LUMO states, electrons are mainly localized in the Cya molecule, with a small fraction transferred to Ti ions. The main difference is the bonding and antibonding character between ring-*B* and ring-*C* for the HOMO and LUMO, respectively. In the LUMO+1 state, electrons are delocalized and distributed in the whole nanowire, mainly in Ti d_{xy} orbitals. Detailed analysis of this state reveals that 88% of electrons reside on the Ti orbitals, which is the CBM of the TiO$_2$ nanowire. We conclude from this analysis that an incident photon absorbed by Cya will promote an electron from its HOMO to its LUMO state, then the electron will be injected into the conduction band of the TiO$_2$ nanowire.

Size effect and oxygen vacancy. We have also investigated the dependence of the LUMO$-$CBM energy difference on the size of the nanowire. The [1$\bar{1}$1]-wire of width 2 units, 4 units, and infinity (that is, the 2D (101) surface) have LUMO$-$CBM separation of 0.38, 0.20, and 0.09 eV, respectively. Therefore, we expect that the larger dimensions of the nanowire used in experiment will result in smaller energy separation ($\sim$0.1 eV) between the LUMO and the CBM of TiO$_2$ than what we showed here for small model nanowires. In addition, we have also considered TiO$_2$ nanowire structures with O vacancy defects, which are dominant on TiO$_2$ surfaces. Three different types of O vacancy were analyzed. The first type involves the
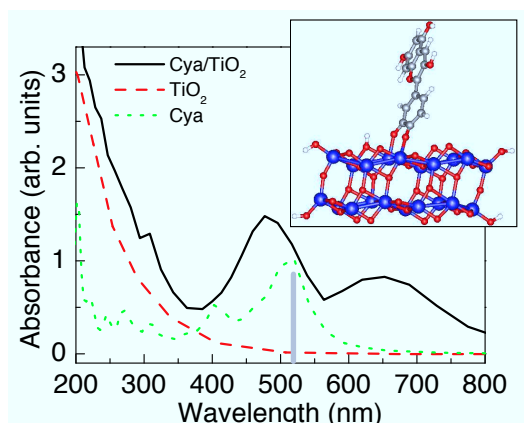
Figure 5.7: Optical absorption spectra of a finite segment of TiO_2 nanowire (inset) with (solid) and without (dashed) sensitizing dye molecules. The calculated spectrum for a free cyanidin molecule is also shown (dotted), together with the experimental peak position (vertical bar).

O vacancy located at one of the four edges of the wire; the second type involves an O vacancy on the surface steps, that is, the outermost oxygen rows, which connect the 5-fold and 6-fold Ti ions of the wire; the third type of O vacancy lies in the flat surface terrace, the oxygen that connects two 5-fold Ti ions. All three types are possible, with the energy difference between them less than 0.1 eV per vacancy. Not surprisingly, the O vacancy right beneath the Cya molecule enhances dye adsorption significantly (adsorption energy 2.7 eV), and results in the LUMO being slightly higher in energy than the CBM of TiO_2, by 0.16 eV.

5.2.2 Optical properties

We calculated the optical properties of the Cya/TiO_2 nanowire using TDDFT. We used a finite segment of the [$1\bar{1}1$]-nanowire with a narrow width (2 repeat units) is terminated by OH or H at the two ends along its axis, resulting in a structure consisting of 20(TiO_2)·2(H_2O), shown in Fig. 5.7 (inset). We checked that this finite structure reproduces well the DOS features of the infinite nanowire. The optical absorption of the dye/wire structure is shown in Fig. 5.7.

For free Cya molecule, it exhibits two major absorption peaks at 520 and 410 nm, respectively. These peaks are prominent and red-shifted to 650 and 480 nm for Cya adsorption on TiO_2 nanowire, with intensity much enhanced due to the interfacial Ti-O coupling between the molecule and the wire. These peaks correspond to excitations from the state 1 (HOMO) and the state 2 (HOMO-1) to the state 1* (LUMO) as labelled in Fig. 5.6b. The red-shift is also consistent with the decreased bandgap of the adsorbed Cya (1.15 eV) compared to that of free Cya (1.45 eV) in DFT calculations. Direct excitation from Cya orbitals to the TiO_2 conduction band is less important, as verified by the negligible transition dipole moment between them. On the other hand, the bare TiO_2 nanowire shows no absorption beyond 400 nm, consistent

50

with its large bandgap $\sim$3.2 eV.[199] Therefore, the dye sensitizer greatly increased the absorption of the TiO$_2$ nanowire in the visible light range, which dominates the terrestrial solar spectrum.

Comparing with experiment, free cyanin solution and cyanin on TiO$_2$ nanoparticles[35] show absorption peaks at 520 nm and 532 nm, respectively, and the latter exhibits two major emission peaks at 550 nm and 740 nm, consistent with our results. In addition, rosella extract with the main component being cyanin shows a strong absorption peak at 560 nm and a shoulder at 650 nm after adsorption on TiO$_2$ nanoparticles,[200] which agrees well with our calculated spectrum. The differences may be assigned to the versatility of dye adsorption configurations and different TiO$_2$ structures (nanowires in the calculation versus nanoparticles in experiment).

5.2.3   Rapid charge injection

In order to make solar cells efficient, rapid charge injection and transport are required in addition to intense visible light absorption. Many previous studies have emphasized that the dye LUMO being higher than the CBM of TiO$_2$ is beneficial for efficient electron injection.[201–203] However, this causes other problems for DSSCs, namely, the electrons excited to the dye LUMO can dissipate through non-radiative processes into the lower-lying CBM of TiO$_2$, reducing significantly the open circuit potential V_{oc} and causing unwanted energy loss.[201, 204] The ideal case would be that the LUMO is close to and slightly higher than the CBM to produce both large V_{oc} and high injection rates, ultimately leading to large I_{ph} accompanied by intense light absorption. For our system of natural-dye sensitized TiO$_2$ nanowire, large V_{oc} would not be a limitation because of the large difference between the HOMO and CBM. We demonstrate below that this structure also facilitates ultrafast electron injection from the dye LUMO to the CBM of the TiO$_2$ wire, a result coming from their close match in energy, despite the fact that the LUMO is slightly lower.

Electronic injection process. We monitor the electron injection process from Cya to the TiO$_2$ nanowire after photon absorption using TDDFT. Fig. 5.8a shows the evolution of electronic energy levels with respect to simulation time. At time t=0, one electron is promoted from the HOMO to the LUMO of Cya, which is a good approximation for representing the first excited state.[157] We then let the coupled electron-ion system evolve in real time. The initial ionic temperature is set to 350 K. The energy of the LUMO, occupied with one electron after excitation, first approaches that of the CBM of TiO$_2$, and later diverges from it. There is a crossover at time 30 fs, after which the two states seem mixed, evidenced by the large off-diagonal Hamiltonian matrix element. The density distribution of the excited electron is also monitored, and projected onto all Ti and O atomic orbitals in the nanowire. The latter is considered as the "injected" electrons into the nanowire.

We found that at $t = 0$ only 0.14 e is distributed on the TiO$_2$, due to the electronic coupling between Cya and the wire through carbonyl groups. This value decreases slightly then starts to increase after 5 fs (Fig. 5.8b), and reaches a first maximum of 0.2 e at $t = 18$ fs and a second maximum of 0.4 e at $t = 48$ fs. The value increases

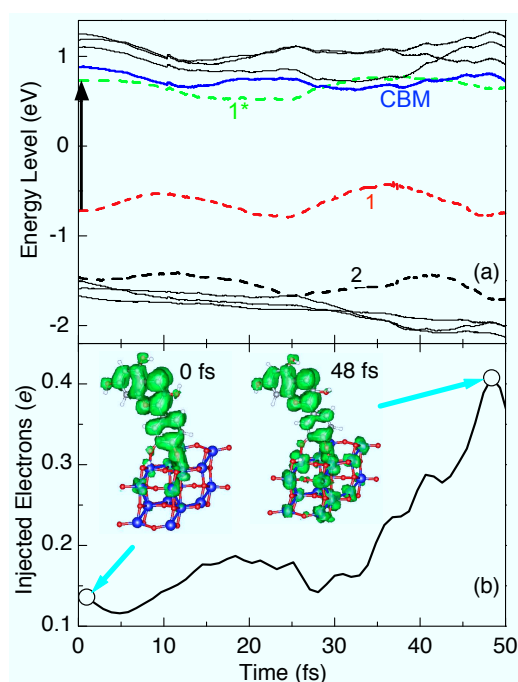**Figure 5.8:** (a) Evolution of electronic state energy levels after excitation of cyanidin from its HOMO (state 1) to the LUMO (state 1*). Energy levels contributed by the dye are shown in dotted lines. (b) Fraction of electrons injected to the TiO_2 nanowire as a function of time after excitation. The insets show the charge density of the excited electron at $t = 0$ and 48 fs at the contour level of 0.004 e/Å^3.

further to 0.6 e around $t = 63$ fs (not shown). This ultrafast charge injection is more obvious if we compare the density distribution of the excited electron at $t = 0$ and 48 fs in Fig. 5.8b. On the other hand, direct recombination of the electron and the hole is unfavorable because the off-diagonal matrix element between them is <0.04 eV, much smaller than their large energy separation of 1.40 eV, which gives zero Landau-Zener probabilities, indicating that the lifetime of the excited state is long. The details are discussed in paper.[205]

Experimental measurements[35] have revealed ultrafast electron injection from cyanin to TiO$_2$ nanoparticles within less than 100 fs, and a recombination lifetime of 67 ps, in good agreement with our result. Later experimental[206, 207] and theoretical studies[202, 208] confirmed even faster injection processes, within 10 fs or less, take place from other organic dyes (alizarin, bi-isonicotinic acid, catechol) to TiO$_2$.

Injection pathways. We further analyzed the pathways of the injected electron and its transport inside the nanowire. Fig. 5.9 shows the fraction of electrons projected on each Ti ion of the nanowire during charge injection. Ti ions are numbered explicitly in the unit cell in four directions from top (where Cya sits) to bottom. Not surprisingly, the electron is mainly distributed on Ti1, which is bonded to the carbonyl group on the B-ring of Cya, and Ti9, where the deprotonated hydroxyl group binds. From Fig. 5.9a, we find that electrons proceed along Ti1→Ti2→Ti3→Ti4 during charge injection, resulting in density maxima in Ti4 at $t = 16$ fs and 52 fs. Other pathways following the same direction show approximately the same trend. This indicates that electrons first flow in and fill the whole nanowire. Parallel charge transport along the nanowire axis, such as, Ti1→Ti6→Ti5→Ti2′ (Ti2′ being the image of Ti2 in the next cell) is less favorable, judging by the small density and the later appearance of electrons in this path. Efficient charge transport could take place along the Ti13→Ti14→Ti9→Ti10 direction at a later time. Interestingly, previous quantum dynamics simulations with a model Hamiltonian have shown[202] that charge injection along the [101] direction is an order of magnitude slower than that along [$\bar{1}$01] for electrons excited to the HOMO of catechol on TiO$_2$, consistent with our results (note that the direction indices are reversed in Ref. [202]). Therefore, we have demonstrated from first-principles that both charge injection and charge transport occur effectively at the ultrafast timescale in the natural-dye sensitized TiO$_2$ nanowire, even though in this system the dye LUMO is slightly lower than the CBM of the semiconductor, mainly due to the influence of ionic thermal motions in the dye/nanowire system. As a result, both a large V_{oc} and a high electron injection rate can be achieved, which would result in a high efficiency of the natural-dye sensitized TiO$_2$ nanowire solar cells.
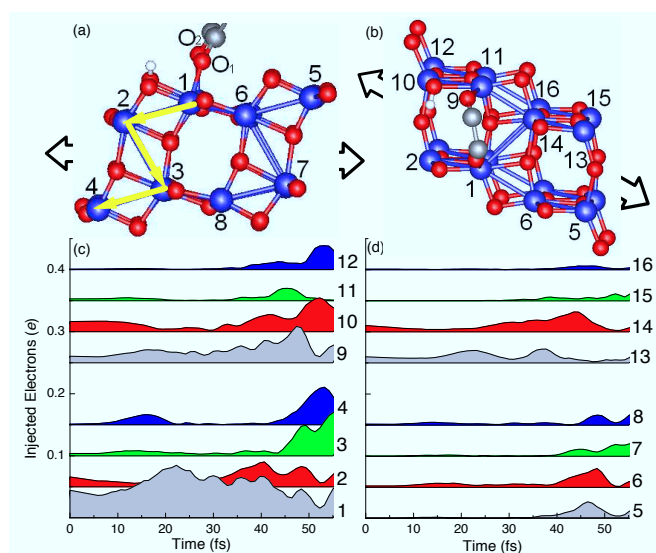
Figure 5.9: Electron transport pathways inside the nanowire. Ti ions are numbered explicitly in (a) the side view and (b) the top view. Only the bottom part of the adsorbed cyanidin (O-C-C-O) is shown. Arrows show the direction of the nanowire axis. (c)-(d) The injected electron distribution on each Ti in the nanowire unitcell as a function of simulation time. For better view, lines are shifted vertically by 0.05 for consecutive curves.

Electronic interactions between copper (fluoro-)phthalocyanine and epitaxial graphene

The interaction between metal phthalocyanines (MPcs) and solid surfaces plays a crucial role in determining the performance of organic solar cells. Their energy conversion efficiency depends sensitively on the interface structure and electronic coupling between molecules and the electrode surface and between organic molecule layers. Much current research has focused on understanding and controlling the epitaxial growth of MPcs on metal surfaces,[209–211] highly oriented pyrolytic graphite (HOPG),[212–214] and SiO$_2$ substrate[215] by using scanning tunneling microscopy (STM) and atomic force microscopy (AFM). Some are dedicated in studying the band alignment and charge transfer from the experimental point view. However, the mechanism of the electronic interaction at the interface is still unknown.

In this chapter, we choose two typical MPc molecules, copper phthalocyanine (CuPc) and hexadecafluorophthalocyanine (F$_{16}$CuPc), because they are air, chemically and thermally stable, and absorb intensively red light. The self assembly process of these two types of molecules on epitaxial graphene (EG) have been investigated, and we explore the corresponding electronic and optical properties by using first-principles calculations based on density functional theory (DFT) and time-dependent DFT (TDDFT). Moreover, we elucidate the mechanism of the electronic interaction between MPcs and EG, the simplest model, which is useful to understand and predict the charge transfer at the organic/inorganic interface in molecular electronic devices and solar cells.

6.1 Models and computational details

The structure of CuPc and F_{16}CuPc molecule is shown in Fig. 6.1, as the model systems to study the electronic interaction between MPc molecule and EG. First-principle calculations are performed with the SIESTA code employed[160] and the Vienna *ab initio* simulation propgram (VASP),[216] in the framework of density functional theory. Since van der Waals (vdW) forces are important for such weakly interaction systems, we also use vdW-density functional (vdW-DFT) of the Lunqvist-Langreth type for typical bonding configurations,[113] which would provide qualitatively correct energy difference and trend for the electronic coupling. The Heyd-Scuseria-Ernzerhof (HSE) hybrid functional[112, 217] is also used in the isolated molecule simulation. An auxiliary real space grid equivalent to a plane-wave cutoff of 120 Ry is employed in the calculation and the spin polarization is also considered. Single Γ point is used to optimize the structure, and the k-point mesh of $(8 \times 8 \times 1)$ in the Monkhorst-Pack sampling scheme are used to analyze the relevant electronic properties for the unit cell (UC) of Pc/graphene system. The basis-set superposition error (BSSE) is excluded in the adsorption energies. Other computational details are the same as chap 4.

For the uniform F_{16}CuPc overlayers $(\alpha - \alpha)$, we consider two possible supercells: supercell lattice vectors run along the armchair direction of graphene (denoted as gra[(3,4)×(4,3)]) (Fig. 6.4b), and along its zigzag direction (gra[(6,0)×(6,1)]) (Fig. 6.4a), respectively. Both lattice vectors for gra[(3,4)×(4,3)] have a length of 14.96 Å with an angle of 69° in between. For the CuPc/graphene system, we adopted a square-like lattice, $(1, 5) \times (4, 3)$ with lattice vectors of 13.69 Å and 14.96 Å, and an angle of 86°. For non-uniform F_{16}CuPc stripes, a $(3, 4) \times (8, 6)$ unit cell is used to to simulate the layer of coexisting α and β stripes. It is noted that there are two F_{16}CuPc molecules in a unit cell.

6.2 Isolated phthalocyanine

6.2.1 Molecular structure

Both CuPc and F_{16}CuPc (see Fig. 6.1) are the planar structures, exhibiting a four-fold symmetry (D_{4h}). The only difference of the two MPc molecules is that all H atoms in phenyl group of CuPc are substituted by F atoms to form F_{16}CuPc.

The optimized structural parameters we calculated and the experimental measurement for both molecules are collected in Table 6.1. From the table, it is obvious that our calculation results of the structural parameters of CuPc are in good agreement with experimental value from Ref. [218]. It approves the reliability of our structure calculations. In comparison with CuPc, F_{16}CuPc shows the similar averaged bond length for the Cu-N, C-N and C-C bond and a 90° of the N1-Cu-N3 angle. However, the diagonal distance between two outermost F atoms (F1-F1′) in F_{16}CuPc is 15.47 Å, 0.43 Å longer than the relevant H1-H1′ bonds of CuPc (15.04 Å), because of 0.2 Å longer for C-F bonds than that for C-H bonds (see Table 6.1).
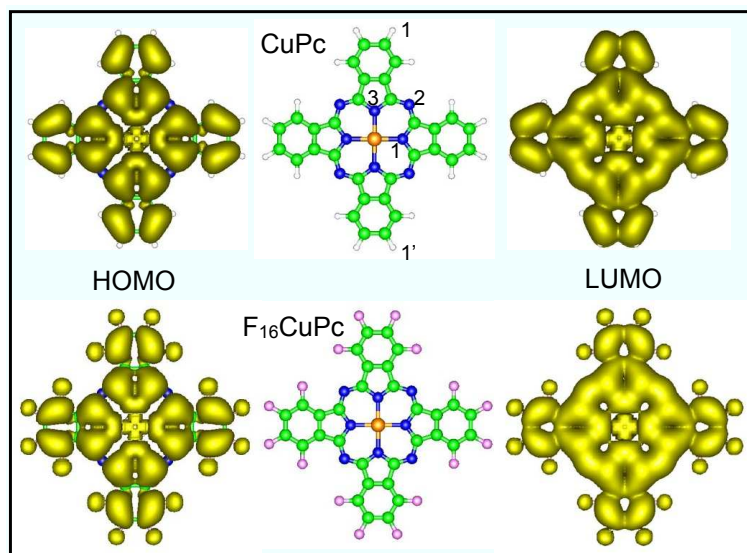
Figure 6.1: Atomic structures of the isolated CuPc (top panel) and F_{16}CuPc (bottom panel) molecules, and the corresponding charge density contour at $0.001e/\text{Å}^3$ for the HOMO and LUMO states. C, H, F, N, Cu atoms are denoted as green, white, pink, blue and orange spheres, respectively.

Table 6.1: Calculated structural geometry for CuPc and F_{16}CuPc molecules with the experimental values of CuPc molecule (Ref. [218]) for comparison. The bond length shown in this table are the averaged bond length of two molecules in the unit of Å. The unit of the bond angle is $^\circ$. Atoms are marked in Fig. 6.1.

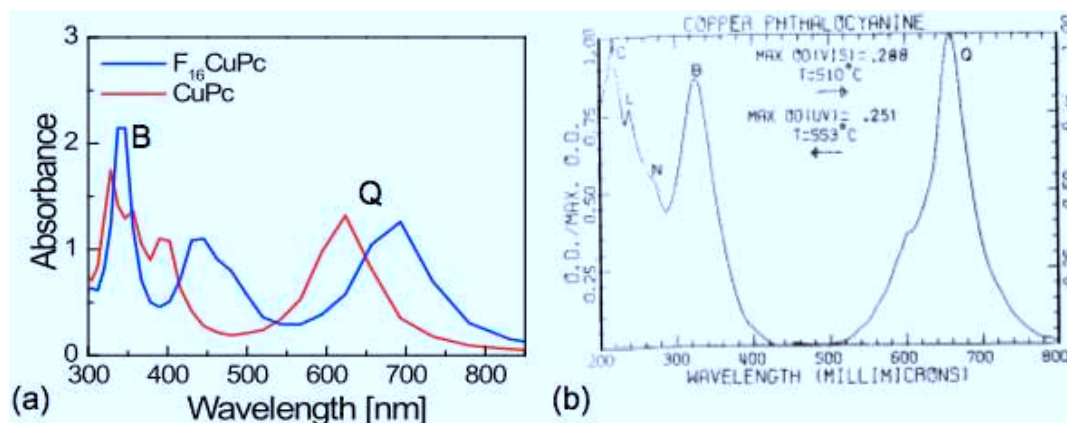|	CuPc	Expt.	F_{16}CuPc
$R_{\text{Cu}-\text{N1}}$	1.944	1.935	1.946
$R_{\text{C}-\text{N1}}$	1.378	1.366	1.376
$R_{\text{C}-\text{N2}}$	1.324	1.328	1.322
$R_{\text{C}-\text{N}}$	1.351	1.347	1.349
$R_{\text{C}-\text{C(Benzene)}}$	1.406	1.391	1.408
$R_{\text{C}-\text{C(Pyrrole)}}$	1.459	1.453	1.459
$R_{\text{C}-\text{H(/F)}}$	1.113	-	1.328
$\theta_{\text{N1}-\text{Cu}-\text{N3}}$	89.9	88.7	89.8
$\theta_{\text{C}-\text{N1}-\text{C}}$	108.3	107.3	108.4

Figure 6.2: (a) UV-vis spectra of CuPc and F_{16}CuPc calculated from TDDFT and (b) experimental spectrum for CuPc from Ref. [58].

6.2.2 Electronic and optical properties

From Fig. 6.1, it is clear that the highest occupied molecular orbitals (HOMO) and lowest unoccupied molecular orbitals (LUMO) for CuPc and F_{16}CuPc molecules are similar, except for small amount of electrons distributed on all F atoms of F_{16}CuPc molecule, due to large electron affinity of F atoms. It is worth pointing out that the LUMO of F_{16}CuPc is brighter at the central Cu position than that in HOMO; CuPc, however, does not show obvious contrast, which is in consistent with experimental STM images.[212]

We also compare the relevant absorbance spectra for both molecules as shown in Fig. 6.2 by using TDDFT. Both Pc molecules exhibit two major absorption peaks (Q- and B-band) in the visible light region. For CuPc, the Q-band locates at 624 nm and B-band at 328 nm with a shoulder at 594 nm, which is in good agreement with the experimental UV-vis spectra 657 nm for the Q-band and 325 nm for the B-band, with a shoulder at 600 nm.[58] In addition, our results show small absorption peaks at 399 nm and 356 nm, which are missing in experiment because of the resolution limit in the experiment. For F_{16}CuPc, three absorption peaks lie in 693 nm, 446 nm and 346 nm, respectively. The red-shift of 0.2 eV of Q-band is consistent with the band-gap narrowing observed in optical measurements of CuPc (1.7 eV) and F_{16}CuPc (1.5 eV).[74] And a red-shift of 0.23 eV is also observed in CuPc and F_{16}CuPc thin-films despite the presence of intermolecular interactions.[219]

To elucidate the nature of the absorption bands, we analyze the electronic structure of both Pc molecules. The density of state (DOS) and the wavefunctions of the HOMO and LUMO for F_{16}CuPc by using HSE functional are presented in Fig. 6.3a. The HOMO states are composed of two degenerated a_{1u} orbitals; while the LUMO states comprise four degenerated e_g orbitals, and one $b_{1g\downarrow}$ orbital. Therefore, the HOMOs behave mainly π bonding character, whereas in the LUMOs the antibonding combination dominates.

In comparison with calculated results of CuPc,[220] as depicted in Fig. 6.3b, the same orbitals for the corresponding HOMO and LUMO are obtained. The discrep-

ancy between LDA and HSE results lies in the inaccurate description of localized states (b_{1g}) in LDA, which contains a large self-interaction error for such states. Therefore, the Q-bands for both molecules are attributed to electronic excitations from the HOMO to LUMO states of molecules, suggesting the $\pi \rightarrow \pi^{\star}$ character. Furthermore, the electronic band gap of $F_{16}CuPc$ is around 0.2 eV smaller than that of CuPc, which accounts for the red-shift in UV-vis spectra discussed above.

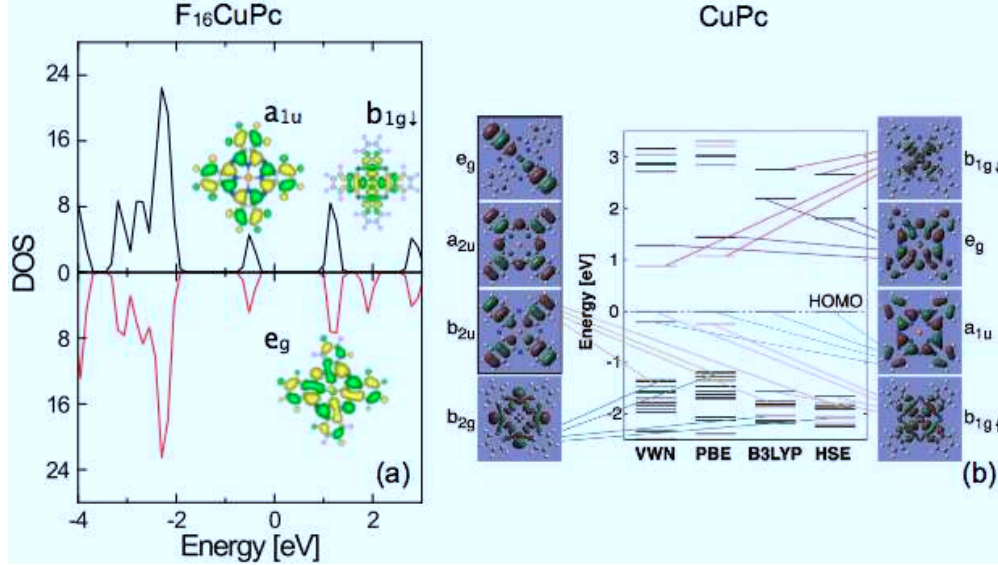**Figure 6.3:** Density of states (DOS) and selected molecular orbitals of the $F_{16}CuPc$ molecule (a) and energy alignment for CuPc[220] (b) by using HSE functional. Up (black curves) and down (red curves) panels show the spin-up and spin-down component, respectively.

6.3 Uniform phthalocyanine overlayers

6.3.1 Configuartion of the $F_{16}CuPc$/graphene system

As defined in the above section, two possible supercells of gra[(3,4)×(4,3)] and gra[(6,0)×(6,1)] are employed to simulate the uniform $\alpha - \alpha$ $F_{16}CuPc$ overlayer adsorption upon graphene, as shown in Fig. 6.4a-b respectively. To match the lattice vectors of 15.1 Å×16.0 Å and the molecular arrangement along the armchair direction of graphene measured in STM image,[221] we focus on $F_{16}CuPc$ molecules adsorption upon gra[(3,4)×(4,3)].

In order to find the optimized structure, we vary the adsorption height and the orientation of $F_{16}CuPc$ with respect to the underlying graphene lattice. Our results in Fig. 6.5 show that the energy minimum is obtained when $F_{16}CuPc$ molecule is located 3.08 Å above the EG surface and the azimuthal angle is $-9°$, defined as the angle between molecule diagonal and the short diagonal direction of the UC, (see Fig. 6.4b). Similarly, the optimized geometry in gra[(6,0)×(6,1)] supercell has an adsorption height of 3.05 Å and the azimuthal angle of $-19°$. Upon adsorption, the

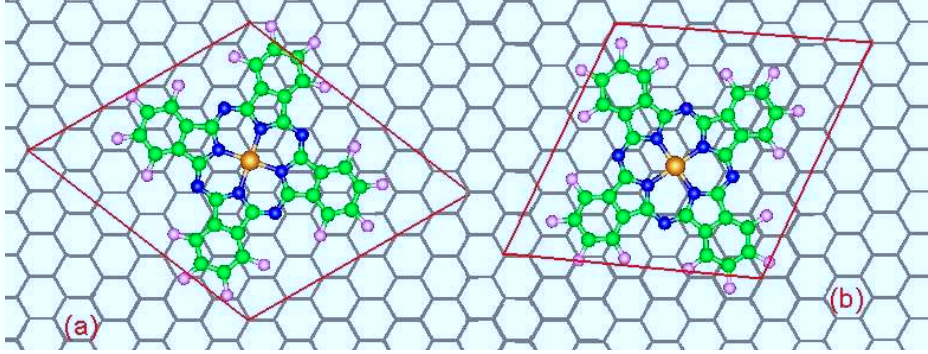**Figure 6.4:** Configurations of F_{16}CuPc molecule adsorption on the gra[(6,0)×(6,1)] (a), and gra[(3,4)×(4,3)] surface (b). The unit cell is described in red parallelogram, C atoms of Pc are changed to green for distinguishing from graphene.

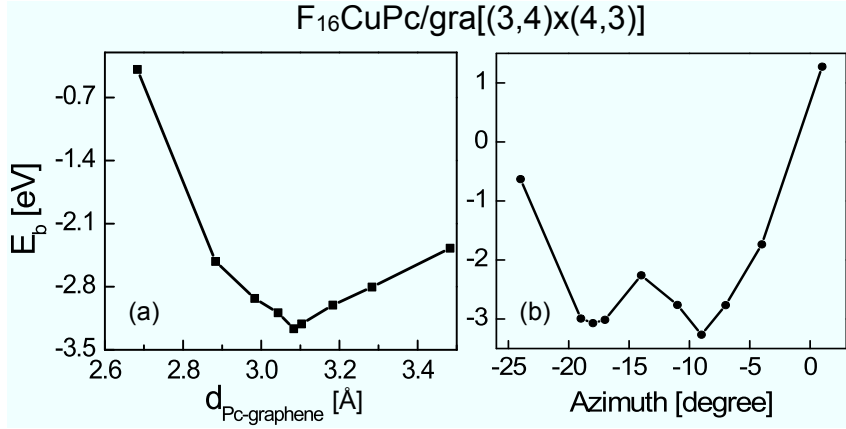**Figure 6.5:** The adsorption energy for F_{16}CuPc molecule adsorption upon gra[(3,4)×(4,3)] as a function of the distance between Pc molecule and graphene surface (a), and the azimuth of molecule (b).

molecule deviates from the ideal planar structure, with the N atoms around Cu being 0.04 Å higher and the periphery F atoms 0.10 Å lower than Cu. In addition, the molecular size shrinks by 0.13 Å in diagonal directions. The corresponding adsorption energy E_a is −3.19 eV and −3.17 eV in gra[(3,4)×(4,3)] and gra[(6,0)×(6,1)] supercells, respectively, using vdW-DF functionals at adsorption height of ∼3.4 Å. The adsorption energy is defined as:

$$E_a = (E_{tot} - E_{gra} - n \times E_{Pc})/n \tag{6.1}$$

where E_{tot}, E_{gra}, and E_{Pc} is the total energy of the adsorption system, the energy of the isolated graphene substrate, and the energy of gas-phase Pc molecule, respectively. n is the number of Pc molecules in the unit cell.

Based on the optimized configuration (Fig. 6.6a), we also calculate the contour plot of potential energy surface in Fig. 6.6b. The dark blue region at (1.42, 0) Å and (0.71, 1.23) Å are both close to the top site of a carbon atom in graphene, shows the highest binding energy of 3.19 eV, indicating the stability of the atop site for
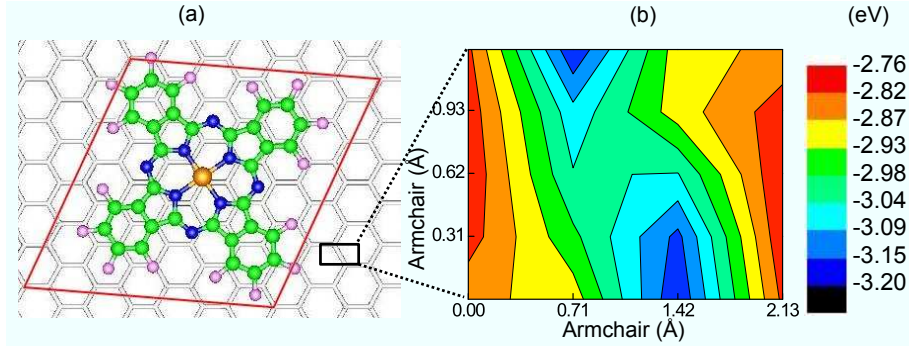
Figure 6.6: (a) The optimized configuration and (b) potential energy surface contours for the $F_{16}CuPc/gra[(3,4)\times(4,3)]$ system. Graphene is shown as a gray sheet to distinguish it from C atoms in the Pc molecule. The unit cell is described by a red parallelogram. The potential energy surface is calculated by using a (4×5) grid sampling in the rectangular region marked in the lower right corner of (a).

$F_{16}CuPc$ adsorption on EG. Moreover, between these two stable sites, Fig. 6.6b reveals a smooth diffusion pathway with a very small barrier ~ 0.16 eV for $F_{16}CuPc$ adsorption on EG. Hence the molecule could diffuse freely on EG to find its most stable adsorption sites.

6.3.2 Band offset

For the adsorption system, the corresponding total DOS (thick black solid line), as well as that projected on to Pc molecule (black dash-dot line) and the graphene substrate (red solid line) are presented in Fig. 6.7a. The two features below and above E_f in the total DOS mainly come from the contributions of the HOMO and LUMO of $F_{16}CuPc$ molecules, which are composed of two spin-up and a spin-down orbital (for HOMOs), and two spin-up and three spin-down orbitals (for LUMOs), respectively. The HOMO and LUMO states are 0.93 eV and 0.37 eV below and above E_F, respectively, rendering a band gap of 1.30 eV. The value of the band gap is smaller than that measured result for $F_{16}CuPc$ molecules deposited on monolayer graphene (MEG), 1.44 eV,[221] as depicted in Fig. 6.7b and HSE result (1.7 eV). It is well known that the band-gap underestimation is typical in LDA. For the Pc molecules adsorption on bilayer EG (BEG) (see Fig. 6.7b), the band gap is even wider.[221]

More importantly, the LUMO states of Pc are slightly occupied, indicating a small amount of electron transfer from graphene to $F_{16}CuPc$. This is also consistent with the fact that E_F is 40 meV lower than the Dirac point of EG. Furthermore, the projected DOS (PDOS) of EG shows two small features at 0.65 eV (0.39 eV) below (above) the E_D, and a major smoothing effect for the peak in the range 2–3 eV below E_D. This suggests that the electronic states of graphene are redistributed upon $F_{16}CuPc$ adsorption.
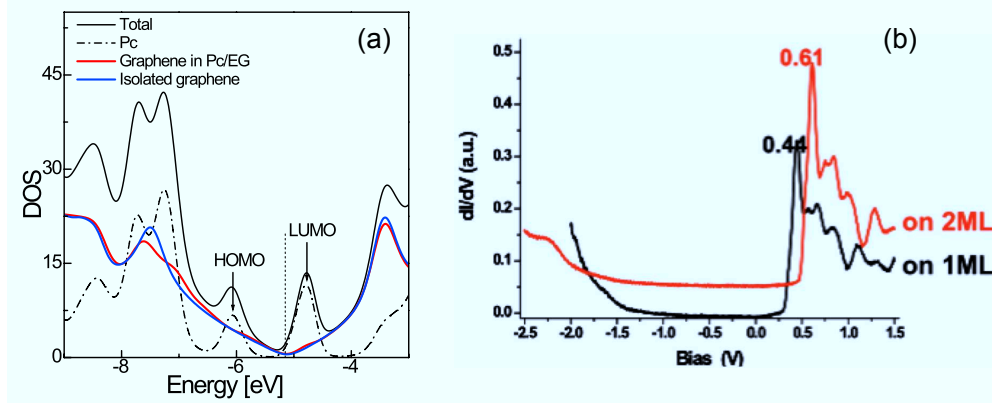
Figure 6.7: (a) Total DOS (thick black solid line) and projected DOS on the Pc molecule (black dash-dot line), on graphene (red solid line), upon F_{16}CuPc adsorption on graphene, and the DOS of the isolated graphene (blue solid line). The vertical dotted line shows the Fermi level. (b) Scanning tunneling spectroscopy (STS) performed on F_{16}CuPc molecule adsorption on monolayer (lower) and bilayer (upper) EG, respectively.

6.3.3 Charge transfer

To gain more insights of the electronic interaction between F_{16}CuPc and graphene, we show in Fig. 6.8 the bonding character and charge redistribution upon F_{16}CuPc adsorption by calculating the corresponding charge density differences (CDD), defined as,

$$\Delta\rho = \rho_{Pc/gra} - \rho_{Pc} - \rho_{gra} \tag{6.2}$$

where $\rho_{Pc/gra}$, ρ_{Pc}, ρ_{gra} are the charge density of the combined system, isolated Pc molecule and graphene with geometry fixed at optimized ones in Pc/EG. From Fig. 6.8c, it is clear that p_z orbitals of Pc molecule and EG are mainly involved forming a strong $\pi - \pi$ interaction, and form an interfacial electronic layer between Pc and EG, yielding a dipole layer pointing towards Pc molecule. More explanations are listed in the paper.[222] Integrating the CDD along surface normal directions z suggests a net $0.08e$ transferred from EG to F_{16}CuPc for the neutral system, as shown in Fig. 6.8d. To simulate the substrate charging effect of SiC,[221] we charged the whole system by $0.4e$ and $0.8e$ respectively, to model the realistic electronic conditions of BEG and MEG. We find that charged system facilitates more charge transfer to Pc molecule from charged EG surface. To quantitate the charge transfer by using the same analysis in Fig. 6.8d, a net charge of $0.32e$ ($0.51e$) transfers to F_{16}CuPc from BEG (MEG).

6.3.4 Comparison with CuPc/EG system

Atomic structure. First, we compare the atomic structure of the CuPc/EG system (Fig. 6.9a) with the F_{16}CuPc/EG system (Fig. 6.6a). The most stable adsorption site for Pc in both systems is the top site of C atoms of EG. The structure, however, varies in several aspects: 1) adsorbed CuPc overlayer arranged in the
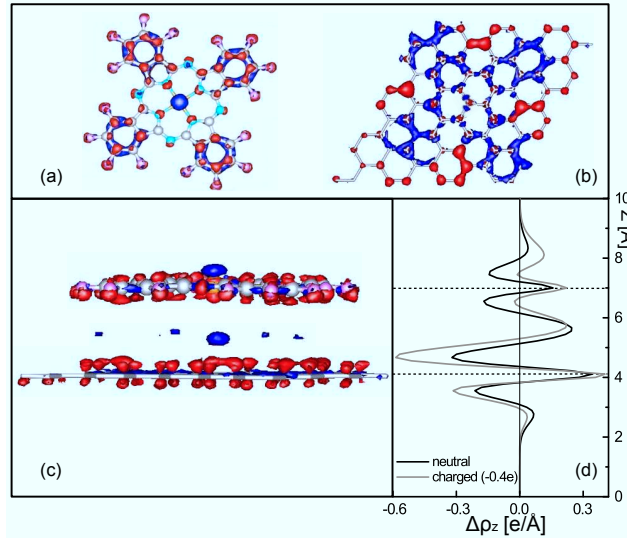
Figure 6.8: Top view (a, b) and side view (c) of the charge density difference (CDD) for the $F_{16}CuPc/gra[(3,4)\times(4,3)]$ at contour levels of $0.003e/\text{Å}^3$. The blue and red clouds correspond to regions with electron accumulation and depletion, respectively. To differentiate from electron clouds, N atoms are denoted in light-blue. (d) The plane-averaged CDD along the surface normal direction of graphene for neutral system (black line) and charged system with $-0.4e$ (gray line). Horizontal dash lines indicate the positions of graphene and the $F_{16}CuPc$ molecule.

square-like lattice,[214, 223] while $F_{16}CuPc$ overlayer in hexagonal lattice;[212, 221] 2) On graphene CuPc overlayer is more compact than that of $F_{16}CuPc$ because of the smaller molecule size (diagonal H-H distance of 15.04 Å for CuPc vs. diagonal F-F distance of 15.47 Å for $F_{16}CuPc$) and weaker H-H repulsion than F-F repulsion between neighboring molecules; 3) the adsorption height of CuPc is 3.15 Å, 0.1 Å higher than that of $F_{16}CuPc$ in LDA, and the adsorption energy is -2.47 eV in vdW-DF (height$\sim$3.4 Å), which is 0.72 eV lower than that of $F_{16}CuPc/gra[(3,4)\times(4,3)]$. The smaller absorption energy of CuPc than $F_{16}CuPc$ is attributed to weaker vdW interaction between CuPc and graphene and between CuPc molecules, due to the smaller charge density around periphery H atoms than F atoms in $F_{16}CuPc$, and 0.07 Å larger distance between CuPc and graphene.

DOS and STM image. Fig. 6.9b represents the corresponding DOS for both systems. The DOS features of CuPc/graphene are qualitatively close to that of $F_{16}CuPc$/graphene, whereas the biggest difference is the band level alignment: with reference to the Dirac point of graphene E_D, the HOMO of CuPC is 0.76 eV below E_D while the HOMO of $F_{16}CuPc$ is 0.94 eV below E_D, and the LUMO is 0.56 eV and 0.34 eV higher than E_D for CuPc and $F_{16}CuPc$, respectively. Since the LUMO of $F_{16}CuPc$ is closer to the Fermi level and could facilitate easier charge transfer from graphene to the molecule, consistent with its n-type nature. On the other hand, LUMO of CuPc is higher and more difficult to accept electrons from the substrate, re-assuring its p-type character. Our result is in good agreement with pho-
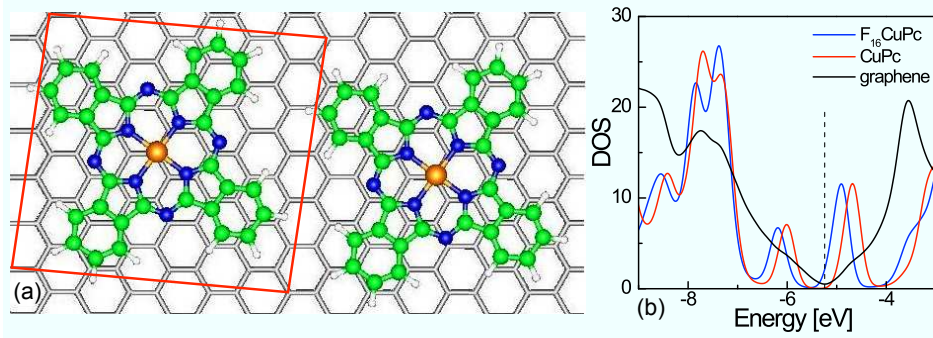
Figure 6.9: (a) Geometry of CuPc molecules adsorbed on graphene[$(1,5)\times(4,3)$] surface. (b) The corresponding DOS projected on CuPc and graphene for the adsorption system, respectively. The dashed line marks the Dirac point which is 10 meV below the Fermi level for CuPc/graphene.
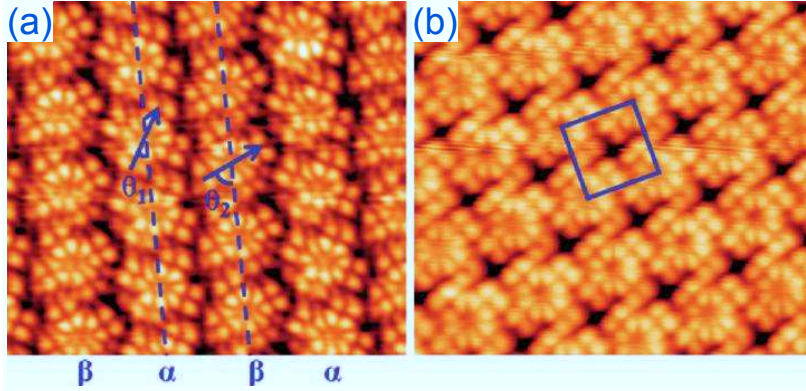
Figure 6.10: STM images for the HOMO of F_{16}CuPc monolayer(a) and CuPc monolayer (b) on HOPG from Ref. [223].

toelectronic measurement of HOMO position on highly oriented pyrolytic graphite (HOPG):[213] it is 0.9 eV and 1.2 eV below the E_F of HOPG for CuPc and F_{16}CuPc, respectively.

The fact that HOMO of CuPc is closer to Fermi level than F_{16}CuPc is also consistent with experimental observation of brighter CuPc images (HOMO) under the positive tip bias ($+2.0\ V$), as shown in Fig. 6.10, indicating that more electrons in occupied sates of CuPc tunnel to the Fermi level of the tip.[223] Similarly, F_{16}CuPc images (LUMO) are brighter than CuPc under the negative bias -2.0 V,[212] suggesting more electrons collected in this energy range.

Charge transfer. The redistribution of electron density upon CuPc adsorption is also similar to the case of F_{16}CuPc. However, F_{16}CuPc shows much higher electron polarization at the interface, displayed by the higher positive peak between Pc and graphene planes and the lower negative peaks in the molecule region (Fig. 6.11a). A significant difference from F_{16}CuPc in Fig. 6.8 is that the charge redistribution on CuPc is very small, whereas more electrons are located around the benzene-like rings and F atoms in F_{16}CuPc case.

Figure 6.11: (a) The plane-averaged CDD along the surface normal direction of graphene for both systems. Dot lines mark the pos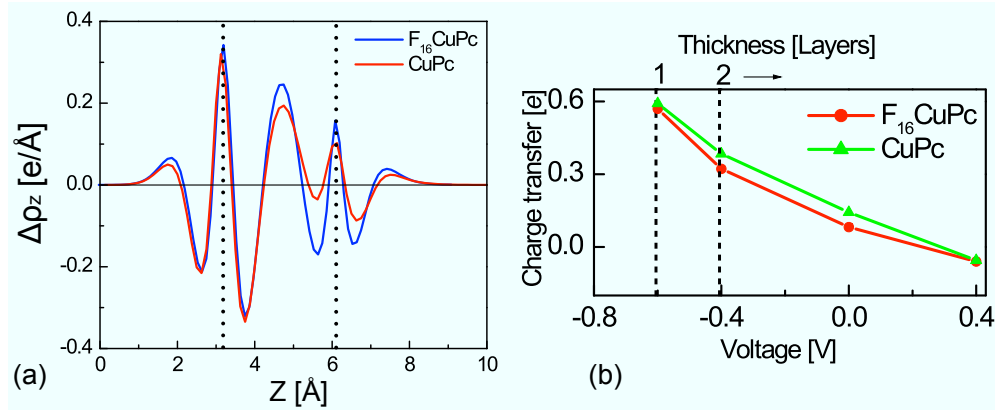itions of graphene and molecule plane. (b)The amount of electron transfer from graphene to the adsorbed Pc molecule as a function of voltage applied in the system and thickness of graphene layers. The red line with dots shows the charge gained by F$_{16}$CuPc, and the green one with triangles represents the CuPc case.

The amount of electron transfer from CuPc to graphene also follows the same trend as that of F$_{16}$CuPc with the increase of graphene voltage or the decrease of EG thickness, as also plotted in Fig. 6.11b. CuPc could gain $0.59e$ and $0.38e$ on MEG and BEG, respectively. The larger polarization effect at the F$_{16}$CuPc/graphen interface is consistent with the stronger electron-accepting properties of the F$_{16}$CuPc molecules. As a result, the induced interface dipole for F$_{16}$CuPc is greater than that for CuPc, blocking electron transfer from F$_{16}$CuPc to graphene in the former when graphene is used as transparent anodic electrode in photovoltaic devices.[88]

6.4 Non-unifrom F$_{16}$CuPc stripes

For the non-uniform F$_{16}$CuPc stripes arranged on EG surface, forming the alternate $\alpha - \beta$ orientation. The three optimized configurations are shown in Fig. 6.12b-d. The relevant lattice vectors are 14.96 Å and 29.92 Å, at an angle of 69.4° for the F$_{16}$CuPc/gra[(3,4)×(8,6)] system.

The adsorption energy is -6.16 eV/UC for the $\alpha - \alpha$ orientation in Fig. 6.12a. The $\alpha - \beta$ arrangements have very close energetics with an adsorption energy around -5.99 ± 0.03 eV/UC for Fig. 6.12c-d. The difference is within the computational limit of accuracy, however, we find the molecular orientation in Fig. 6.12c is closest to the arrangement observed in experiment (Fig. 6.13a). The small difference in the adsorption energy of -0.1 eV/Pc indicates that Pc molecules in $\alpha - \alpha$ and $\alpha - \beta$ orientations are almost energetic degenerate though the $\alpha - \alpha$ orientation is slightly favored within this artificial UC. The $\alpha - \beta$ orientation is indeed more stable than $\alpha - \alpha$ orientation on EG, by taking into account the intermolecular interaction between Pc molecules in the incommensurate lattice as well as the van der Waals force between Pc and EG, which also explains more $\alpha - \beta$ orientation appeared in
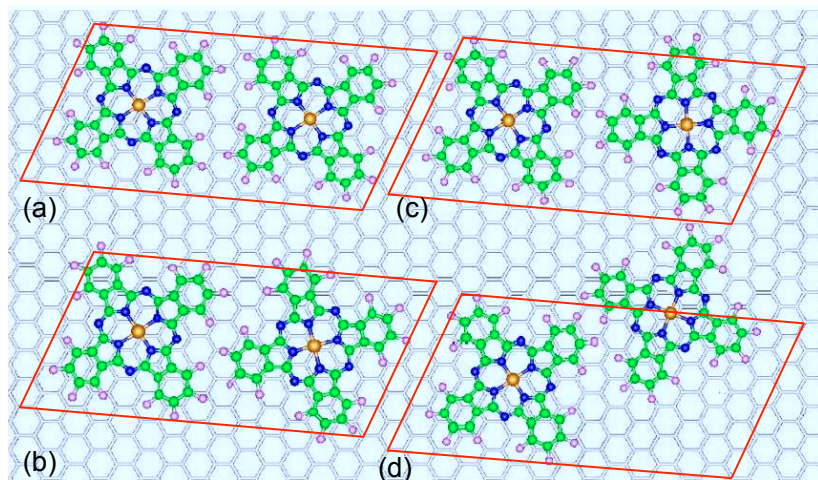
Figure 6.12: Configurations of uniform and non-uniform $F_{16}CuPc$ overlayers adsorbed on graphene[(3,4)×(8,6)]. (a) the $\alpha - \alpha$ pattern, and the $\alpha - \beta$ stripes with relative azimuthal angles of (b) 20°, (c) 30° and (d) 40°. The unit cell (red parallelogram) contains two Pc molecules.
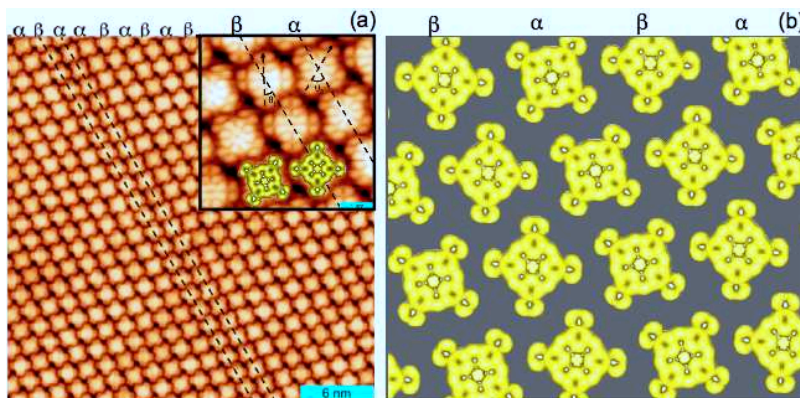
Figure 6.13: High-resolution STM images[221] (a) and the simulated STM (b) of ordered $F_{16}CuPc$ patterns on epitaxial graphene. The inset in pattern (a) is the enlarged STM image.

the STM image. Furthermore, the simulated STM images based on the charge density of LUMO, as displayed in Fig. 6.13b, match excellent with the STM images in Fig. 6.13a. Our results of the calculated HOMO and LUMO images also appear a brighter spot in the central Cu position for the LUMO of molecules and darker for its HOMO.

Theoretical investigations on the fullerene and copper phthalocyanine heterojunciton

Organic photovoltaic (OPV) cells have attracted a tremendous amount of attention as promising alternatives to established inorganic technologies, because of their incomparable advantages such as low cost, easy fabrication, excellent flexibility, and compatibility with large-area substrate.[224–226] A molecular heterojunction based on copper phthalocyanine (CuPc) and fullerene (C_{60}) are widely applied in OPV cells as an electron donor-acceptor pair. Although the molecular orientation of CuPc on C_{60},[227,228] the corresponding band alignment[229,230] and ultrafast charge transfer at the CuPc/C_{60} interface[231] are widely investigated from the experimental point of view, the atomic structure and the relevant interaction between the CuPc and C_{60} thin film are not well understood at the atomic level. In this chapter, we investigate the atomic structure and electronic properties of a CuPc molecule adsorbing on a C_{60} surface with the lying-down and the standing-up molecular orientations, through first-principles calculations based on DFT. In addition, we explore the relevant optical properties for different configurations by using TDDFT. Moreover, we elucidate the difference of the electronic interaction for the distinct CuPc/C_{60} configurations with different molecular orientations. Based on the optimized geometries of the CuPc/C_{60} molecular heterojunction, we extend to construct two models to simulate the thin film heterojunction: CuPc monolayer deposit on $C_{60}(001)$ surface with the lying-down molecular orientation, and upon $C_{60}(111)$ surface with the standing-up configuration. Our results predict that the former one shows a higher efficiency of charge transfer at the interface than that in the latter one, because of the larger overlap and stronger electronic interaction between CuPc and C_{60} molecules.
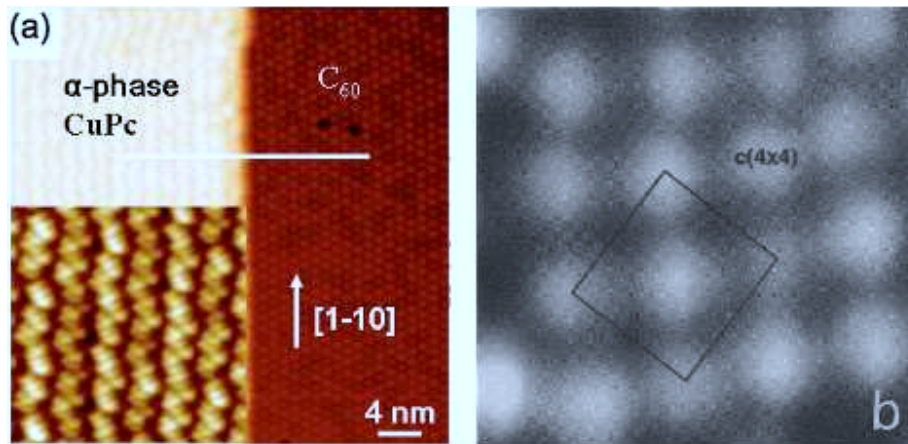
Figure 7.1: (a) Scanning tunneling microscopy (STM) image of α-phase CuPc on C_{60}/Ag(111), and the relevant CuPc molecular arrangement. C_{60} shows a close-packed hexagonal lattice.[227] (b) STM image shows the c(4×4) molecular ordering of C_{60} molecules on the Si(100)-(2×1) surface.[236]

7.1 Lying-down vs standing-up for CuPc molecular orientation

For the CuPc/C_{60} heterojunction, which molecular orientation: **lying-down** or **standing-up**, does CuPc molecule prefer to adopt when adsorbing on the C_{60} surface? To address this question, special attention is paid to study the interfacial geometries mainly through scanning tunnelling microscopy (STM).

For the low coverage of CuPc molecule deposited on a Au(111) surface covered by a monolayer of C_{60}, the molecules prefer to lie flat on the surface,[228] in consistent with CuPc molecule deposition on graphite,[223] Ag(111),[227,232] Cu(111),[233] and TiO$_2$(011)-(2×1) surface.[234] For the high coverage of CuPc thin film adsorption upon C_{60}/Ag(111), CuPc molecules adopt a standing-up orientation on C_{60} monolayer,[227] as shown in Fig. 7.1a. However, CuPc molecules adopt a lying-down orientation with the square lattice adsorbing on the C_{60}/MoS$_2$ system[235] for a coverage of monolayer. The lying-down or standing-up molecular orientation relies primarily on the competition between the molecule-substrate interaction and intermolecular interaction. If the electronic interaction of CuPc and C_{60} is stronger than the CuPc-CuPc interaction, CuPc molecules prefer to lie flat on the C_{60} surface; otherwise, they would like to adopt a standing-up orientation.

In addition, the molecular arrangement and lattice commensuration of C_{60} monolayer on the substrate is another important factor which influences the orientation of CuPc molecules on C_{60} surface. The STM images indicate that a C_{60} monolayer forms a hexagonal lattice on Si(111)-(7×7) surface, and a square lattice with a c(4×4) ordering on Si(100)-(2×1) surface[236] (see Fig. 7.1b). The distance of the two nearest C_{60} molecules is 10.2 Å and 10.9 Å for the hexagonal and square lattice, respectively. Compared with the crystalline C_{60} structure, the distance for the near-
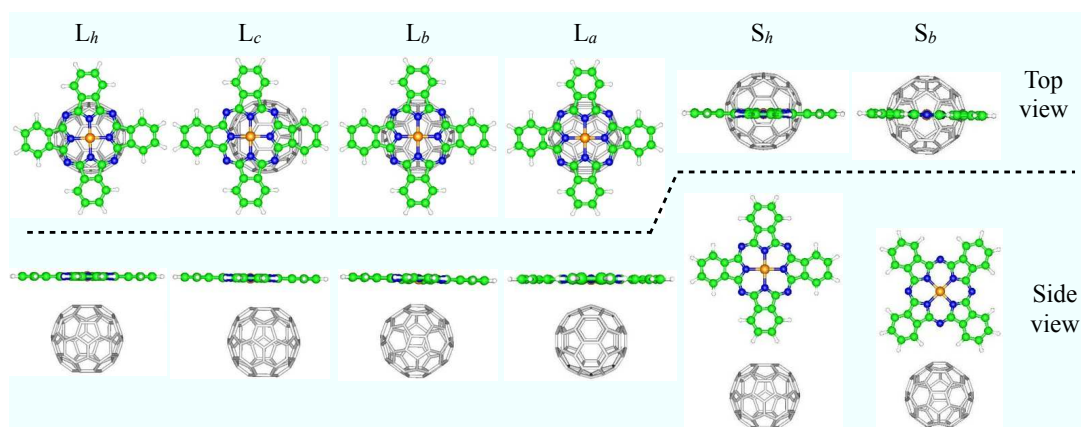
Figure 7.2: Different configurations for CuPc adsorption upon C$_{60}$ surface. L$_h$, L$_c$, L$_b$, and L$_a$ represent the distinct lying-down orientations; while S$_h$ and S$_b$ mark the standing-up geometries. Top view (above) and side view (below) are separated by a black dash line. C, H, N, Cu atoms are denoted as gray, white, blue and orange spheres, respectively. To distinguish, C atoms in Pc molecules are shown in green spheres.

est neighbor is 10.02 Å,[237] suggesting a smaller lattice mismatch existed between C$_{60}$ monolayer and Si(111)-(7×7) surface. Thus crystalline C$_{60}$(111) film growth occurs. The same phenomena are also observed on other metal substrates.[228,238,239] On the other hand, a large lattice mismatch between the CuPc square lattice (∼14 Å) with the lying-down molecular orientation and the close-packed C$_{60}$ hexagon lattice (10.02 Å) exclude the possibility of CuPc molecule adsorption upon C$_{60}$(111) with the lying-down orientation. However, the lattice vector of the C$_{60}$(001) surface is 14.17 Å, which exhibits excellent commensuration with the CuPc square lattice. Therefore, C$_{60}$(001) surface provides a good opportunity for CuPc molecules to lie flat on the surface, whereas C$_{60}$(111) surface shows a possibility for CuPc adsorption with the standing-up molecular orientation.

7.2 CuPc/C$_{60}$ molecular complex

7.2.1 Atomic structure

To start, we have studied the simplest model for the molecular complex of single CuPc molecule and C$_{60}$ molecule. The computational details are the same as in chap. 6. We define the adsorption site as the projection on C$_{60}$ of the central Cu atom of CuPc. Four different adsorption sites for CuPc lying down on C$_{60}$ surface, including the center of a hexagon (L$_h$), the top site of a C atom in a hexagon (L$_c$), the bridge site (L$_b$), and the apex C atom (L$_a$) of C$_{60}$, and two standing-up configurations, such as the top site of a hexagon (S$_h$) and the bridge site (S$_b$), have been investigated, as shown in Fig. 7.2.

Based on their optimized configurations, the respective binding energies, the structural parameters and the static charge transfer for the different CuPc/C$_{60}$ molec-

ular complexes are summarized in Table 7.1. We ignore the discussion of CuPc adsorption upon a pentagon of C_{60} molecule, because there are only 2 meV energy differences existing for the same absorption site on both surfaces.

Table 7.1: Calculated energies, adsorption height and charge transfer for these six CuPc/C_{60} complexes, as defined in Fig. 7.2[a].

Geometry	E_{b1}	E_{b2}	E_{b3}	$d_{Cu-C_{60}}$	$d^*_{Cu-C_{60}}$	$\Delta\rho$
L_h	–0.53	–0.27		3.041		0.015
L_c	–0.61	–0.33		2.978		0.020
L_b	–0.67	–0.37	–0.65	2.639	2.939	0.010
L_a	–0.64	–0.37	–0.64	2.587	2.887	0.004
S_h	–0.15	–0.11		2.525		–0.009
S_b	–0.25	–0.17	–0.22	2.363	2.714	–0.007

[a] Different binding energies (E_{b1}, E_{b2} and E_{b3}) and the averaged adsorption heights ($d_{Cu-C_{60}}$ and $d^*_{Cu-C_{60}}$) correspond to different exchange-correlation functionals used, see text. The unit of the binding energy, adsorption height and charge-transfer from Pc to C_{60} is eV, Å and e, respectively.

In Table 7.1, the binding energy is defined as:

$$E_{b1} = (E_{tot} - n(E_{C_{60}} + E_{Pc}))/n \tag{7.1}$$

where E_{tot}, $E_{C_{60}}$, and E_{Pc} is the total energy of the complex, the energy of the isolated C_{60} molecule, and the energy of gas-phase Pc molecule, respectively. n is the number of Pc and C_{60} molecules in a unit cell. The binding energy of E_{b2} excludes the basis set superposition error (BSSE), relative to the E_{b1}. E_{b3} is obtained by considering van der Waals (vdW-DF) functionals and excluding the BSSE in the calculations. Accordingly, the averaged adsorption height $d_{Cu-C_{60}}$ corresponds to the LDA results, while $d^*_{Cu-C_{60}}$ is the result of using vdW-DF functionals and excluding the BSSE. From our results, the overall binding energies for the lying-down molecular orientations range from –0.53 eV (L_h) to –0.67 eV (L_b) in LDA, but only –0.15 eV (S_h) and –0.25 eV (S_b) for the standing-up geometries, suggesting that the former orientations are energetically favorable for CuPc adsorption. Even if the BSSE is excluded, the relevant binding energies of the lying-down configurations decrease dramatically, but it does not change the general trend: $L_b > L_a > L_c > L_h > S_b > S_h$. The stronger binding energy for the lying-down molecular orientations is attributed to the larger overlap between CuPc and C_{60} molecule, in comparison with that of the standing-up configurations. On the other hand, the weak CH-π interaction for the standing-up configurations also indicates that the stability of the standing-up orientation is weaker.

Among the four lying-down orientations, L_b is the most stable one, indicating CuPc molecule prefers to locate on the bridge site of C_{60}, with one N-Cu-N bond being parallel to the C-C bond of C_{60} molecule. This can be explained by the shorter

adsorption height, the stronger electronic interaction. The adsorption height for L$_b$ is 2.639 Å, which is shorter than that of L$_h$ (3.041 Å) and L$_c$ (2.978 Å). Although the latter two configurations have larger contact area, the 0.3 Å longer distance weakens the strength of the interaction at the interface. In contrast, the adsorption height of L$_a$ is 2.587 Å, which is slightly shorter than that of L$_b$. However, the slightly smaller overlap between C$_{60}$ and Pc in comparison with L$_b$ results in the latter configuration being slightly more energetically favorable. Therefore, the strength of the electronic interaction ultimately relies on the competition of the contact area and the distance between CuPc and C$_{60}$ molecule. For the standing-up molecular orientations, the bridge site is still the preferential site for CuPc adsorption on C$_{60}$. Compared to S$_h$, two benzene rings of S$_b$ point towards the C-C bond of C$_{60}$ with the H-C bond-length of 2.363 Å, $\sim$0.2 Å shorter than that of the S$_h$ geometry. The shorter bond-length and the larger overlap between CuPc and C$_{60}$ determines the preference of S$_b$. This is consistent with the competition mechanism used in the analysis of the lying-down configurations.

To obtain the accurate binding energy, we focus on three stable configurations, including L$_b$, L$_a$ and S$_b$, by using vdW-DF functional. The corresponding binding energy is –0.65, –0.64, and –0.22 eV, respectively, also confirming the stability of the bridge site for CuPc adsorption upon C$_{60}$, which is in good agreement with the same trend for the ZnPc/C$_{60}$ system.[240] In comparison with LDA results, the respective binding energy is almost the same, but the adsorption height increase by $\sim$0.3 Å.

7.2.2 Charge transfer

To clarify the electronic interaction between CuPc and C$_{60}$, we calculate the corresponding charge density differences (CDD) (see Fig. 7.3a-b) to describe the bonding character and charge redistribution upon CuPc molecule adsorption. The definition of CDD is

$$\Delta\rho = \rho_{tot} - \rho_{C_{60}} - \rho_{Pc} \tag{7.2}$$

where ρ_{tot}, $\rho_{C_{60}}$, and ρ_{Pc} is the charge density of the molecular complex, isolated C$_{60}$ and CuPc molecule with geometries fixed at the optimized ones in CuPc/C$_{60}$ complex. For the calculated CDD, it is obvious that an interfacial layer of the electron-accumulation is generated between CuPc and C$_{60}$ molecule. For the lying-down orientation, more electrons accumulate in the interfacial layer for L$_b$ and L$_a$ than that for L$_h$ and L$_c$. For the standing-up ones, more electrons accumulate for S$_b$.

Integrating the CDD along the C$_{60}$-CuPc direction z, we get the planar averaged CDD, as shown in Fig. 7.3c-d. In general, the CDD amplitude of the lying-down molecular orientations is much larger than the standing-up orientations, indicating a larger electron-polarization for the lying-down configuration. In turn, the large electron-polarization at the interface also enhance the electronic interaction between CuPc and C$_{60}$. Quantitating the planar average CDD, we obtain 0.015 (L$_h$), 0.020 (L$_c$), 0.010 (L$_b$), and 0.004e (L$_a$) of electrons (see Table 7.1) transferring from CuPc to C$_{60}$, confirming the character of the electron donor-acceptor pair. Although the L$_b$ is the optimized configuration for CuPc adsorption, more charge accumulation
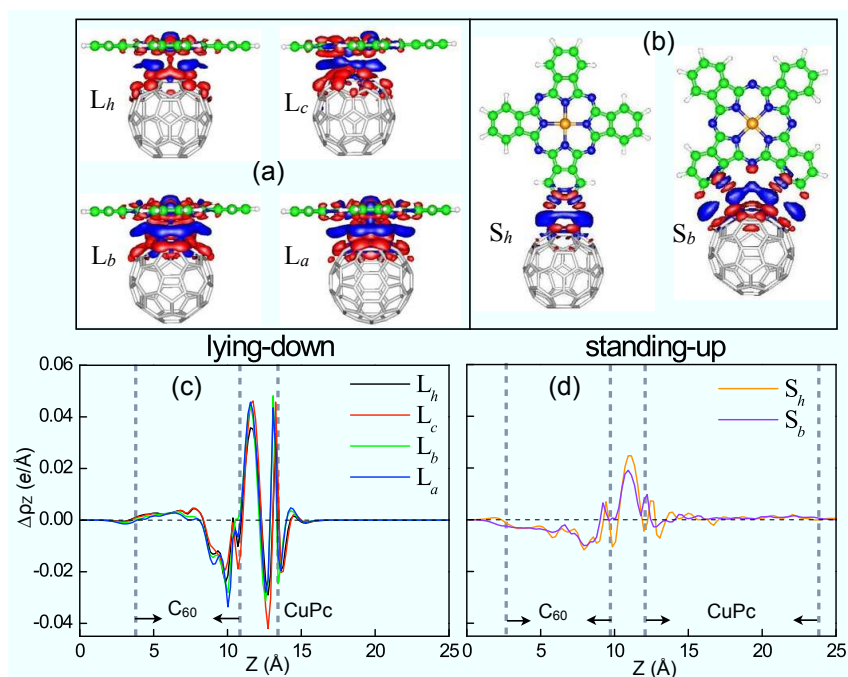
Figure 7.3: Side view of the charge density difference for the lying-down CuPc/C_{60} configurations (a) and the standing-up geometries (b) at contour level of $0.03e/\text{Å}^3$. The blue and red clouds correspond to regions with electron accumulation and depletion, respectively. Planar averaged charge density difference along the C_{60}-CuPc direction for the lying-down symmetries (c) and the standing-up ones (d), respectively. The gray vertical lines in (c) and (d) mark the positions of CuPc and C_{60}.

on C_{60} is observed for L_h and L_c, because of the large overlap and strong electronic interaction for CuPc adsorbing on a hexagon surface of C_{60}. The standing-up geometries such as S_h and S_b configurations, however, display different character of the charge transfer. –0.009e for S_h and –0.007e for S_b indicate smaller charge transfers from C_{60} to CuPc, because of very weak CH-π interaction and smaller overlap between two molecules.

7.2.3 Electronic and optical properties

In experiment, the optical absorbance spectra is used to identify the structure change based on the molecular adsorption. To distinguish the lying-down and standing-up configurations, we calculate the optical properties of the three geometries, including L_b, L_c and S_b using TDDFT. From Fig. 7.4, it is clear that both lying-down and standing-up configurations show two major absorbance bands, ranging from 610 nm to 650 nm for the band I and 300-420 nm for the sequent band II. In comparison with the isolated CuPc and C_{60} molecule, the band I is mainly attributed as the contribution of CuPc, and the band II is composed of major contribution of CuPc and part of C_{60}, which is consistent with the primary peak measured in ultraviolet (UV)-vis spectra for both isolated molecules.[58,237]
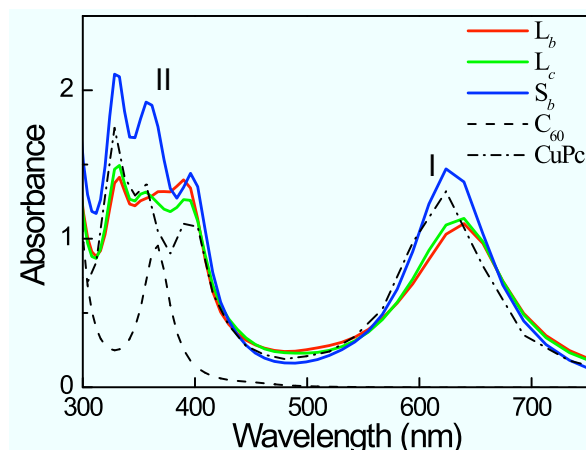
Figure 7.4: UV-vis spectra of CuPc adsorption upon C$_{60}$ surface calculated from TDDFT. Red, green, and blue solid line represents the CuPc/C$_{60}$ system with the L$_b$, L$_c$ and S$_b$ symmetry, respectively. Black dash and dash-dot line shows the absorbance bands for the isolated C$_{60}$ and CuPc molecule.

For the lying-down configurations, the first peak of L$_b$ and L$_a$ is located at 640 nm, with a shoulder at 624 nm. The second sequent band for L$_b$ is at 390, 372, and 333 nm, but for L$_a$, the absorption peak is at 390, 356 and 333 nm with switching the ordering of the intensity for the peaks at 390 and 356 nm. For the standing-up configuration, the first peak of S$_b$ shifts to 624 nm and the second band is at 396, 356, and 328 nm, with enhancement of the intensity. The red shift and the decreased intensity of the first absorption peak for the lying-down configuration can be used to identify it from the standing-up structure.

To elucidate the nature of the absorption peaks, we analyze the electronic structure of the L$_b$ and S$_b$ configurations. The corresponding band alignment and the wavefunctions of these states are presented in Fig. 7.5. Upon CuPc adsorption, the highest occupied molecular orbital (HOMO) of the CuPc/C$_{60}$ complex is ascribed to the contribution of CuPc, while the lowest unoccupied molecular orbital (LUMO) of the complex is from that of C$_{60}$. The HOMO and the LUMO state of CuPc is composed of a singly occupied molecular orbital (SOMO), which is depicted as $b_{1g\uparrow}$ and $b_{1g\downarrow}$ orbital, respectively. The respective HOMO–1 and LUMO+1 states comprise doubly-degenerate a_{1u} spin-orbitals and two doubly-degenerate e_g spin-orbitals. The HOMO and LUMO states of C$_{60}$ comprise 5 doubly-degenerate and 3 doubly-degenerate spin-orbitals, respectively. The band gap is 0.92 eV for the L$_b$, which is in excellent agreement with the experimental results of 1.03 eV,[229] and the band gap of 0.63 eV corresponds to the S$_b$ configuration. The energy difference $(E_{C_{60}}^{LUMO} - E_{CuPc}^{HOMO})$ of 0.3 eV higher for L$_b$ than that for S$_b$ also indicates that the larger circuit voltage can be obtained for the lying down configuration. Considering the stronger couplings between CuPc and C$_{60}$ and the larger electron polarization, the lying-down configuration is more favorable for exciton dissociation at the Pc/C$_{60}$ interface.

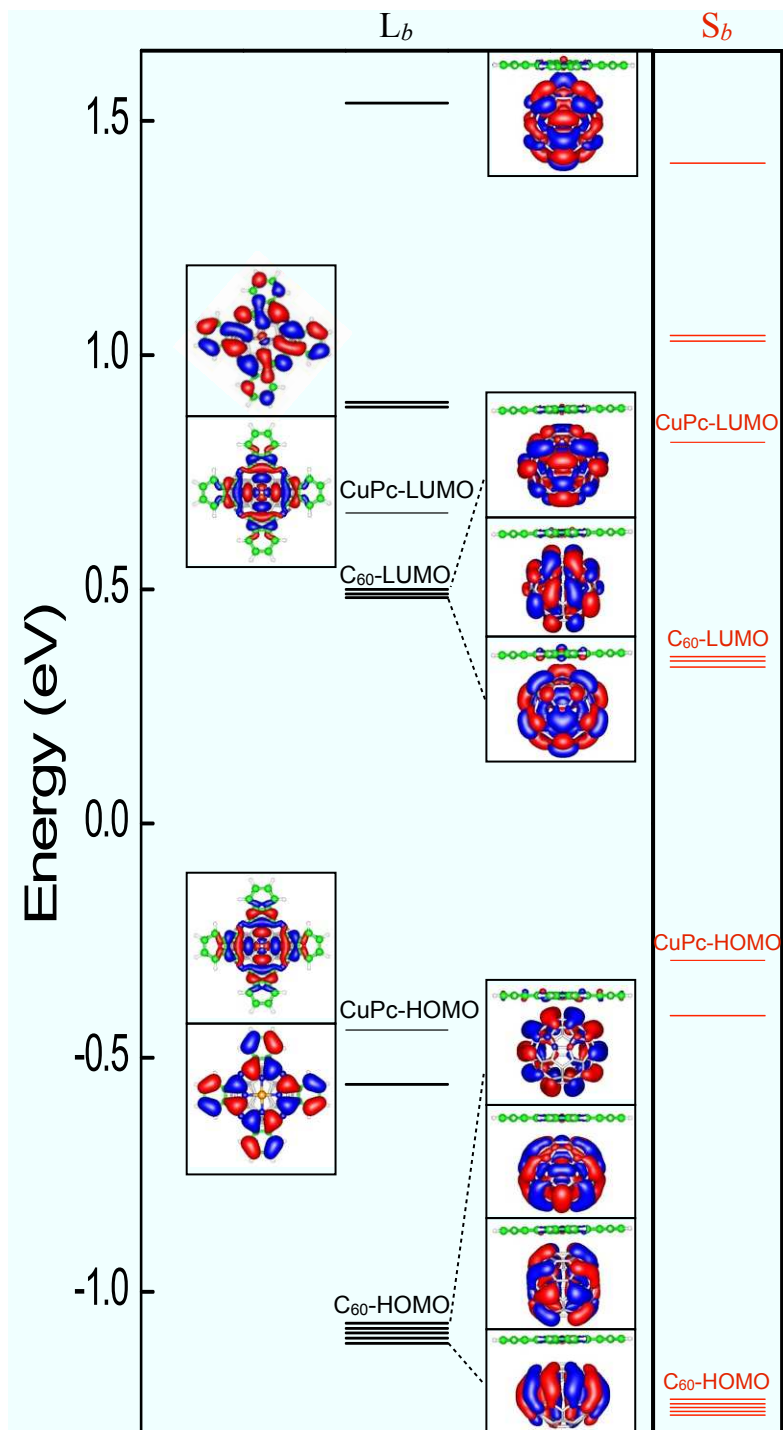Combining with the UV-vis absorbance spectra (see Fig. 7.4), we find that the

Figure 7.5: Band alignment and the relevant wavefunction of each state for the CuPc/C_{60} system with L_b (black lines) and S_b (red lines) geometry, respectively.

peak at 640 nm for the L$_b$ and 624 nm for the S$_b$ is not attributed to electronic excitations from the HOMO to LUMO states of the CuPc/C$_{60}$ complex. It is worth pointing out that the first absorption band corresponding to the transition between the HOMO and LUMO states of the CuPc/C$_{60}$ complex should be around 1200 nm for L$_b$ and 1500 nm for S$_b$. However, this absorption band is difficult to detect in experiments, due to very small intensity. As a result, the band I at 640 nm (L$_b$) and 624 nm (S$_b$) is corresponding to the transition from the HOMO to the LUMO state of CuPc molecule. The band II in both configurations are primarily composed of the HOMO–1$\rightarrow$ LUMO, HOMO$\rightarrow$LUMO+1, and HOMO–1$\rightarrow$LUMO+1transition of CuPc molecule.

Compared to the S$_b$ configuration, the band gap of the L$_b$ configuration is much larger than that of the S$_b$, suggesting a large blue shift for the absorption band (1200 nm) for the L$_b$. In addition, the band levels of C$_{60}$ shift towards the higher position without changing the energy difference between the HOMO and LUMO states, because C$_{60}$ is very stable, and Pc adsorption does not change the electronic structure of C$_{60}$ molecule. The band levels of CuPc, however, shift to lower position. Furthermore, the L$_b$ configuration moves the HOMO and LUMO states of CuPc closer which accounts for the observed red shift in the band I discussed earlier.

7.3 CuPc/C$_{60}$ thin film heterojunction

7.3.1 CuPc adsorption on C$_{60}$(001) or (111) surface

Based on the optimized structures of the CuPc/C$_{60}$ complex (L$_b$ and S$_b$), we extend it to simulate the CuPc/C$_{60}$ thin film heterojunction by considering two kinds of supercells with periodic boundary condition. 1) For the lying-down molecular orientation, we adopt a square lattice with the lattice vector of 14.17 Å to simulate the CuPc/C$_{60}$(001) system. A unit cell contains two C$_{60}$ molecules and one CuPc molecule, as shown in Fig. 7.6a. 2) For the standing-up orientation, a rhombus lattice with the lattice vector of 10.02 Å is applied to simulate the CuPc/C$_{60}$(111) system. Only one C$_{60}$ and one CuPc is included in a unit cell, as depicted in Fig. 7.6b. A vacuum layer for both configurations are exceeding 10 Å.

The difference between two models is that there are two C$_{60}$ molecules and one CuPc molecule in a unit cell for the lying-down orientation, but only one C$_{60}$ and one CuPc molecule in a unit cell for the standing-up configuration. The averaged adsorption height is 2.812 Å and 2.363 Å for the lying-down and standing-up configuration, respectively. The corresponding binding energy is –1.16 and –0.82 eV/C$_{60}$, which includes interactions between CuPc and C$_{60}$ and the intra-layer couplings within C$_{60}$ and CuPc thin films. Excluding the BSSE, the relevant binding energy changes to –0.33 and –0.15 eV/C$_{60}$ for the lying-down and standing-up configuration, respectively. Therefore, the binding energy of the lying-down configuration is two times larger than that of the standing-up structure, suggesting a more stable configuration of CuPc adsorption upon C$_{60}$(001) surface. This result is consistent
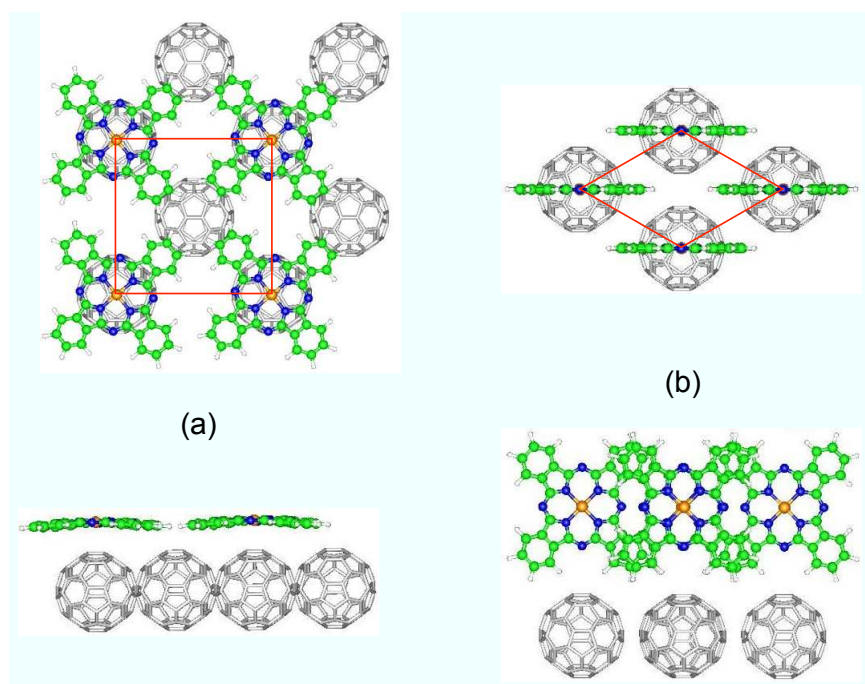
Figure 7.6: Top and side view of different configurations of CuPc/C_{60} thin film heterojunction. (a) CuPc molecules deposit on C_{60}(001) surface, and (b) on C_{60}(111) surface. The red square and rhombus represents the corresponding unit cells.

with the trend of the stability for the isolated CuPc/C_{60} complex. Moreover, the larger binding energy (–1.16 eV/C_{60}) for the CuPc adsorption on C_{60}(001) surface than that of L_b (–0.67 eV) in CuPc/C_{60} complex, indicates the enhancement of the stability of CuPc/C_{60} interface, when C_{60}(001) surface is covered by CuPc monolayer. For the CuPc/C_{60}(111) thin film heterojunction, the interaction at the interface is also enhanced by depositing CuPc monolayer with the standing-up orientation.

As discussed in previous section, the arrangement of C_{60} monolayer on the substrate and the lattice mismatch between CuPc and C_{60} is another critical factor that influences the CuPc molecular orientation on C_{60}. STM images reveal that CuPc molecules adopt a standing-up molecular orientation on C_{60} monolayer deposited on Ag(111),[227] as shown in Fig. 7.1a. It is clear that C_{60} monolayer forms a close-packed hexagonal lattice, namely C_{60}(111) surface on Ag(111). The large lattice mismatch between the CuPc monolayer with the lying-down molecular orientation and the C_{60}(111) surface exclude the possibility of the lying-down orientation for CuPc adsorption. Although the C_{60}(111) surface is common observed face in experiments. However, on Si(100)-(2×1) and MoS$_2$ substrate, C_{60} molecules form a square lattice with c(4×4) ordering,[235, 236] namely C_{60}(001) surface. C_{60}(001) surface offer a good opportunity for CuPc to deposit a monolayer with the lying-down orientation. Based on the comparison of the stability, charger transfer and electronic interaction for the lying-down and standing-up configuration, we predict that the CuPc/C_{60}(001) thin film heterojunction facilitates charge transfer from CuPc to C_{60} and has a higher stability, because of the larger overlap and stronger electronic

interaction between CuPc monolayer and C$_{60}$(001) surface.

7.3.2 Electronic properties of the CuPc/C$_{60}$(001) system

Since the lying-down configuration have more advantages over the standing-up geometry, we focus on the CuPc adsorption upon C$_{60}$(001) surface. The relevant band alignment and wavefunction for each state is shown in Fig. 7.7. It is clear that the HOMO and LUMO state of the system is still attributed to the contribution of CuPc and C$_{60}$, respectively. The HOMO state is composed of SOMO of CuPc, and the LUMO states contain 6 doubly-degenerate orbitals of C$_{60}$. When an electron is excited from the HOMO to the LUMO state of the CuPc molecule, it will first dissipate onto both C$_{60}$ molecules equally, then hop back-and-forth between two C$_{60}$ molecules, and then redistribute on both molecules, and finally diffuse away. This whole picture of the electron hopping shed light on understanding the charge transport at the CuPc/C$_{60}$ interface. In comparison with the CuPc/C$_{60}$ complex (L$_b$), the band gap decreases to 0.86 eV, the energy difference between the HOMO and LUMO of CuPc does not change. Consequently, the band I of the CuPc/C$_{60}$(001) heterojunction should be at ∼640 nm, the same as the isolated complex. The intensity, however, should be enhanced because of the additional electronic interaction between CuPc and the second C$_{60}$ molecule.

Our results predict that the CuPc/C$_{60}$(001) thin film heterojunction is more feasible for the charge transfer from CuPc to C$_{60}$ than the CuPc/C$_{60}$(111) system, due to large overlap between two molecules and stronger electronic interaction at the interface. As a result, CuPc molecules adsorption on C$_{60}$(001) surface with the lying-down molecular orientation would lead to a new direction of designing more stable OPV cells with higher efficiency of charge transfer in the future.
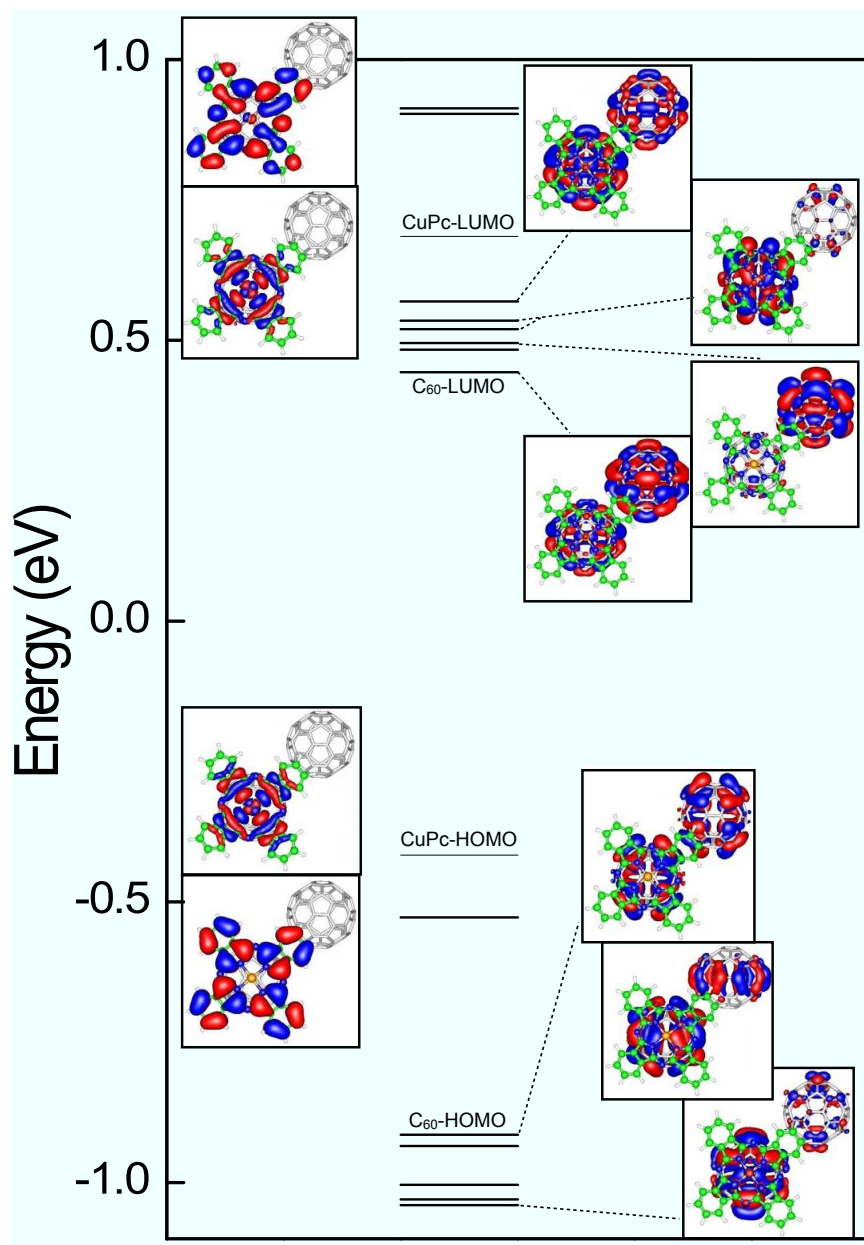
Figure 7.7: Band alignment and the relevant wavefunction of each state for the CuPc/C_{60}(001) system.

Conclusions and Perspectives

With wide applications of organic molecules in pharmacological fields as anti-inflammatory, anti-cancer, and antioxidants, in dye sensitized solar cells as light absorbers, and in organic photovoltaic cells as electron conductors, researchers pay tremendous attention to the investigation of the organic molecules and their interface with other materials. The interfaces, with metals, inorganic and organic semiconductors, determine the exceptional thermal, chemical, electronic, and optical properties of these hybrid systems and the usage of organic molecules. In particular, a full understanding of the performance and properties of the organic-inorganic interfaces ultimately depends on a complete knowledge about the atomic geometry at the interface and the associated electronic interactions.

In this thesis, we have investigated several important interfaces comprising organic molecules, and explored the corresponding electronic and optical properties using first-principles calculations within the framework of density functional theory (DFT) and time-dependent DFT (TDDFT) with a self-consistent field (SCF). Very different interfaces are considered: We have studied the complexation mechanism of flavonoids with iron ions, the charge injection process in the natural cyanidin dye sensitized TiO_2 solar cells, the molecular arrangements of $F_{16}CuPc$ and CuPc molecules adsorbed on graphene, and the electronic couplings between CuPc molecule and the $C_{60}(001)$ and (111) surfaces. These systems range from small molecules to complex interface structures ($\sim$400 atoms), and the obtained results on atomic geometry, electron transfer, and optical absorption are generally in good agreement with available experimental data, approving the computational efficiency and accuracy of our methods, and the success in dealing with the electronic structure of interfaces involving organic molecules. A special attention is paid to elucidate the correlation between atomic configurations and unique electronic and optical properties, and to demonstrate the mechanism of electronic couplings at the atomic scale.

To look forward, so many unknowns ahead of us about the electronic interaction between organic molecules and the interfaces point to potential directions for future

research. First of all, photovoltaic devices based on organic molecules, including dye-sensitized types and purely organic ones, are still in the infancy of their development. The sunlight-to-electricity conversion efficiency is still limited to 12% for DSCs and 6% for OPVs. To make them commercially competitive and implementable on a large scale, a higher efficiency is general required. Is it possible in these devices to achieve a conversion efficiency higher than 16%? And how? It is still a great challenge and a pressing issue to our society. Secondly, organic molecules are usually less stable than inorganic materials. They can easily get bleached, disassembled, or detached from substrate under intensive UV illumination, making them unsuitable for long-term ($\geq$25 years) outdoor applications. However could we improve the stability of some critical organic molecules, such as phthalocyanines or new high-extinction-coefficient dyes? How could we obtain a more stable interface with desirable structures and boundaries? Can we probably increase the lifetime of the interface by designing more and stronger anchoring groups to enhance molecule-surface binding? These questions need to be answered. Thirdly, we need to develop experimental techniques that are capable of detecting molecular and interface structures at the atomic scale. For instance, there is no direct experimental information on the position and number of iron ions for the Fe-quercetin complexes. Lacking of such data makes it difficult to test theoretical predictions and insights, and to establish correct structure-property relationships about the organic-inorganic interface. Currently most available experimental data are indirectly inferred from spectroscopic measurements; such information is mostly averaged over a large ensemble and a long time, and is hard to interpret. Straightforward real-space and real-time techniques, such as photon-assisted Atomic Probe Microscopy and atomic probes that operate at ambient conditions, need to be developed to resolve some of these puzzles.

All above can benefit from more accurate description and better material design of organic molecules and their interface structures. If we could design stable organic molecules with higher extinction coefficients and intense infrared-red light absorption, and engineer interfaces with desirable geometry, electronic band offsets, and stronger couplings, we could probably build a solar cell based on these novel molecules and interfaces with an energy conversion efficiency $\geq$20% and an extended lifetime ($\geq$30 years). This requires us to continuously develop computational approaches which are realistic, accurate, and efficient for describing organic molecules and their interfaces. To this end, i) we need to improve the accuracy of calculations on electronic structures of large organic complexes and band-offsets at interfaces. In our calculations of on phthalocyanine-fullerene interface, the absolute value of bandgaps and band alignments is much underestimated in LDA. Although the relative band levels provides an indication of electronic structure change upon interface interaction, precise band offsets are required for correctly predicting device performances such as the open-circuit voltage. Hybrid functionals, TDDFT approaches, as well as some efficient quantum chemistry methods offer an opportunity for improvement. ii) We have to improve further the efficiency of our methods. In general, ab initio methods dealing with the system including over 200 atoms is

extremely expensive. Unfortunately, functional organic molecules and related interfaces, are usually large and complex, easily going beyond 200 atoms. In addition, obtaining longer simulation time without divergency would enable us to simulate charge injection processes at the 100-picosecond level. We need efficient methods which handle nicely both the size and time limits. iii) Including solvent effects is the next challenge. Many devices based on organic molecules perform in organic solvents. To simplify, we usually use implicit polarizable continuum medium or small molecules such as water to model the influence of solvents on electronic interactions. Understandably this is a rough, and sometimes unjustified, approximation. It would be interesting to study explicitly the dynamics of solvent molecules, in particular, their roles in maintaining the functionality of devices. In brief, developing accurate and efficient theoretical and computational models to study organic molecules and their function in biological and photovoltaic environments is complementary to experimental investigations, which are normally costly and time-consuming; it will significantly contribute to our understanding and further improvements of device performance in sensors and solar cells via better material design.

Acknowledgments

Every time when I read through my thesis, my heart is full of happiness and gratitude, because the Ph. D. education is an inspiring and challenging journey. I would like to express my appreciation to all who have contributed to this thesis in many ways.

My supervisor, Prof. Efthimios Kaxiras, provides me useful suggestions and help in all aspects. He deserves many thanks. His vision and ability to grasp the essence of physics in a complicated problem, his deep and vast knowledge on the solid state field, and his enthusiasm on sciences have guided me to become a qualified candidate for a doctorate. I appreciate very much all his kind advices and guidance during my Ph. D. study.

I would like to thank Prof. Nava Setter for providing me lots of good opportunities to be involved in the social and professional activities in EDMX at EPFL. In particular, her moral support encourages me to overcome all difficulties during the final stage of my doctoral education.

All collaborators are acknowledged. I really appreicate Prof. Sheng Meng for his support, guidance, and collaboration during my whole Ph. D. study. I would like to thank Christina Lekka, Prof. Xucun Ma, Prof. Qikun Xue, Prof. Gerrit E.-W. Bauer, Prof. Efstratios Manousakis, and Prof. Anna Fontcuberta i Morral for much fruitful discussion. I would also like to thank the members of my thesis jury: Prof. Dr. Thomas Frauenheim, Prof. Zhengxiao Guo, Prof. Anna Fontcuberta i Morral, and Prof. Harm-Anton Klok.

I then would like to express my gratitude to the previous members in the Laboratory of Multiscale Modeling of Materials from both a professional and personal point of view. I am very grateful to our former secretary Ms. Doris Sapin, for taking care of administrative and my personal matters. A number of my colleagues deserve special mention for their help and sharing ideas: Maria Fyta, Peirfrancesco Rosini, Georg Schusteritsch, Hsiang-Han Tseng, Jonas Latt, and Jan M. Knaup.

A word of appreciation goes to my friends around the world: Yanxing Zheng, Xiahan Sang, Tess Zangrill, Florence Ven, Sanhao Ji, who make my life cheerful.

Lastly I would like to thank my family for their deep love and eternal support, which is a permanent strength-fountain to support me to challenge and develop myself ceaselessly.

Bibliography

[1] K. Herrmann, J. Food Tech. 11, 433 (1976).

[2] E. Middelton, C. Kandaswami, in: J.B. Harborne (Ed.), *The Flavonoids: Advances in Research Since 1986*, Chapman and Hall, London, 1994.

[3] R. F. V. de Souza, W. F. De Giovani, Redox Report 9, 97 (2004).

[4] S. R. Husain, J. Cillard, P. Cillard, Photochemistry 26, 2489 (1987).

[5] M. L. Brandi, Bone Mineral 19, S3 (1992).

[6] E. Middleton, C. Kandaswami, Biochem. Pharmacol. 43, 1167 (1992).

[7] B. H. Havsteen, Pharmacol. Therapeut. 96, 67 (2002).

[8] C. A. Rice-Evans, N. J. Miller, G. Paganga, Free radical biology & Medicine 20, 933 (1996).

[9] S. V. Jovanovic, S. Steenken, M. Tosic, B. Marjanovic, M. G. Simic, J. Am. Chem. Soc. 116, 4846 (1994).

[10] S. A. B. E. van Acker, G. P. van Balen, D. J. van den Berg, A. Bast, W. J. F. van der Vijgh, Biochem. Pharmacol. 56, 935 (1998).

[11] I. B. AfanasÕev, A. I. Dorozhko, A. V. Brodskii, V. A. Kostyuk, A. I. Potapovitch, Biochem. Pharmacol. 38, 1763 (1989).

[12] M. Melidou, K. Riganakos, D. Galaris, Free Radical Biol. Med. 39, 1591 (2005).

[13] H. J. H. Fenton, J. Chem. Soc. 65, 889 (1894).

[14] F. Haber, J. J. Weiss, Proc. R. Soc. London, Ser A 147, 332 (1934).

[15] A. Torreggiani, A. Trinchero, M. Tamba, P. Taddei, J. Raman Spectrosc. 36, 380 (2005).

[16] J. P. Cornard, J. C. Merlin, J. Inorg. Biochem. 92, 19 (2002).

[17] M. Leopoldini, N. Russo, S. Chiodo, M. Toscano, J. Agric. Food Chem. 54, 6343 (2006).

[18] R. F. V. de Souza, E. M. Sussuchi, W. F. De Giovani, Synth. React. Inorg. Met.-Org. Chem. 33, 1125 (2003).

[19] J. Zhou, L. F. Wang, J. Y. Wang, N. Tang, J. Inorg. Biochem. 83, 41 (2001).

[20] J. P. Cornard, L. Dangleterre, C. Lapouge, J. Phys. Chem. A 109, 10044 (2005).

[21] T. J. Mabry, K. R. Markham, M. B. Thomas, *The systematic identification of flavonoids*, Springer-Verlag, New York, (1970).

[22] F. Galvano, L. La Fauci, G. Lazzarino, V. Fogliano, A. Ritieni, S. Ciappellano, N. C. Battistini, B. Tavazzi, G. Galvano, J. Nutritional Biochem. 15, 2 (2004).

[23] A. Calzolari, D. Varsano, A. Ruini, A. Catellani, R. Tel-Vered, H. B. Yildiz, O. Ovits, and I. Willner, J. Phys. Chem. A 113, 8801 (2009).

[24] S. Lamy, M. Blanchette, J. M. Levesque, R. Lafleur, Y. Durocher, A. Moghrabi, S. Barrette, D. Gingras, R. Béliveau, Carcinogenesis 27, 989 (2006).

[25] T. Miyazawa, K. Nakagawa, M. Kudo, K. Muraishi, K. Someya, J. Agric. Food Chem. 47, 1083 (1999).

[26] C. A. Rice-Evans, N. J. Miller, P. G. Bolwell, P. M. Bramley, J. B. Pridham, Free Radical Res. 22, 375 (1995).

[27] W. Zheng, S. Y. Wang, J. Agric. Food Chem. 51, 502 (2003).

[28] M. Grätzel, J. Photochem. Photobiol. C 4, 145 (2003).

[29] M. Grätzel, Chem. Lett. 34, 8 (2005).

[30] M. Law, L. E. Greene, J. C. Johnson, R. Saykally, P. Yang, Nat. Mater. 4, 455 (2005).

[31] B. Tan, Y. Y. Wu, J. Phys. Chem. B 110, 15932 (2006).

[32] G. K. Mor, K. Shankar, M. Paulose, O. K. Varghese, C. A. Grimes, Nano Lett. 6, 215 (2006).

[33] K. Zhu, N. R. Neale, A. Miedaner, A. Frank, J. Nano Lett. 7, 69 (2007).

[34] F. De Angelis, S. Fantacci, A. Selloni, M. Grätzel, M. K. Nazeeruddin, Nano Lett. 7, 3189 (2007).

[35] N. J. Cherepy, G. P. Smestad, M. Grätzel, J. Z. Zhang, J. Phys. Chem. B 101, 9342 (1997).

[36] S. Hao, J. H. Wu, Y. F. Huang, J. M. Lin, Sol. Energy 80, 209 (2006).

[37] K. Wongcharee, V. Meeyoo, S. Chavadej, Sol. Energy Mater. Sol. Cells 91, 566 (2007).

[38] W. M. Campbell, K. W. Jolley, P. Wagner, K. Wagner, P. J. Walsh, K. C. Gordon, L. Schmidt-Mende, M. K. Nazeeruddin, Q. Wang, M. Grätzel, D. L. Officer, J. Phys. Chem. C 111, 11760 (2007).

[39] R. O′Regan and M. Grätzel, Nature 353, 737 (1991).

[40] W. D. Zeng, Y. M. Cao, Y. Bai, Y. H. Wang, Y. S. Shi, M. Zhang, F. F. Wang, C. Y. Pan, P. Wang, Chem. Mater. 22, 1915 (2010).

[41] N. S. Lewis, Science 315, 798 (2007).

[42] K. Y. J. Chen, Nanoscale Res Lett 4, 1 (2009).

[43] B. Tian, X. L. Zheng, T. J. Kempa, Y. Fang, N. F. Yu, G. H. Yu, J. L. Huang, C. M. Lieber, Nature 449, 885 (2007).

[44] A. Braun, J. Tcherniac, Berichte der Deutschen Chemischen Gesellschaft 40, 2709 (1907).

[45] H. de Diesbach, E. von der Weid, Helevtica Chimica Acta 10, 886 (1927).

[46] J. M. Robertson, J. Chem. Soc. 615, (1935).

[47] C. E. Dent and R. P. Linstead, J. Chem. Soc. 1027, (1934).

[48] R. P. Linstead, J. Chem. Soc. 1016, (1934).

[49] K. S. Lokesh, N. Uma, B. N. Achar, J. Non-Cryst. Solids 353, 384 (2007).

[50] S. Singh, S. K. Tripathi, G. S. S. Saini, Mater. Chem. & Phys. 112, 793 (2008).

[51] S. Senthilarasu, S. Velumani, R. Sathyamoorthy, A. Subbarayan, et al. Appl. Phys. A 77, 383 (2003).

[52] T. Enokida, R. hirohashi, N. Morohashi, Bull. Chem. Soc. Jpn. 64, 279 (1991).

[53] S. Kera, H. Yamane, N. Ueno, Progress in Surface Science 84, 135 (2009).

[54] K.-Y. Lee, Chem. Rev. 93, 449 (1993).

[55] N. B. McKeown, *Phthalocyanine materials: synthesis, structure and function,* Cambridge University Press, (1998).

[56] F. Iwatsu, J. Phys. Chem. 92, 1678 (1988).

[57] A. T. Davidson, J. Chem. Phys. 77, 168 (1982).

[58] L. Edwards, M. Gouterman, J. Mol. Spec. 33, 292 (1970).

[59] D. Pop, B. Winter, W. Freyer, I. V. Hertel, W. Widdra, J. Phys. Chem. B 107, 11643 (2003).

[60] J. S. Shirk, R. G. S. Pong, S. R. Flom, H. Heckmann, M. Hanack, J. Phys. Chem. A 104, 1438 (2000).

[61] P. Y. Reddy, L. Giribabu, C. Lyness, H. J. Snaith, Angew. Chem. Int. Ed. 46, 373 (2007).

[62] M. Grätzel, Nature 414, 338 (2001).

[63] N. R. Armstrong, W. Wang, D. M. Alloway, D. Placencia, E. Ratcliff, M. Brumbach, Macromol. Rapid. Commun. 30, 717 (2009).

[64] T. Strenalyuk, S. Samdal, H. V. Volden, J. Phys. A 112, 4853 (2008).

[65] A. A. M. Farag, Opt. & Laser Tech. 39, 728 (2006).

[66] J. Xue, S. Uchida, B. P. Rand, S. R. Forrest, Appl. Phys. Lett. 84, 3013 (2004).

[67] M. Brumbach, D. Placencia, N. R. Armstrong, J. Phys. Chem. C 112, 3142 (2008).

[68] S. Pfuetzner, J. Meiss, A. Petrich, M. Riede, K. Leo, Appl. Phys. Lett. 94, 253303 (2009).

[69] Y. S. Hsiao, W. T. Whang, S. C. Suen, J. Y. Shiu, C. P. Chen, Nanotechnology 19, 415603(2008).

[70] D. Gebeyehu, B. Maenning, J. Drechsel, K. Leo, M. Pfeiffer, Solar Energy Mater. & Solar cells 79, 81 (2003).

[71] P. Peumans, S. Uchida, S. R. Forrest, Nature 425, 158 (2003).

[72] S. Günes, H. Neugebauer, N. S. Sariciftci, Chem. Rev. 107, 1324 (2007).

[73] S.-H. Lee, D.-H. Kim, J.-H. Kim, T.-H. Shim, J.-G. Park, Synthetic Metals 159, 1705 (2009).

[74] K. M. Lau, J. X. Tang, H. Y. Sun, C. S. Lee, S. T. Lee, D. H. Yan, Appl. Phys. Lett. 88, 173513 (2006).

[75] H. Hoppe and N. S. Sariciftci, J. Mater. Res. 19, 1924 (2004).

[76] H. Spanggaard, F. C. Krebs, Solar Energy Materals & Solar Cells 83, 125 (2004).

[77] W. B. Chen, H. F. Xiang, Z. X. Xu, B. P. Yan, V. A. L. Roy, C. M. Che, Appl. Phys. Lett. 91, 191109 (2007).

[78] M. Y. Chan, S. L. Lai, M. K. Fung, C. S. Lee, and S. T. Lee, Appl. Phys. Lett. 90, 023504 (2007).

[79] M. Vogel, J. Strotmann, B. Johnev, M. Ch. Lux-Steiner, K. Fostiropoulos, Thin Solid Films 511, 367 (2006).

[80] K. C. Chiu, L. T. Juey, C. F. Su, S. J. Tang, M. N. Jong, S. S. Wang, J. S. Wang, C. S. Yang, W. C. Chou, J. of Crystal Growth 310, 1734 (2008).

[81] K. Fostiropoulos and W. Schindler, Phys. Status Solidi B 246, 2840 (2009).

[82] I. Kim, H. M. Haverinen, J. Li, G. E. Jabbour, Appl. Mater. & Inter. 2, 1390 (2010).

[83] T. Taima, J. Sakai, T. Yamanari, K. Saito, Solar Energy Materials & Solar cellls 93, 742 (2009).

[84] Z. R. Hong, B. Maennig, R. Lessmann, M. Pfeiffer, K. Leo, P. Simon, Appl. Phys. Lett. 90, 203505 (2007).

[85] S. H. Park, A. Roy, S. Beaupre, S. Cho, N. Coates, J. S. Moon, D. Moses, M. Leclerc, K. Lee, A. J. Heeger, Nature Photonics 3, 297 (2009).

[86] J. C. Bernède, Y. Berredjem, L. Cattin, and M. Morsli, Appl. Phys. Lett. 92, 083304 (2008).

[87] J. Y. Lee, S. T. Connor, Y. Cui, P. Peumans, Nano Lett. 10, 1276 (2010).

[88] L. G. De Arco, Y. Zhang, C. W. Schlenker, K. Ryu, M. E. Thompson, and C. W. Zhou, ACSNano 4, 2865 (2010).

[89] M. Hiramoto, K. Sakai, Proc. of SPIE 7052, 70520H (2008).

[90] J. Y. Kim, K. Lee, N. E. Coates, D. Moses, T. Q. Nguyen, M. Dante, A. J. Heeger, Science 317, 222 (2007).

[91] J. G. Xue, S. Uchida, B. P. Rand, S. R. Forrest, Appl. Phys. Lett. 85, 5757 (2004).

[92] M. Born and K. Huang. *Dynamical theory of crystal lattices*. Oxford University Press, Oxford, (1954).

[93] W. M. C. Foulkes, L. Mitas, R. J. Needs, and G. Rajagopal, Rev. Mod. Phys. 73, 33 (2001).

[94] D. R. Hartree, Proc. Camb. Phil. Soc. 24, 89 (1928).

[95] J. C. Slater, Phys. Rev. 34, 1293 (1929).

[96] V. Fock, Z. Phys. 61, 209 (1930).

[97] H. Thomas, Proc. Camb. Phil. Soc. 23, 542 (1927).

[98] E. Fermi, Accad. Naz. Lincei 6, 602 (1927).

[99] P. Hohenberg and W. Kohn, Phys. Rev. 136, B864 (1964).

[100] W. Kohn and L. J. Sham, Phys. Rev. 140, A1133 (1965).

[101] D. M. Ceperley and B. L. Alder, Phys. Rev. Lett. 45, 566 (1980).

[102] A. D. Becke, Phys. Rev. A 38, 3098 (1988).

[103] D. C. Langreth and M. J. Mehl, Phys. Rev. Lett. 47, 446 (1981).

[104] C. Lee, W. Yang, and R. C. Parr, Phys. Rev. B 37, 785 (1988).

[105] J. P. Perdew, J. A. Chevary, S. H. Vosko, K. A. Jackson, M. R. Pederson, D. J. Singh and C. Fiolhais, Phys. Rev. B 46, 6671 (1992).

[106] J. P. Perdew, K. Burke, M. Ernzerhof, Phys. Rev. Lett. 77, 3865 (1996).

[107] B. Hammer, L. B. Hansen, J. K. Norskov, Phys. Rev. B 59, 7413 (1999).

[108] S. Kurth, J. P. Perdew, and P. Blaha, Int. J. Quant. Chem. 75, 889 (1999).

[109] A. D. Becke, J. Chem. Phys. 98, 1372 (1993).

[110] A. D. Becke, J. Chem. Phys. 98, 5648 (1993).

[111] J. P. Perdew, M. Ernzerhof, K. Burke, J. Chem. Phys. 105, 9982 (1996).

[112] J. Heyd, G. E. Scuseria, M. Ernzerhof, J. Chem. Phys.118, 8207 (2003).

[113] M. Dion, H. Rydberg, E. Schröder, D. C. Langreth, and B. I. Lundqvist, Phys. Rev. Lett. 92, 246401 (2004).

[114] Y. Andersson, D. C. Langreth, and B. I. Lundqvist, Phys. Rev. Lett. 76, 102 (1996).

[115] O. F. Sankey and D. J. Niklewski, Phys. Rev. B 40, 3979 (1989).

[116] D. Sanchez-Portal, E. Artacho, J. M. Soler, J. Phys.: Condens. Matter 8, 3859 (1996).

[117] A. Tsolakidis, D. Sánchez-Portal and R.M. Martin, Phys. Rev. B 66, 235416 (2002).

[118] S. Meng and E. Kaxiras, J. Chem. Phys. 129, 054110 (2008).

[119] D. J. Singh. Planewaves, *pseudopotentials and the LAPW method*. Kluwer Academic Publishers, Boston, (1993).

[120] O. K. Andersen, Phys. Rev. B 12, 3060 (1975).

[121] W. E. Pickett. *Pseudopotential methods in condensed matter applications*. North-Holland, Amsterdam, (1989).

[122] J. A. Appelbaum and D. R. Hamann, Phys. Rev. B 8, 1777 (1973).

[123] N. Troullier, and J. L. Martins, Phys. Rev. B 43, 1993 (1991).

[124] T. Kreibich and E. K. U. Gross, Phys. Rev. Lett. 86, 2984 (2001).

[125] E. Runge and E. K. U. Gross, Phys. Rev. Lett. 52, 997 (1984).

[126] C. Swalina, M. V. Pak, A. Chakraborty, S. Hammes-Schiffer, J. Phys. Chem. A 110, 9983 (2006).

[127] N. J. Mason, J. M. Gingell, J. A. Davies, H. Zhao, I. C. Walker, and M. R. F. Siggel, J. Phys. B: Atom. Mol. Opt. Phys. 29, 3075 (1996).

[128] R. Mota, R. Parafita, A. Giuliani, M.-J. Hubin-Franskin, J. M. C. Lourenco, G. Garcia, S.V. Hoffmann, N. J. Mason, P. A. Ribeiro, M. Raposo, and P. Limao-Vieira, Chem. Phys. Lett. 416, 152 (2005).

[129] W. F. Chan, G. Cooper, and C. E. Brion, Chem. Phys. 180, 77 (1994).

[130] W. F. Chan, G. Cooper, and C. E. Brion, Chem. Phys. 178, 401 (1993).

[131] G. Cooper, J. E. Anderson, and C. E. Brion, Chem. Phys. 209, 61 (1996).

[132] F. W. Taylor, Rep. Prog. Phys. 65, 1 (2002).

[133] M. Suto and L.C. Lee, J. Chem. Phys. 78, 4515 (1983).

[134] E. E. Koch and A. Otto, Chem. Phys. Lett. 12, 476 (1972).

[135] J. A. Pople, R. Seeger, and R. Krishnan, Int. J. Quantum Chem. 149 (Suppl. Y-11), (1977).

[136] H. G. Kummel, *A biography of the coupled cluster method*, in *Proceedings of the 11th international conference: Recent progress in many-body theories*, edited by R. F. Bishop, T. Brandes, K. A. Gernoth, N. R. Walet, and Y. Xian (World Scientific Publishing, Singapore, 2002, pp. 334-348).

[137] K. Andersson, P. A. Malmqvist, and B. O. Roos, J. Chem. Phys. 96, 1218 (1992).

[138] N. N. Matsuzawa, A. Ishitani, D. A. Dixon, and T. Uda, J. Phys. Chem. 105, 4953 (2001).

[139] M. E. Casida, C. Jamorski, K.C. Casida, and D.R. Salahub, J. Chem. Phys. 108, 4439 (1998).

[140] C. Adamo, G. E. Scuseria, and V. Barone, J. Chem. Phys. 111, 2889 (1999).

[141] R. J. Cave, K. Burke, and E.W. Castner, Jr., J. Phys. Chem. A 106, 9294 (2002).

[142] K. Burke, J. Werschnik, and E.K.U. Gross, J. Chem. Phys. 123, 062206 (2005).

[143] B. G. Levine, C. Ko, J. Quenneville and T.J. Martinez, Mol. Phys. 104, 1039 (2006).

[144] M. E. Casida, in *Recent Developments and Applications in Density Functional Theory*, edited by J.M. Seminario (Elsevier, Amsterdam, 1996).

[145] N. Santhanamoorthi, K. Senthilkumar and P. Kolandaivel, Mol. Phys. 107, 1629 (2009).

[146] E. Tapavicza, I. Tavernelli and U. Rothlisberger, Phys. Rev. Lett. 98, 023001 (2007).

[147] R. Bauernschmitt and R. Ahlrichs, Chem. Phys. Lett. 256, 454 (1996).

[148] R. E. Stratmann, G. E. Scuseria and M. J. Frisch, J. Chem. Phys. 109, 8218 (1998).

[149] F. Furche and R. Ahlrichs, J. Chem. Phys. 117, 7433 (2002).

[150] M. Parac and S. Grimme, Chem. Phys. 292, 11 (2003).

[151] R. Bauernschmitt, M. Haser, O. Treutler and Ahlrichs, Chem. Phys. Lett. 264, 573 (1996).

[152] S. J. A. van Gisbergen, A. Rosa, G. Ricciardi and E. J. Baerends, J. Chem. Phys. 111, 2499 (1999).

[153] M. Miura, Y. Aoki and B. Champagne, J. Chem. Phys. 127, 084103 (2007).

[154] K. Yabana and G.F. Bertsch, Phys. Rev. B 54, 4484 (1996).

[155] O. Sugino and Y. Miyamoto, Phys. Rev. B 59, 2579 (1999).

[156] A. Castro, M.A.L. Marques and A. Rubio, J. Chem. Phys. 121, 3425 (2004).

[157] I. Tavernelli, U.F. Rohrig and U. Rothlisberger, Mol. Phys. 103, 963 (2005).

[158] J. Ren, E. Kaxiras, and S. Meng, Molecular Physics 108, 1829 (2010).

[159] M.A.L. Marques, A. Castro, and A. Rubio, The octopus manual. http://www.tddft.org/programs/octopus/, cited on April 2011.

[160] J. M. Soler, E. Artacho, J. D. Gale, A. García, J. Junquera, P. Ordejón, and D. Sánchez-Portal, J. Phys.: Condens. Matter 14, 2745 (2002).

[161] J. P. Perdew and A. Zunger, Phys. Rev. B 23, 5048 (1981).

[162] E. Artacho, D. Sánchez-Portal, P. Ordejón, A. García, and J.M. Soler, Phys. Stat. Sol. B 215, 809 (1999).

A. Tsolakidis, D. Sánchez-Portal, and R.M. Martin, Phys. Rev. B **66**, 235416 (2002).

[163] A. Tsolakidis and E. Kaxiras, J. Phys. Chem. A 109, 2373 (2005).

[164] A.T. Al-Kazwini, P. O'Neill, R. B. Cundall, G. E. Adams, A. Junino, and J. Maignan. Tetrahedron Lett. 33, 3045 (1992).

[165] V.P. Grishchuk, S.A. Davidenko, I.D. Zholner, A.B. Verbitskii, M.V. Kurik, and Y.P. Piryatinskii, Tech. Phys. Lett. 28, 36 (2002).

[166] T.L. Chan, M.L. Tiago, E. Kaxiras, and J.R. Chelikowsky, Nano Lett. 8, 596 (2008).

[167] A. Tsolakidis and R. M. Martin, Phys. Rev. B 71, 125319 (2005).

[168] I. Vasiliev, S. Ogut, and J. R. Chelikowsky, Phys. Rev. Lett. 86, 1813 (2001).

[169] E.E. Koch and M. Skibowski, Chem. Phys. Lett. 9, 429 (1971).

[170] P.G. Wilkison and H.L. Johnston, J. Chem. Phys. 18, 190 (1050).

[171] R. van Harrevelt, J. Chem. Phys. 126, 204313 (2007).

[172] J. S. Wright, E. R. Johnson, G. A. DiLabio, J. Am. Chem. Soc. 123, 1173 (2001).

[173] M. Leopoldini, T. Marino, N. Russo, M. Toscano, J. Phys. Chem. A 108, 4916 (2004).

[174] W. Bors, W. Heller, C. Michel, M. Saran, Methods Enzymol. 186, 343 (1990).

[175] J. Zhou, L. F. Wang, J. Y. Wang, N. Tang, Transition Metal Chem. 26, 57 (2001).

[176] J. E. Brown, H. Khodr, R. C. hider, C. A. Rice-Evans, Biochem. J. 330, 1173 (1998).

[177] M. D. Engelmann,R. Hutcheson, I. F. Cheng, J. Agri. Food Chem. 53, 2953 (2005).

[178] M. Rossi, L. F. Rickles, W. A. Halpin, Bioorg. Chem. 14, 55 (1986).

[179] Ch. E. Lekka, J. Ren, S. Meng, E. Kaxiras, J. Phys. Chem. B 113, 6478 (2009).

[180] S. V. Jovanovic, S. Steenken, M. Tosic, B. Marjanovic, M. G. Simic, J. Am. Chem. Soc. 116, 4846 (1994).

[181] N. Sugihara, T. Arakawa, M. Ohnishi, K. Furuno, Free Radic. Biol. Med. 27, 1313 (1999).

[182] M. T. Fernandez, L. Mira, M. H. Florencio, K. R. Jennings, J. Inorg. Biochem. 92, 105 (2002).

[183] L. Mira, M. T. Fernandez, M. Santos, R. Rocha, M. H. Florenchio, K. R. Jennings, Free Radical Res. 36, 1199 (2002).

[184] B. Tan, Y. Y. Wu, J. Phys. Chem. B 110, 15932 (2006).

[185] K. Zhu, N. R. Neale, A. Miedaner, A. J. Frank, Nano Lett. 7, 69 (2007).

[186] B. Liu, E. S. Aydil, J. Am. Chem. Soc. 131, 3985 (2009).

[187] X. J. Feng, K. Shankar, O. K. Varghese, M. Paulose, T. J. Latempa, C. A. Grimes, Nano Lett. 8, 3781 (2008).

[188] T. Kawahara, Y. Konishi, H. Tada, N. Tohge, J. Nishii, S. Ito, Angew. Chem. 114, 2935 (2002).

[189] A. L. Linsebigler, G. Lu, J. T. Yates, Jr. Chem. Phys. 95, 735 (1995).

[190] Z. Ding, G. Q. Lu, P. F. Greenfield, J. Phys. Chem. B 104, 4815 (2000).

[191] A. Selloni, Nature Materials 7, 613 (2008).

[192] G. K. Mor, O. K. Varghese, M. Paulose, K. Shankar, C. A. Grimes, Sol. Energy Mater. Sol. Cells 90, 2011 (2006).

[193] X. F. Duan, Y. Huang, Y. Cui, J. F. Wang, C. M. Lieber, Nature 409, 66 (2001).

[194] L. J. Lauhon, M. S. Gudiksen, D. Wang, C. M. Lieber, Nature 420, 57 (2002).

[195] M. S. Gudiksen, L. J. Lauhon, J. F. Wang, D. C. Smith, C. M. Lieber, Nature 415, 617 (2002).

[196] P. Caroff, K. A. Dick, J. Johansson, M. E. Messing, K. Deppert, L. Samuelson, Nat. Nano. 4, 50 (2009).

[197] F. M. Ross, Nat. Nano. 4, 17 (2009).

[198] M. Heiβ, S. Conesa-Boj, Jun Ren, H.-H. Tseng, A. Gali, A. Rudolph, Em Uccelli, F. Peiro, J. R. Morante, D. Schuh, E. Reiger, E. Kaxiras, J. Arbiol, A. F. i Morral, Phys. Rev. B (2010).

[199] F. De Angelis, S. Fantacci, A. Selloni, M. K. Nazeeruddin, M. Grätzel, J. Am. Chem. Soc. 129, 14156 (2007).

[200] K. Wongcharee, V. Meeyoo, S. Chavadej, Sol. Energy Mater. Sol. Cells 91, 566 (2007).

[201] F. De Angelis, S. Fantacci, A. Selloni, M. Grätzel, M. K. Nazeeruddin, Nano Lett. 7, 3189 (2007).

[202] L. G. C. Rego, V. S. Batista, J. Am. Chem. Soc. 125, 7989 (2003).

[203] P. Persson, M. J. Lundqvist, J. Phys. Chem. B 109, 11918 (2005).

[204] W. R. Duncan, O. V. Prezhdo, Annu. Rev. Phys. Chem. 58, 143 (2007).

[205] S. Meng, J. Ren, E. Kaxiras, Nano Lett. 8, 3266 (2008).

[206] R. Huber, J. E. Moser, M. Grätzel, J. Wachtveitl, J. Phys. Chem. B 106, 6994 (2002).

[207] J. Schnadt, B. A. Bruhwiler, L. Patthey, J. N. O'Shea, S. Sodergren, M. Odelius, A. Ahuja, O. Karis, M. Bassler, P. Persson, H. Siegbahn, S. Lunell, N. Martensson, Nature 418, 620 (2002).

[208] W. Stier, W. R. Duncan, O. V. Prezhdo, Adv. Materials 16, 240 (2004).

[209] Y. Wakayama, J. Phys. Chem. C 111, 2675 (2007).

[210] H. Huang, W. Chen, A. T. S. Wee, J. Phys. Chem. C 112, 14913 (2008).

[211] E. Barrena, D. G. de Oteyza, H. Dosch, Y. Wakayama, ChemPhysChem 8, 1915 (2007).

[212] Y. L. Huang, W. Chen, S. Chen, A. T. S. Wee, Appl. Phys. A 95, 107 (2009).

[213] W. Chen, H. Huang, S. Chen, Y. L. Huang, X. Y. Gao, A. T. S. Wee, Chem. Mater. 20, 7017 (2008).

[214] S. D. Wang, X. Dong, C. S. Lee, S. T. Lee, J. Phys. Chem. B 108, 1529 (2004).

[215] D. G. de Oteyza, E. Barrena, J. O. Osso, H. Dosch, S. Meyer, J. Pflaum, Appl. Phys. Lett. 87, 183504 (2005).

[216] G. Kresse and J. Furthmuller, Phys. Rev. B 54, 11169 (1996).

[217] J. Heyd, G. E Scuseria, M. Ernzerhof, J. Chem. Phys. 124, 219906 (2006).

[218] C. J. Brown, J. Chem. Soc. A 2488 (1968).

[219] E. Kol'tsov, T. Basova, P. Semyannikov, I. Igumenov, Materials Chem. and Phys. 86, 222 (2004).

[220] N. Marom, O. Hod, G. E. Scuseria, L. Kronik, J. Chem. Phys. 128, 164107 (2008).

[221] Y. L. Wang, J. Ren, C. L. Song, Y. P. Jiang, L. L. Wang, K. He, X. Chen, J. F. Jia, S. Meng, E. Kaxiras, Q. K. Xue, X. C. Ma, Phys. Rev. B 82, 245420 (2010).

[222] J. Ren, S. Meng, Y. L. Wang, X. C. Ma, Q. K. Xue, E. Kaxiras, submitted to J. Chem. Phys. (2011).

[223] Y. L. Huang, H. Li, J. Ma, H. Huang, W. Chen, S. Chen, A. T. S. Wee, Langmuir 26, 3329 (2010).

[224] Z. R. Hong, B. Maennig, R. Lessmann, M. Pfeiffer, K. Leo. P. Simon, App. Phys. Lett. 90, 203505 (2007).

[225] K. Akaike, K. Kanai, Y. Ouchi, K. Seki, Adv. Funct. Mater. 20, 715 (2010).

[226] M. Ichikawa, E. Suto, H.-G. Jeon, Y. Taniquchi, Organic Electronics 11, 700 (2010).

[227] H. Huang, W. Chen, S. Chen, D. C. Qi, X. Y. Gao, A. T. S. Wee, App. Phys. Lett. 94, 163304 (2009).

[228] M. Fendrich, Th. Wagner, M. Stöhr, R. Möller, Phys. Rev. B 73, 115433 (2006).

[229] Y. C. Zhou, Z. T. Liu, J. X. Tang, C. S. Lee, S. T. Lee, J. of Elect. Spect. and Related Phen. 174, 35 (2009).

[230] J. C. Bernéde, Y. Berredjem, L. Cattin, M. Morsli, App. Phys. Lett. 92, 083304 (2008).

[231] G. J. Dutton, W. Jin, J. E. Reutt-Robey, S. W. Robey, Phys. Rev. B 82, 073407 (2010).

[232] K. Manandhar, T. Ellis, K.T. Park, T. Cai, Z. Song, J. Hrbek, Surf. Sci. 601, 3623 (2007).

[233] H. Karacuban, M. Lange, J. Schaffert, O. Weingart, Th. Wagner, R. Möller, Surf. Sci. 603, L39 (2009).

[234] S. Godlewski, A. Tekiel, J. S. Prauzner-Bechcicki, J. Budzioch, M. Szymonski, ChemPhysChem 11, 1863 (2010).

[235] G. E. Collins, V. S. Williams, L.-K. Chau, K. W. Nebesny, C. England, P. A. Lee, T. Lowe, Q. Fernando and N. R. Armstrong, Synthetic Metals 54, 351 (1993).

[236] D. Chen, D. Sarid, Surf. Sci. 318, 74 (1994).

[237] M. S. Dresselhaus, G. Dresselhaus, P. C. Eklund, *Science of fullerenes and carbon nanotubes*. Academic press, San Diego, 1996.

[238] S. S. Wong, W. W. Pai, C. H. Chen, M. T. Lin, Phys. Rev. B 82, 125442 (2010).

[239] L. L. Wang, H. P. Cheng, Phys. Rev. B 69, 165417 (2004).

[240] Y. Kodama, K. Ohno, App. Phys. Lett. 96, 034101 (2010).

Curriculum Vitae: Jun Ren
Doctoral Candidate

Department of Materials Science and Engineering, Swiss Federal Institute of Technology (EPFL), Lausanne CH-1015

Email: jun.ren@epfl.ch ; Tel: +41 21 693 1157; Fax: +41 21 693 1125

Experience

Doctoral Student　　　　　　　　　　*Oct. 2009 – present*
Materials Science Program, Swiss Federal Institute of Technology (EPFL)
Working with Prof. Efthimios Kaxiras:
- Electronic interaction between phthalocyanine and fullerene
- Properties of $F_{16}CuPc$ (CuPc) layers deposited on graphene

Ph.D. Student　　　　　　　　　　*Aug. 2008 – Sep. 2009*
Mechanic Engineering and Materials Science, Pittsburgh University
- Initial stage of Cu(001) surface oxidation

Research Assistant　　　　　　　　　*Sep. 2006 – Jul. 2008*
Physics Department, Harvard University
Working with Prof. Efthimios Kaxiras:
- TiO_2 nanowire sensitized by natural dyes for solar cell applications
- Optical absorption spectra for typical small molecules
- Effective hamiltonian for FeAs based superconductors
- Assembly and interaction of flavonoids with metal cations

Graduate Research Assistant　　　　　*Sep. 2002 – Jul. 2005*
Sichuan Normal University, Chengdu, P. R. China
Visiting student　　　　　　　　　　*Sep. 2003 – Jul. 2005*
Institute of Physics, Chinese Academy of Sciences
Working with Profs. Ling Li, Ke Xia, and Gerrit E. W. Bauer:
- Water-surface structure and interaction
- Spin dependent magnetoresistance of Fe(Co,Ni)|GaAs|Fe(Co,Ni)<001> tunnelling junctions

Undergraduate study　　　　　　　　*Sep. 1997 – Jul. 2001*
Sichuan Normal University

Education　　**M. Sc., Condensed Matter Physics, Sichuan Normal University, 2005**
　　　　　　　in coalition with Institute of Physics, Chinese Academy of Sciences
　　　　　　B. Sc., Physics, Sichuan Normal University, 2001

Awards
- Academic Scholarship, Inst. Phys., Chinese Academy of Sciences, 2003-2005
- Excellence in Student Leadership, Sichuan Normal University, 1999
- Excellent Youth Award, Sichuan Normal University, 1998
- Academic Excellence, Sichuan Normal University, 01/1998
- Academic Excellence, Sichuan Normal University, 09/1998

Language　Chinese (Native)
　　　　　　English (fluent)
　　　　　　French (A1)

Computer	▪ First-principles simulation packages: LMTO, WIEN2k, Stuttgart, VASP, Siesta ▪ Programming skills: proficient in C, Pascal, Fortran, Mathematica, Matlab
Presentations	▪ *Electronic interaction between copper(fluoro-)phthalocyanine and epitaxial graphene*, TokyoTech-EPFL workshop, Chateau d'Oex, Mar. 2011.

▪ *Selective adsorption and electronic interactions of $F_{16}CuPc$ on epitaxial graphene* (poster), Annual meeting of the Swiss physical society, Basel, Jun. 2010.

▪ *Cu surface oxidation by water and oxygen,* American Physical Society, March Meeting, Pittsburgh, Mar. 2009.

▪ *Complexation mechanism of flavonoids with iron: structural and optical signatures,* American Physical Society, March Meeting, New Orleans, Mar. 2008.

▪ *Atomic structure and interaction of water with copper surfaces: the borderline for water dissociation* (poster)*,* Material Research Society, Fall meeting, Boston, Nov. 2006.

▪ *A study of magnetoresistance of Fe|GaAs|Fe tunneling junction,* Fourth National Conference on Nano-magnets and Magnetic Films, Tianjing, May 2004.

▪ *Magnetoresistance of Fe|GaAs|Fe <001> tunneling junctions,* Annual Autumn Meeting of Chinese Physics Society, Shanxi, Sep. 2004.

Activities	▪ Organizer of EDMX "happy-hour" social activity, EPFL, 2010-2011

▪ Volunteer at Cambridge Hospital, MA, 2007-2008

▪ Volunteer at the 55th anniversary festivities of Sichuan Normal University, involving reception, accounting, and organizing meetings, 2005

▪ Tutoring college and high school students in physics and electronics, 1999-2005

▪ Fourth prize in table-tennis, Autumn Sports Game, Institute of Physics, 2004

▪ Hobbies including swimming, table-tennis, music